
MASTER THESIS
GEOGRAPHY BASED BI-FACIAL CELL DESIGN FOR LOW LCOE
SANTHOSH RAMESH
Technische Universiteit Delft
TUDelft

Geography based bi-facial cell design for low LCoE

by

Santhosh Ramesh

to obtain the degree of Master of Science
at the Delft University of Technology,
to be defended publicly on Tuesday August 20, 2019 at 3:00 PM.

Student number:	4742664	
Project duration:	September 1, 2018 – May 30, 2019	
Thesis committee:	Prof. Dr. Arthur Weeber,	TU Delft, Supervisor
	Prof. Dr. Arno Smets,	TU Delft
	Dr. Mohamad Ghaffarian Niasar,	TU Delft
	Dr. Gaby Janssen,	ECN.TNO, Daily Supervisor
	Dr. Rudi Santbergen,	TU Delft, Advisor

This thesis is confidential and cannot be made public until December 31, 2019.

Acknowledgements

First of all, I would like to thank Prof. Dr. Arthur Weeber for helping me find the master thesis opportunity at ECN part of TNO and accepting to supervise it. I would also like to thank Prof. Dr. Arno Smets for accepting the thesis proposal.

I would like to thank Dr. Gaby Janssen, ECN part of TNO for accepting me for this thesis work and guiding me throughout the project. I would also like to thank Dr. Bas Van Aken, ECN part of TNO for helping me with his scientific knowledge to complete the tasks in a better way. I would like to extend my sincere thanks to other members of Department of Solar energy, ECN part of TNO for giving valuable feedback on my work and help me improve it.

Last but not least, I would like to extend my gratitude to my parents for supporting me mentally and financially, helping me complete my masters degree successfully.

Santhosh Ramesh
4742664
Delft, August 2019

Abstract

The Levelized Cost of Electricity (LCoE) produced by PV systems is determined by yield (kWh) and cost of the system. Reducing the LCoE of the solar power can be achieved either by increasing the yield or by reducing the cost. The yield of bi-facial PV systems is promoted by high efficiency and a high bi-faciality factor.

Yield due to the front efficiency depends on the parameters (V_{oc} ,I_{sc} and FF) that contribute to that efficiency. It was found that the different parameter helped maximize the yield in each climatic condition. For low irradiation and low operating temperature zones, yield improved when the product $I_{sc} \times V_{oc}$ was increased at the cost of the FF. While at equatorial tropical climates with fairly high temperatures, yiele improved when V_{oc} was increased at cost of I_{sc} and FF. For high irradiance and high temperature desert climates, yield improved when the product $V_{oc} \times FF$ increased at the cost of I_{sc}. Designing cells to suit the operating conditions of the region improved yield per W_p thereby reducing the LCoE.

A large part of the cell processing cost is in the metal (silver) used on the cell. The amount of silver is usually optimized for the cell efficiency (i.e. power in W) delivered under standard test conditions, i.e. a solar irradiance of 1000 W/m2. When the metal patterns were optimized for the yield at a climatic zone, results showed that up to 50% of silver per cell could be saved (From a reference cell considered). Up to 5% LCoE improvement was theorized.

The irradiance on the bi-facial modules varies with different system orientations (Equator facing, East west tilted, East West Vertical). The metal patterns were also optimized for the different system orientation at a climatic condition. The results showed metal patterns can be made more thin when designed for vertical systems.

Advanced c-Si cell concepts try to reach the theoretical efficiency by employing different passivation technologies, grid patterns, etc. Each cell technology will have advantage over the other. This makes it interesting to study if we can attribute a cell concept to a climatic condition where it will outperform other cell concepts.

Contents

Acknowledgements ii

Abstract iii

List of Figures ix

List of Tables xiii

1 Introduction 1

2 Literature Study 3
- 2.1 Bi-facial PV . . . 3
  - 2.1.1 Factors affecting bi-facial gain . . . 4
- 2.2 Bi-facial energy yield . . . 5
  - 2.2.1 Irradiance model . . . 5
  - 2.2.2 Thermal model . . . 7
  - 2.2.3 Yield determination . . . 7
- 2.3 Climatic zones . . . 8
  - 2.3.1 Köppen-Geiger climate classification . . . 8
  - 2.3.2 Climate zones considered for analysis . . . 10
- 2.4 Simulators . . . 10
  - 2.4.1 Quokka cell simulator . . . 10
  - 2.4.2 BIGEYE - Bi-facial yield simulator . . . 11

3 Yield maximizing parameter 13
- 3.1 Introduction . . . 13
- 3.2 Test setup . . . 14
- 3.3 Results and Discussion . . . 17
  - 3.3.1 Oceanic Climate - London . . . 17
  - 3.3.2 Tropical climate - Singapore . . . 20
  - 3.3.3 Hot desert climate - Doha . . . 22
- 3.4 Conclusion . . . 25

4 Optimizing the metal pattern for different geographic location 27
- 4.1 Introduction . . . 27
- 4.2 Test setup . . . 28
  - 4.2.1 Reference cell and module . . . 28
  - 4.2.2 Metal pattern variable matrix . . . 28
  - 4.2.3 Simulation . . . 29
- 4.3 Results and Discussion . . . 30
  - 4.3.1 Front metal optimization . . . 30
  - 4.3.2 Rear metal optimization . . . 31
  - 4.3.3 Optimal Pattern . . . 33
- 4.4 Conclusion . . . 36

5 Optimizing the metal pattern for different system configurations 37
- 5.1 Introduction . . . 37
- 5.2 Test setup . . . 37
  - 5.2.1 Equator facing system . . . 37
  - 5.2.2 East - West Tilted system . . . 38
  - 5.2.3 East - West Vertical system . . . 38
  - 5.2.4 Irradiation analysis . . . 39
  - 5.2.5 Reference cell . . . 39

5.2.6 Metal pattern variable matrix . . . 40
5.3 Results and discussion . . . 41
5.3.1 Equator facing system . . . 41
5.3.2 East - West tilted system . . . 45
5.3.3 East - West vertical system . . . 49
5.4 Conclusion . . . 52

6 Yield maximizing cell architecture for different climatic conditions 53
6.1 Introduction . . . 53
6.2 Architectures . . . 53
6.2.1 Passivated Emitter Rear Contact solar cell (PERC) . . . 53
6.2.2 Passivated Emitter Rear Locally diffused solar cell(PERL) . . . 54
6.2.3 Passivated Emitter Rear Totally diffused solar cell (PERT) . . . 55
6.2.4 Tunnel Oxide Passivated Contact cell (TOPCon) . . . 55
6.2.5 Hetero Junction Interdigitated Back Contact cells (HJ-IBC) . . . 56
6.3 Climatic suitability of solar cells . . . 57
6.4 Conclusion . . . 59

7 Conclusion 61

A Optimal Tilt 63

B Yield maximizing parameter - additional results 67
B.1 Oceanic Climate - London . . . 67
B.2 Oceanic Climate - Amsterdam . . . 69
B.3 Oceanic Climate - Vancouver . . . 70
B.4 Oceanic Climate - Chongqing . . . 71
B.5 Oceanic Climate - Malabo . . . 72
B.6 Tropical Climate - Singapore . . . 73
B.7 Tropical Climate - Chennai . . . 74
B.8 Tropical Climate - Perth . . . 75
B.9 Tropical Climate - Durban . . . 76
B.10 Tropical Climate - Los Angeles . . . 77
B.11 Hot Desert Climate - Cairo . . . 78
B.12 Hot Desert Climate - Port Louis . . . 79
B.13 Hot Desert Climate - Doha . . . 80

C Metal optimization - additional results 81
C.1 Singapore - albedo : 0.25 . . . 81

D Quokka setting file 83

Bibliography 87

List of Figures

1.1 Rise of Carbon dioxide level in atmosphere . . . 1
1.2 Global average annual net capacity addition by type . . . 2

2.1 Schematic representation of irradiance components on a tilted bi-facial module (left) and vertical bi-facial module (right) . . . 3
2.2 IV characteristics of the bi-facial cell under different albedo conditions . . . 4
2.3 Global maps showing energy yield ratio of Bi_{EW} over Bi_{EF} for different scenarios . . . 5
2.4 Irradiance model . . . 6
2.5 The equivalent circuit of a solar cell with series resistance R_s and shunt resistance R_{sh} . . . 7
2.6 World map of Köppen climate classification for 1901 - 2010 . . . 9
2.7 a - Quokka GUI. b - IV curve of a model simulation . . . 11
2.8 GUI of the BIG EYE simulator . . . 11
2.9 Sky irradiance on a configuration of 2 sheds and a single diffuse reflecting wall behind those sheds . . . 12

3.1 The absolute increase in bi-faciality factor needed to compensate the yield lost due to relative front side efficiency loss . . . 13
3.2 IV curves of theoretical cells with same efficiency . . . 14
3.3 Climate and yield simulation result for London . . . 17
3.4 Oceanic climate : London - performance comparison of different modules . . . 18
3.5 Yield variation with respect to the performance parameters at London . . . 19
3.6 Climate and yield simulation results for Singapore . . . 20
3.7 Tropical Climate: Singapore - performance comparison of different modules . . . 20
3.8 Yield variation with respect to the performance parameters at Singapore . . . 21
3.9 Climate at Doha . . . 22
3.10 Yield simulation results for Doha . . . 22
3.11 Performance of modules at Doha with ground albedo:0.25 . . . 23
3.12 Performance of modules at Doha with ground albedo:0.75 . . . 23
3.13 Yield variation with respect to the performance parameters at Doha (albedo : 0.25) . . . 24
3.14 Yield variation with respect to the performance parameters at Doha (albedo : 0.75) . . . 24
3.15 Yield maximizing parameter at different climatic zones . . . 25

4.1 Trend for remaining silver per cell (156 X156 mm) . . . 27
4.2 TOPCON Architecture, ECN part of TNO . . . 28
4.3 Front metal optimization results . . . 30
4.4 Yield variation with respect to the silver content in solar cell for Oceanic and Hot desert climate at the front metal pattern height of 20 μm . . . 31
4.5 Yield change with finger spacing at finger height of 20 μm for different finger widths . . . 31
4.6 Yield sensitivity to fill factor change at finger height of 20 μm for different finger widths . . . 32
4.7 Effect of rear metal coverage, efficiency and bi-faciality on the yield . . . 32
4.8 Rear metal optimization results for two different climatic zones . . . 33
4.9 Rear metal optimization trend when different front metal pattern is used . . . 33
4.10 Metal pattern optimization results . . . 34
4.11 Yield variation when the optimal patterns for each climate zone is simulated for yield performance at other two climate zones. . . . 36

5.1 Schematic representation of equator facing system used for yield simulation . . . 37
5.2 Schematic representation of east-west tilted system used for yield simulation . . . 38
5.3 Schematic representation of east-west vertical system used for yield simulation . . . 38

5.4 Irradiation profile on $30^{th} June$ incident on the module. a - front irradiance profile. b - rear irradiance profile. c - total irradiance . . . 39
5.5 Results - Front metal optimization of equator facing system configuration . . . 41
5.6 Results - Rear metal optimization of equator facing system configuration . . . 42
5.7 Metal optimization results of the equator facing system . . . 43
5.8 Results - Front metal optimization of East-West tilted system configuration . . . 45
5.9 Results - Rear metal optimization of East-West tilted system configuration . . . 46
5.10 Metal optimization results of the east-west tilted system . . . 47
5.11 Results - Front metal optimization of east-west vertical system configuration . . . 49
5.12 Results - Rear metal optimization of east-west vertical system configuration . . . 50
5.13 Metal optimization results of the East-West vertical system. . . . 51

6.1 Schematic cross section of p-type PERC cell . . . 53
6.2 Schematic cross section of p-tpye PERL cell . . . 54
6.3 a - Schematic cross section of p-type PERT cell. b -Schematic cross section of rear junction n-type PERT cell. . . . 55
6.4 Schematic cross section of -type and p-type TOPCon cells . . . 55
6.5 a - cross section of a typical hetero-junction solar cell. b - cross section of a typical Interdigitated back contact solar cell . . . 56
6.6 schematic cross section and IV,PV curve of record efficient HJ-IBC solar cell . . . 57
6.7 IV curves of the different cell technologies scaled to efficiency of 25% . . . 57
6.8 c-Si cell technologies that are expected to give maximum yield at different regions of the irradiance and temperature. . . . 58

7.1 a - Results of the yield maximizing parameter experiment. b - graph showing solar cell technologies suitable for different climatic conditions . . . 61

A.1 London - Yield at different tilt angles . . . 63
A.2 Amsterdam - Yield at different tilt angles . . . 63
A.3 Chongqing - Yield at different tilt angles . . . 63
A.4 Vancouver - Yield at different tilt angles . . . 63
A.5 Malabo - Yield at different tilt angles . . . 64
A.6 Chennai - Yield at different tilt angles . . . 64
A.7 Los Angeles - Yield at different tilt angles . . . 64
A.8 Singapore - Yield at different tilt angles . . . 64
A.9 Perth - Yield at different tilt angles . . . 64
A.10 Durban - Yield at different tilt angles . . . 64
A.11 Cairo - Yield at different tilt angles . . . 65
A.12 Nairobi - Yield at different tilt angles . . . 65
A.13 Port Louis - Yield at different tilt angles . . . 65
A.14 Doha - Yield at different tilt angles . . . 65
A.15 Variation of optimal tilt with the latitude for different albedo . . . 65

B.1 Yield simulation results for the theoretical modules for different ground albedo at London . . . 67
B.2 yield variation against the variation of different parameters at different albedos. . . . 68
B.3 Yield simulation results for the theoretical modules for different ground albedo at Amsterdam . . . 69
B.4 yield variation against the variation of different parameters at different albedos. . . . 69
B.5 Yield simulation results for the theoretical modules for different ground albedo at Vancouver . . . 70
B.6 yield variation against the variation of different parameters at different albedos. . . . 70
B.7 Yield simulation results for the theoretical modules for different ground albedo at Chongqing . . . 71
B.8 yield variation against the variation of different parameters at different albedos. . . . 71
B.9 Yield simulation results for the theoretical modules for different ground albedo at Malabo . . . 72
B.10 yield variation against the variation of different parameters at different albedos . . . 72
B.11 Yield simulation results for the theoretical modules for different ground albedo at Singapore . . . 73
B.12 yield variation against the variation of different parameters at different albedos . . . 73
B.13 Yield simulation results for the theoretical modules for different ground albedo at Chennai . . . 74
B.14 yield variation against the variation of different parameters at different albedos . . . 74

B.15 Yield simulation results for the theoretical modules for different ground albedo at Perth 75
B.16 yield variation against the variation of different parameters at different albedos 75
B.17 Yield simulation results for the theoretical modules for different ground albedo at Durban . . . 76
B.18 yield variation against the variation of different parameters at different albedos 76
B.19 Yield simulation results for the theoretical modules for different ground albedo at Los Angeles . 77
B.20 yield variation against the variation of different parameters at different albedos 77
B.21 Yield simulation results for the theoretical modules for different ground albedo at Cairo 78
B.22 yield variation against the variation of different parameters at different albedos 78
B.23 Yield simulation results for the theoretical modules for different ground albedo at Port Louis . . 79
B.24 yield variation against the variation of different parameters at different albedos 79
B.25 Yield simulation results for the theoretical modules for different ground albedo at Doha 80
B.26 yield variation against the variation of different parameters at different albedos 80

C.1 Metal pattern optimization results - Singapore 81
C.2 Metal pattern optimization results - Singapore 82

List of Tables

2.1 Albedo values of certain ground surfaces . . . 4
2.2 The climate types used for the analysis . . . 10

3.1 Single diode parameters of reference cell . . . 15
3.2 Modules with highest performance parameter values . . . 15
3.3 yield simulation constraints . . . 15
3.4 Locations chosen for each climatic zones . . . 16

4.1 Front and rear metal pattern data for the reference TOPCon cell . . . 28
4.2 IV parameters of 60 cell module with the reference TOPCon cell . . . 28
4.3 Metal grid parameter variation matrix . . . 29
4.4 simulation constraints used for BIG EYE bi-facial yield simulation . . . 29
4.5 Location with albedo chosen for metal optimization . . . 29
4.6 Optimal metal pattern for different climatic conditions that can be printed using the current/near future technology. . . . 34
4.7 IV parameters of optimal patterns for different climatic conditions that can be printed using the current/ near future technology . . . 35
4.8 Optimal metal pattern (R&D) for different climatic conditions . . . 35
4.9 IV parameters of optimal patterns (R&D) for different climatic conditions . . . 35
4.10 Cost analysis for 50% silver saving . . . 36

5.1 System parameters used for yield simulation . . . 37
5.2 System parameters used for yield simulation . . . 38
5.3 System parameters used for yield simulation . . . 38
5.4 Metal grid patter of the reference cell . . . 40
5.5 IV parameters of the reference cell . . . 40
5.6 Metal grid parameter variation matrix . . . 40
5.7 Optimal patterns for the equator facing system. . . . 43
5.8 IV parameters of the cells with optimal metal patterns . . . 44
5.9 Optimal patterns for the East-West tilted system . . . 47
5.10 IV parameters of the cells with optimal metal patterns . . . 48
5.11 Manufacturable optimal pattern with lesser metal and better yield than the reference cell . . . 51
5.12 IV parameters of the optimized cells . . . 52
5.13 The optimal metal pattern for different system configuration . . . 52

6.1 IV parameters of record efficient PERC solar cell at industrial scale . . . 54
6.2 IV parameters of record efficient industrial scale PERL solar cell . . . 54
6.3 IV parameters of record efficient industrial scale PERT solar cell. . . . 55
6.4 IV parameters of record efficient TOPCon solar cell. . . . 56
6.5 IV parameters of record efficient HJ-IBC solar cell . . . 57
6.6 IV parameters of the c-si solar cells with their efficiency scaled to 25% . . . 58

1

Introduction

Erratic climatic conditions that are observed around the world pose a threat to human existence. Tackling it and creating a sustainable environment is the need of the hour to ensure a progressive future for the human race. The climate change is due to the increase in greenhouse gases like methane, carbon-dioxide, nitrous oxide and CFCs. The NASA states that CO_2 emission is the principal accelerator of the climate change [1]. Figure 1.1 shows the historic levels of CO_2 in the atmosphere. In 2013, CO_2 levels surpassed the historical level of 400 ppm [2]. This drastic increasing in the CO_2 level are due to the burning of fossil fuels. In 2016, Electricity and heat generation was the major contributor of CO_2 emission amounting to 42% of global CO_2 level[3]. Realizing the need for action, 197 countries signed the Paris Climate Agreement (COP21) that aims to limit the green house emission that would limit the global temperature preferably below 1.5°C [4]. Decarbonizing the energy industry is the cost-effective way to reduce the CO_2 in atmosphere to pre-industrial level [5].

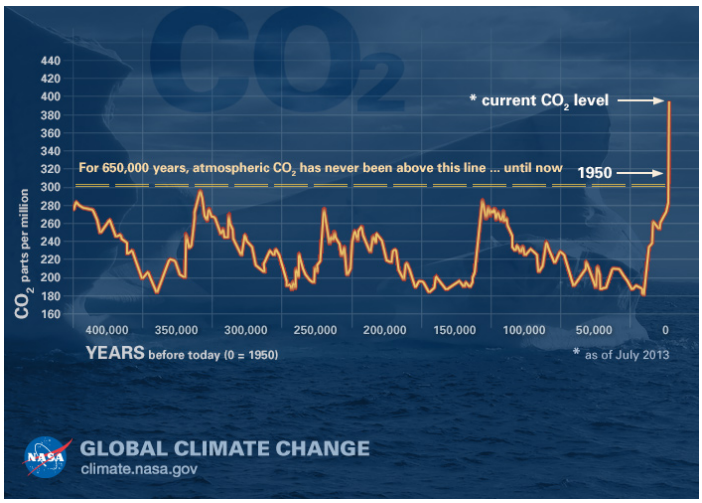

Figure 1.1: Rise of Carbon dioxide level in atmosphere [1]

Figure 1.2 shows that the renewable energy is expected to become the two third of the global energy supply by 2040 [6]. Solar energy has the lower carbon footprint of 3.5 – 12 $g\,CO_2\,eq/kWh$ [7] and is one of the cleanest energy source available. Solar energy has the potential to be a major contributor in our future energy systems. With rapid deployment of large scale photovoltaics by developing nations like China and India is helping solar energy to be the major energy source in the low carbon energy future [6].To support and achieve this growth in deployment of solar energy societal and economical acceptance of the technology must be achieved. Economical acceptance of the technology can be achieved by reducing the Least Cost of Electricity (LCoE) of solar power.

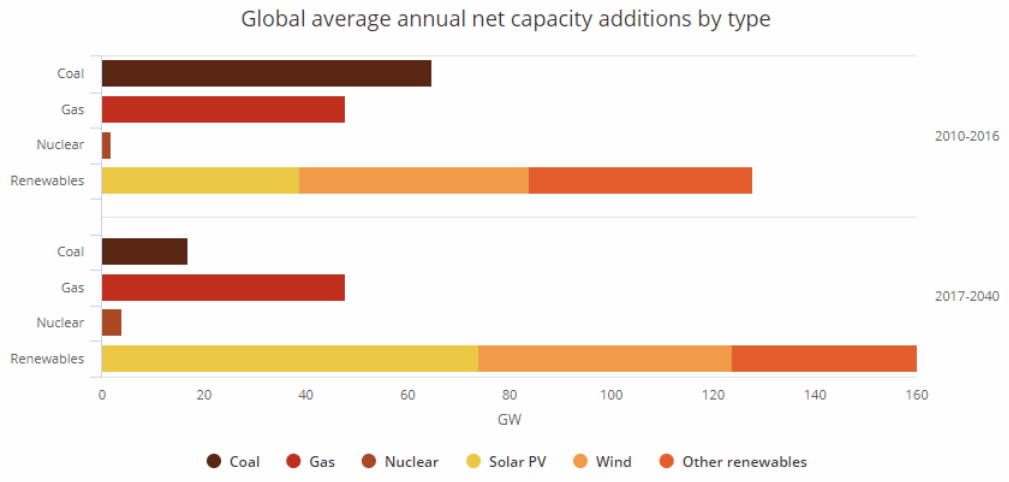

Figure 1.2: Global average annual net capacity addition by type [6]

Bi-facial photovoltaics is one of the advanced technology which has the potential to reduce LCoE by increasing the energy yield. Bi-facial modules produce power from both the sides of the module. Bi-facial PV modules makes use of the diffuse and albedo component of the solar radiation to give additional yield compared to mono-facial modules. Up to 50% bi-facial gain has been reported when compared with the yield of a similar isolated mono-facial module [8].The bi-facial systems can be used in the east-west titled and vertical orientation to match the peak power production to the peak demand. It can also be used as vertical system to reduce soiling. The bi-facial yield gain depends upon a lot of the external parameters like, diffuse radiation, albedo, elevation, tilt angle, etc. This implies that bi-facial yield can vary widely on geographic/climatic conditions. Designing the bi-facial cells, suiting a climatic region to maximize the yield will reduce the LCoE of solar power. This master thesis work aims to identify the optimal design parameters suited for each geographic conditions and analyze whether the geography based design has an economical benefit.

The photo-voltaic cells are usually designed for higher efficiency at standard test condition of $1000 W/m^2$ and $25°C$. But the irradiation and temperature in real time deviates a lot from the STC values. For a better LCoE, it is advisable to design the cells for a better yield at the climatic condition. This motivates the first task of identifying the design parameter that maximizes the yield at different climatic conditions and this knowledge can be used to optimize cells and modules for the best LCoE at that climate.

The silver is the costliest non-silicon component of a solar cell. Bi-facial cells with Ag metal pattern on both the sides (n-type PERT, TOPCon and SHJ) needs more than twice the amount of silver compared to a mono-facial cell. Optimizing the metal grid to the geographic condition for a better yield may reduce the silver content thereby reducing the cost of a cell. The second task aims to identify the optimal pattern for each of the chosen climatic zones while relatively maintaining or increasing the energy yield.

PV system orientation is important to suit the end application. Equator facing systems are used in utility scale systems for their maximum yield. The east-west tilted systems have better usage of space and have good energy yield in smaller area [9]. Vertical systems have increased utilization of land [10]. Each of the orientation at a same climate captures a different intensity of irradiation. This motivates third task to identify the optimal metal pattern for different system orientation.

Cell architectures like HIT, PERC, PERT, Thin-film, tandem cells have their own characteristics that may makes them suited for a particular climatic condition. The fourth and final task is to identify the cell architecture that uses its characteristics to perform the best at each of the climatic zone.

This report is structured into 7 chapters. Chapter 2 of this report deals with the literature study explaining the basics of bi-facial modules, bi-facial yield prediction, climatic zones, solar cell calculators and simulators used etc. Chapter 3 explains the first task of identifying the yield maximizing parameter for different climatic zones. Chapter 4 explains need for the metal pattern optimization and identifies the optimal metal pattern for each of the climatic zone. Chapter 5 identifies the optimal metal pattern for different system orientation. Chapter 6 identifies the cell architecture that has better yield at different climatic conditions. Chapter 7 concludes with the final results of the experiments and lays down the scope for future work.

2

Literature Study

2.1. Bi-facial PV

Bi-facial PV modules effectively collects the irradiation from both front and rear sides, increasing the yield. This is depicted in the figure 2.1. Bi-facial yield gain can be given as the ratio of the yield of a similar mono-facial module to yield of the bi-facial module. Bi-facial yield gains up to 10% are possible at lower albedo of 0.25 [11]. By increasing the albedo, increasing the elevation and reducing the self shading, bi- facial gain up to 30% is possible [11]. This will help reduce the LCoE of the solar energy.

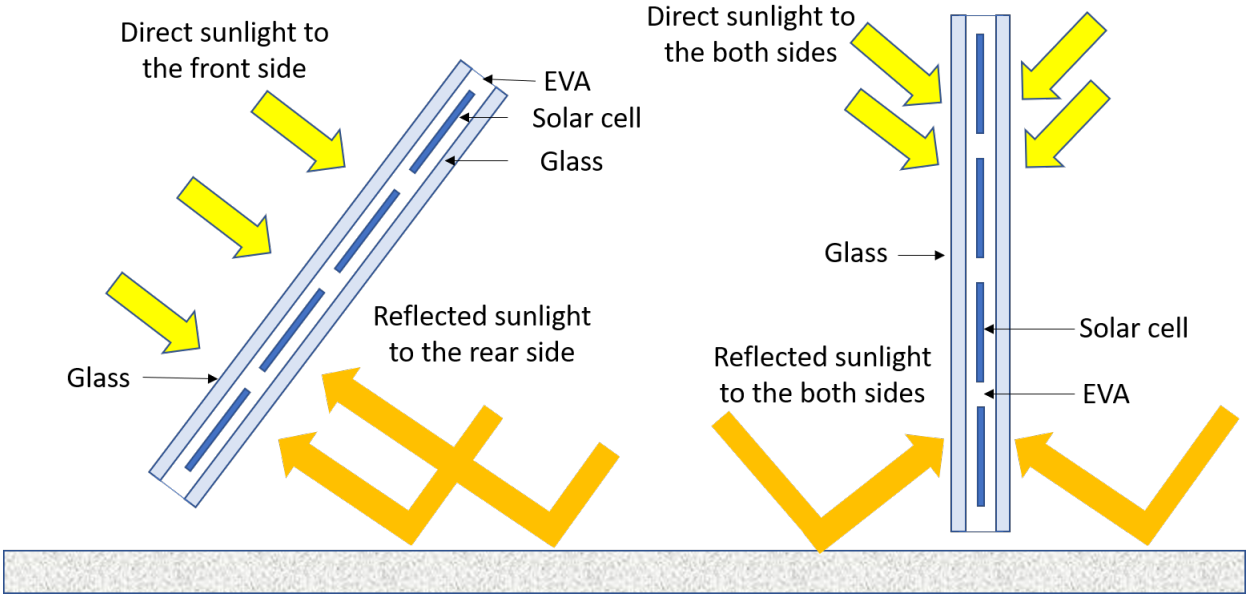

Figure 2.1: Schematic representation of irradiance components on a tilted bi-facial module (left) and vertical bi-facial module (right)

The energy yield of a bi-facial PV module is dependent on the the front side efficiency and bi-faciality factor and are given by the below equations. Bifaciality factor is the ratio of cell efficiency when illuminated on the rear side to the efficiency when illuminated on the front side. Both the parameters are defined at STC conditions which will vary at the operating conditions.

$$\eta_{STC} = \frac{Voc \cdot Isc \cdot FF}{G_{STC} \cdot Area} \tag{2.1}$$

$$\phi = \frac{\eta_{rear}}{\eta_{front}} \tag{2.2}$$

The bi-facial gain strongly depends on the ratio G_{front}/G_{rear} [12]. This shows that the a lot of external parameters like system orientation, module elevation, albedo of the reflecting surface, transparency of the module, clearness index of the sky plays a major role in determining the bi-facial yield. It is essential to optimize the system to the climatic condition to gain the maximum possible energy yield.

2.1.1. Factors affecting bi-facial gain

Albedo

Albedo is the measure of reflection of the solar radiation out of total irradiation received by a body. A body which absorbs all irradiation has an albedo of 0 whereas a body which reflects everything has an albedo of 1. Albedo of the location has large effect on the bi-facial gain. Albedo of a site changes seasonally. Periods of snow or local foliage may change the albedo drastically. Higher the albedo of the reflecting surface, higher the light collected at the rear of the module, G_{rear}. The table 2.1 shows the albedo of different ground surfaces. The yield increases linearly with increase in the albedo. Russel et al [13] shows that albedo significantly affects the thermodynamic efficiency limits resulting in higher output power. The figure 2.2 shows the bi-facial IV characteristics of the bi-facial solar cell under different illumination conditions.

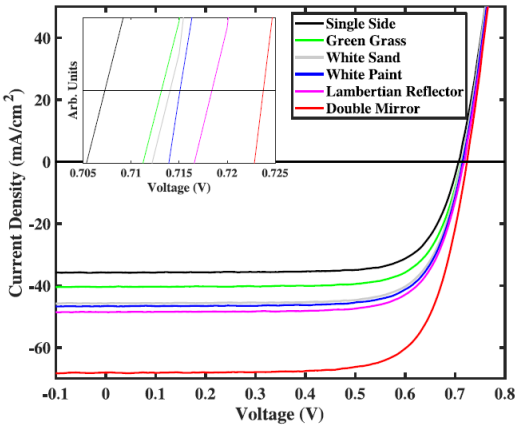

Figure 2.2: IV characteristics of the bi-facial cell under different albedo conditions [13]

Surface Type	Albedo
Green field (Grass)	0.23
Concrete	0.16
White painted concrete	0.6-0.8
White gravel	0.27
White roofing metal	0.56
Light grey roofing foil	0.62
White roofing foil (Solar applications)	>0.8

Table 2.1: Albedo values of certain ground surfaces [14]

Clearness Index

Clearness index K_T indicates the amount of extraterrestrial irradiance that reaches the surface of the Earth. Clearness index can also be attributed as the cloudiness of the sky. During cloud free days ($K_T > 0.75$) the diffuse irradiation received on a horizontal surface is only 12% of the extraterrestrial irradiation outside the atmosphere [15].But during partially cloudy days ($K_T < 0.4$) diffuse irradiation increases upto 25% of the extraterrestrial irradiation [15]. Although overall yield may reduce on a cloudy day due to reduction of direct normal irradiance (DNI), Bi-facial gain will increase as it is a function of diffuse irradiation.

Ground clearance

Ground clearance is a crucial design parameter. The ground clearance of the module from the ground surface reduces the self shading of the module [16] and improves the rear collection of light. Bi-facial yield increases as the clearance increases until the effect of self shading diminishes [11]. Optimal clearance for maximum possible yield reduces as the latitude increase. This is because the self shading effect reduces with higher tilt angle at higher latitudes [11].

Module transparency

Module transparency increases the rear irradiance. Effect of module transparency is more significant when deployed at lower elevation. The effect of increased irradiance decreases as the elevation increases[12].

Azimuth and tilt Angle

The optimal azimuth angle for PV modules is either equator-facing or east-west facing [11]. The tilt angle varies as a function of the latitude, elevation and albedo. Tilt angle must be optimized for the maximum

yield at that location. As we move from the equator, optimal tilt angle increases. The bi-facial equator facing (Bi_{EF}) system has higher tilt angle when compared to a similar mono-facial system. It is because as the tilt increases, the self shading reduces, thereby, increasing the rear irradiance for the bi-facial modules. The east-west system has the optimal tilt angle at 90°[11]. The figure 2.3 shows the performance comparison of equator facing at optimal tilt and vertical east-west system around the world. At low albedo conditions the Bi_{EF} systems outperform the bifacial East-West Bi_{EW} systems as the direct light collection dictates the total yield. Whereas in high albedo conditions, elevation of the system plays a major role. The vertical Bi_{EW} outperforms Bi_{EF} system at zero elevation within the 30°latitude due to the self shading effect of Bi_{EF} system. At higher elevation Bi_{EF} reduces the self shading loses and performs best.

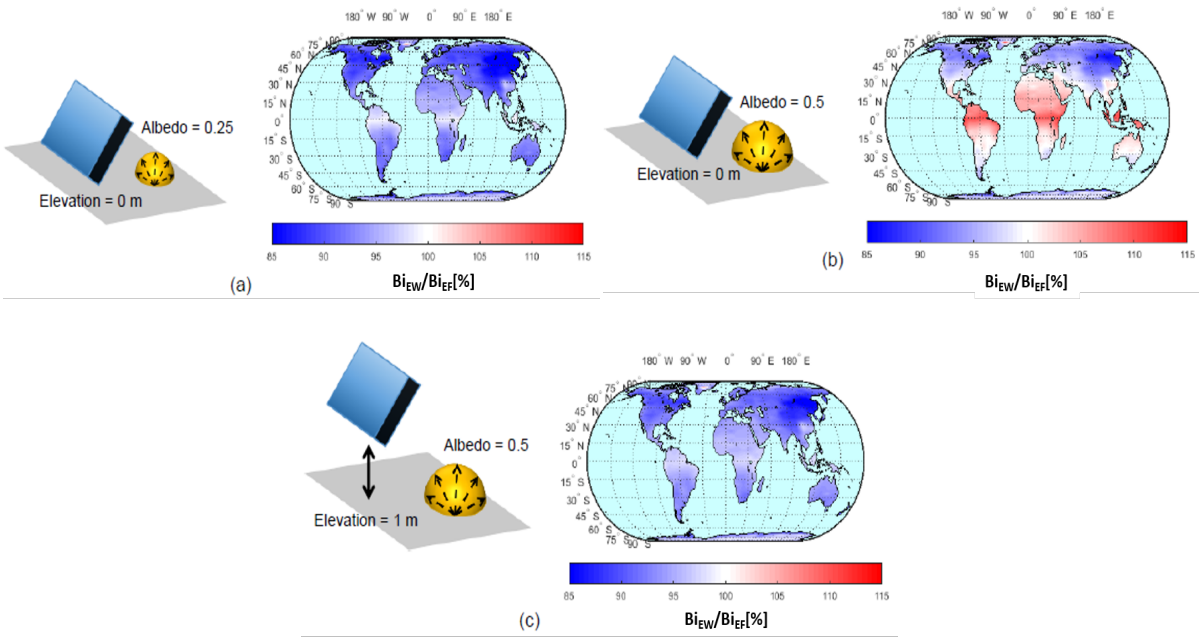

Figure 2.3: Global maps showing energy yield ratio of Bi_{EW} over Bi_{EF} for different scenarios a) ground mounted with ground albedo of 0.25; b) ground mounted with a ground albedo of 0.5 and c) 1 m elevated with a ground albedo of 0.5. Taken from [11]

2.2. Bi-facial energy yield

2.2.1. Irradiance model

The total solar irradiance incident on horizontal surface is called Global horizontal irradiance (GHI). GHI can be decomposed into three components: a) direct normal irradiance (DNI); b) diffuse horizontal irradiance (DHI) c) albedo irradiance. The diffuse irradiance can be decomposed into its angular components: a) isotropic diffuse irradiance ($Diff_{Iso}$) that is received uniformly from all of the sky dome; b) circumsolar irradiance ($Diff_C$) that occurs due to the scattering of light by aerosol particles [11]; c) horizon brightening irradiance ($Diff_H$) is the irradiance that emerges from the Earth horizon.

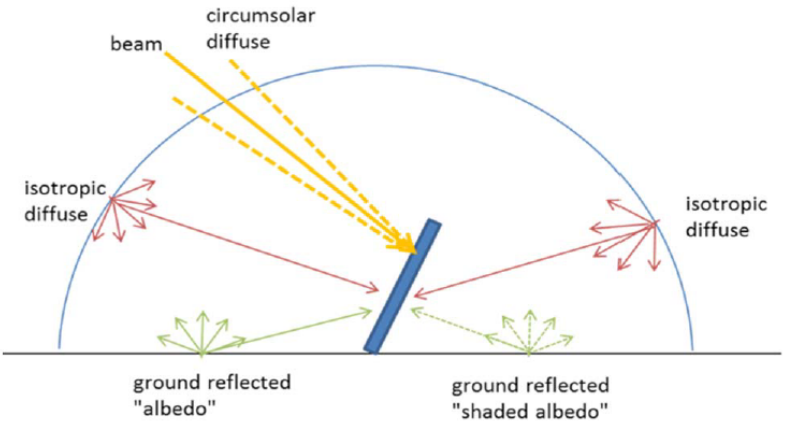

Figure 2.4: Irradiance model

BIGEYE uses Perez model [17] to decompose the diffuse irradiance into its angular components. The albedo irradiance has the ground reflected components of direct, diffuse circumsolar and isotropic diffuse irradiance. The figure 2.4 shows the different components of solar irradiation that is considered for a bi-facial PV module. Below subsections gives the equation to arrive at different irradiance components Equation are adapted from [11].

Direct Irradiance

Direct irradiance can be calculated using the angle of incidence (θ) between G^{DNI} and front/rear surface of the module.

$$G^{direct}_{Front/Rear} = (1 - R_{loss}) \times (GHI - DHI) \times \frac{cos\theta}{cos\theta_z}. \tag{2.3}$$

Where R_{loss} is the reflection loss from the surface of the module [18] .

Diffuse Irradiance

The three components of the diffuse light can be calculated using the below equations.

$$G^{Diff}_{Iso} = (1 - R^{Int}_{loss}) \times Diff_{Iso} \times VF_{M->Sky} \tag{2.4}$$

$$G^{Diff}_{C} = (1 - R_{loss}) \times Diff_{C} \times \frac{cos\theta}{cos\theta_z} \tag{2.5}$$

$$G^{Diff}_{H} = (1 - R_{loss}) \times Diff_{H} \tag{2.6}$$

where $VF_{M->Sky}$ is the module to sky view factor. R^{Int}_{loss} is the integrated reflection loss over the solid angle of isotropic diffuse irradiance. We can use the equations (2.4 - 2.6) to analytically determine the diffuse irradiation on both front and rear surfaces.

Albedo Irradiance

Albedo component of the irradiance is the ground reflected components of the direct and diffuse irradiance. To compute the albedo component careful assessment of self shading by direct, circumsolar diffuse and isotropic diffuse irradiance is necessary [11]. The equation 2.7 gives the albedo component of direct and circumsolar diffuse irradiation.

$$G^{DNI+DIFF_C}_{Alb(Front/Rear)} = \left(1 - R^{Int}_{loss}\right) \times R_A \times \left(G^{DNI} \times cos(\theta_z) + G^{Diff}_{(C)} \times cos(\theta_{z(cir)})\right) \times VF_1 \tag{2.7}$$

where R_A is the ground albedo coefficient, $\theta_{z(cir)}$ is the zenith angle of the circumsolar diffuse light. VF_1 is the view factor that represents a portion of unshaded albedo light. The albedo component due to isotropic diffuse irradiance is given by the equation 2.8.

$$G^{DIFF(Iso)}_{Alb(Front/Rear)} = \left(1 - R^{Int}_{loss}\right) \times R_A \times G^{Diff}_{(ISo)} \times VF_2(H) \tag{2.8}$$

where VF_2 is the view factor which is computed taking the consideration of the self shading, location of the module on the ground. Computing the view factors are very critical for the accurate prediction of the energy yield. Knowing the total intensity of the irradiance incident on the module, the next step it to find the module temperature due to the irradiance and atmospheric temperature.

2.2.2. Thermal model

Determining the module temperature is critical for determining the energy yield as the IV parameters vary with temperature. Bi-facial cells absorb light from both the sides of the panel which increases the temperature of the module but also transmits the infrared light which will simultaneously reduce the temperature of the module [19].

To predict the temperature of module heat balance in the PV module must be determined. The heat balance in a PV module is affected by three main factors: 1) the irradiance on the module; 2) conversion losses by thermalization, recombination or parasitic absorption; 3) heat losses by radiation and convection [19].The BIGEYE yield model gives uses the energy balance model developed by Feiman [20]. The steady state module temperature is given by the below equation 2.9.

$$T_m = T_{amb} + \frac{Q_{tot}}{U_0 + U_1 \times v} [20] \tag{2.9}$$

where T_m is the module temperature, T_{amb} is the ambient temperature, U_0 is the heat transfer coefficienct in $Wm^{-2}K^{-1}$ and U_1 is the heat transfer coefficient in $Wm^{-3}sK^{-1}$ and v is the wind speed. Q_{tot} is the effective heat input and is given by the equation 2.10.

$$Q_{tot} = \alpha_f G_{front} + \alpha_r G_{rear} - P_{elec} \tag{2.10}$$

where G_{front} and G_{rear} are the front and rear irradiance respectively and α_f, α_r are the respective net absorption coefficients. They are given by the $\alpha_i = 1 - R_i - T_i$ where R_i and T_i are reflection and transmission of side i.

2.2.3. Yield determination

The power output of the solar cell depends on the instantaneous module temperature and irradiance conditions. The BigEYE bi-facial yield simulator uses five parameter model devised by Soto et al [21] to determine the IV curve at different operating conditions. The five parameters a_{ref}, $I_{l,ref}$, $I_{o,ref}$, $R_{s,ref}$, $R_{sh,ref}$ are the reference values at STC conditions. The equivalent circuit of a solar cell with the five parameters is given by the the figure 2.5.

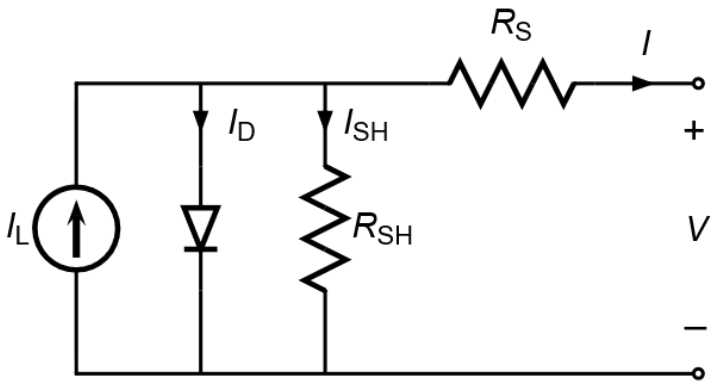

Figure 2.5: The equivalent circuit of a solar cell with series resistance R_s and shunt resistance R_{sh}

The one diode equation used to determine the IV characteristics is given by the below equation 2.11. The parameters a, I_l, I_o, R_s, R_{sh} in the equation 2.11 differs

$$I = I_0 \left\{ exp\left[\frac{q(V - I \cdot R_s)}{a \cdot k_B \cdot T} \right] - 1 \right\} + \frac{V - I \cdot R_s}{R_{sh}} - I_{ph} \tag{2.11}$$

with different operating conditions and are evaluated using their temperature dependence relation. a is the modified ideality factor and it has a linear relation with temperature. The below equation 2.12 will help to determine the ideality factor a operating condition (equation adapted from [21]).

$$\frac{a}{a_{ref}} = \frac{T_c}{T_{c,ref}} \tag{2.12}$$

Where $T_{c,ref}$ and a_{ref} are the values at STC conditions. T_c and a are the values at operating condition. The relation between the diode reverse saturation current and temperature is given by the below equation 2.13.

$$\frac{I_o}{I_{o,ref}} = \left[\frac{T_c}{T_{c,ref}}\right]^3 exp\left[\frac{1}{k_B}\left(\frac{E_g}{T_{ref}} - \frac{E_g}{T_c}\right)\right] \tag{2.13}$$

where k is the Boltmann's constant. The bandgap of the material E_g exhibits a slight temperature dependence which is given by the equation 2.14.

$$\frac{E_g}{E_{g,ref}} = 1 - 0.0002677\left(T - T_{ref}\right) \tag{2.14}$$

The photocurrent I_L is the a linear function of the solar irradiance and it is varies with the cell temperature according with the temperature coefficient $\alpha_{I_{sc}}$. The equation 2.15 gives the I_L at operating conditions.

$$I_L = \frac{S}{S_{ref}}\left[I_{L,ref} + \alpha_{I_{sc}}\left(T_c - T_{c,ref}\right)\right] \tag{2.15}$$

where S_{ref} is the absorbed irradiance at STC conditions. The bifaciality factor is considered for the computation of the irradiance S as given in the below equation [22]. ϕ is the bifaciality factor.

$$S = G_{front} + \phi \cdot G_{rear} \tag{2.16}$$

The R_{sh} is inversely proportional to the short circuit intensities. The equation 2.17 gives the inverse relation of the shunt resistance and the absorbed irradiance. For this work we assume modules with very high shunt resistance.

$$\frac{R_{sh}}{R_{sh,ref}} = \frac{S_{ref}}{S} \tag{2.17}$$

2.3. Climatic zones

2.3.1. Köppen-Geiger climate classification

Köppen climate classification was first introduced by Köppen Geiger in 1884 [23]. It was first aimed to define climate boundaries based on the vegetation present in the zones [24]. Köppen went on to revise his system of classification till his death in 1940. His system was later revised bu Rubel et al [25]. This system of climate classification is widely used in the world [24].

This classification divides the terrestrial climates into 5 major types and given the alphabets A to E to identify it. These five climates are further classified based on the aridity in terms of temperature and precipitation. Certain climates are giver third level of classification to indicate the warmth of the summer and coldness of winter [24].

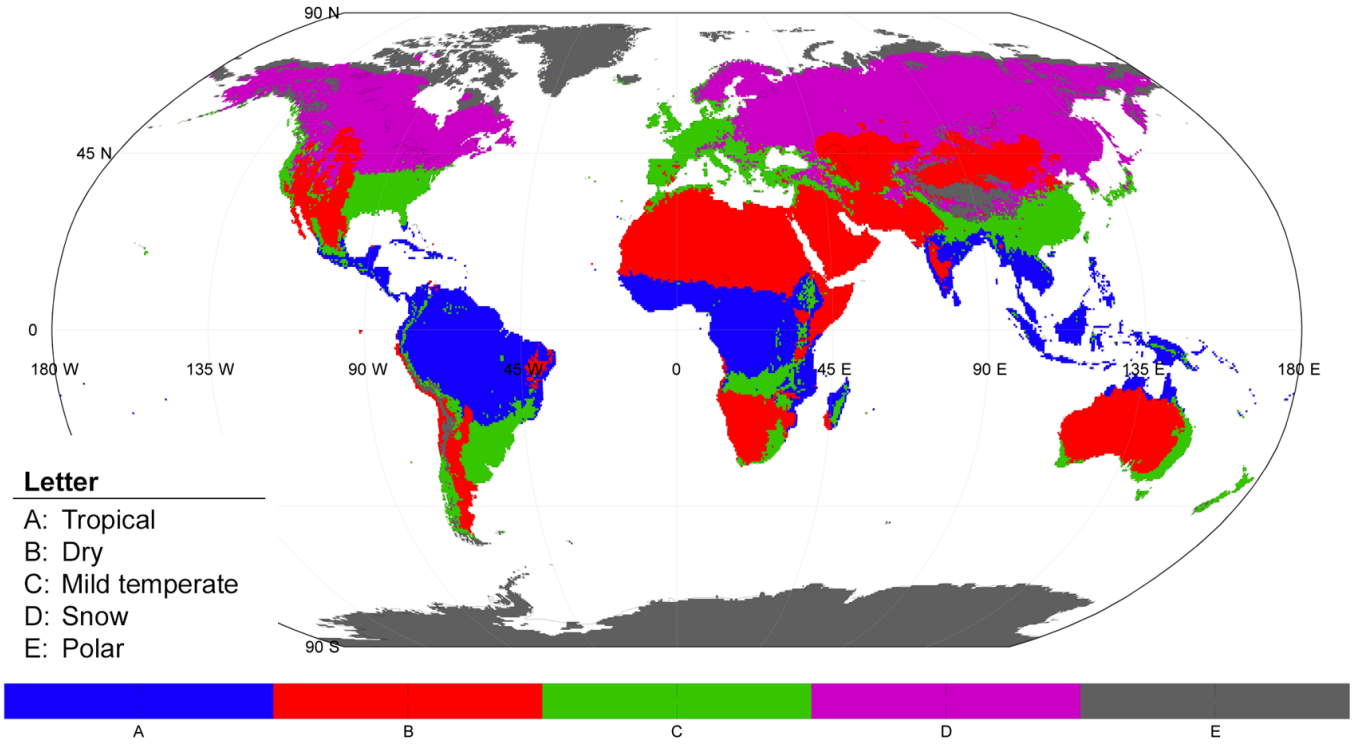

Figure 2.6: World map of Köppen climate classification for 1901 - 2010 [26]

Type A climate - Equatorial

As the name suggests. this climate is found in the low latitude regions, mostly 15 °N and S of the equator. This climatic region can be characterized by no net solar irradiation change among the months and the high temperatures above 18 °C [24]. This Climatic zone can be further classified into three sub zones depending on the precipitation in the driest month.

- Af - Wet equatorial climate
- Am - Tropical monsoon climate
- Aw - Tropical wet-dry climate

Type B climate - Arid and semi arid

These climatic regions are mostly found in 15-30 °latitude regions in both the hemispheres. They are characterized by intense solar irradiation, high temperature and high evaporation [24]. This climate is further sub categorized based on precipitation and temperature.

- BWh - Tropical and subtropical desert climate
- BSh - Mid latitude steppe and desert climate
- BSk - Tropical and subtropical steppe climate

Type C climate - Mild temperature

This climate can be found in the latitude regions of 20 to 55 °. This climatic zone can be characterized when the temperature of the warmest month is more than 10 °C and temperature of the coldest month is between -3 °C and 18 °C [24]. This climate is further sub categorized into six climate zones.

- Cfa, Cwa - Humid subtropical climate
- Csa, Csb - Mediterranean climate
- Cfb, Csb - Marine west coast climate

Type D climate - Snow

This climate can be found in the high latitude regions of 40 to 70 °. A region falls under this category when the temperature of its warmest month is greater than or equal to 10 °C and temperature of the coldest month is less than -3 °C [24]. This climate is further sub categorized into eight sub climates.

- Dfa, Dfb, Dwa, Dwb - Humid continental
- Dfc, Dfd, Dwc, Dwd - Continental subarctic climate

Type E climate - Polar

Regions with this climatic zones are present in high latitudes of 60°and higher. These zones can be characterized by the temperature of the warmest month less than 10°C. This climatic zone is further sub categorized into two zones.

- ET - Tundra climate
- EF - Snow and ice climate

2.3.2. Climate zones considered for analysis

For the purpose of analysis, only 4 major climates were chosen for the analysis. Polar regions are not considered for the analysis. In the rest of the chapters the following nomenclatures are used when addressing a climatic zone.

Climate	Type
Oceanic / Temperate	Type C
Tropical / Humid sub tropical	Type A
Arid / Hot desert	Type B

Table 2.2: The climate types used for the analysis

2.4. Simulators

2.4.1. Quokka cell simulator

Quokka is a free software tool simulation of silicon solar cell devices created by Andreas Fell [27]. It employs simplifications like namely quasi-neutrality and conductive boundaries to the general semiconductor carrier transport model to provide fast and accurate solution. Quokka uses inputs like sheet resistance of regions, effective recombination characteristics of emitter and back surface field etc to solve for electrical characteristics of the solar cell like V_{oc}, J_{sc}, MPP, light and dark IV curve and quantum efficiency (QE) curve.

Quokka simulator solves known set of general transport equation for minority and majority carriers, Poisson's equation for the electrical potential etc with loss of generality. The solar cell model used in the quokka simulator is defined by Andreas Fell in [27].The basic equations solved in the quokka can be simplified into two differential equations describing the steady state charge carrier transport in a quasi-neutral semiconductor.

$$\nabla\left(\sigma_n \nabla \phi_{Fn}\right) = q\left(G - R\right) \tag{2.18}$$

$$\nabla\left(\sigma_p \nabla \phi_{Fp}\right) = -q\left(G - R\right) \tag{2.19}$$

where ϕ_{Fn} and ϕ_{Fp} are the quasi fermi potentials of electrons and holes. Boundary conditions are applied to solve for ϕ_{Fn} and ϕ_{Fp}. The boundary conditions are not included in this text as it goes beyond the scope of this work. The conductivities σ are given by the below equations as a function of their mobilities μ.

$$\sigma_n = qn\mu_n \tag{2.20}$$

$$\sigma_p = qp\mu_p \tag{2.21}$$

To calculate recombination rate R, Auger, Radiative and Shockley-Read-Hall recombination are taken into account. The total recombination is then computed as the sum of all recombination rates or they can be

stated as fixed bulk recombination rate. At boundaries the recombination rate is denoted by Jo (Refer to the the appendix D). Recombination factor can be effectively switched off by using very high life times. Recombination, resistive properties of the different layers should be stated as shown in the appendix D.

$$R = \Sigma R_{SRH,Custom} + R_{SRH,BO} + R_{Auger} + R_{Rad} + R_{\tau b,fixed} \tag{2.22}$$

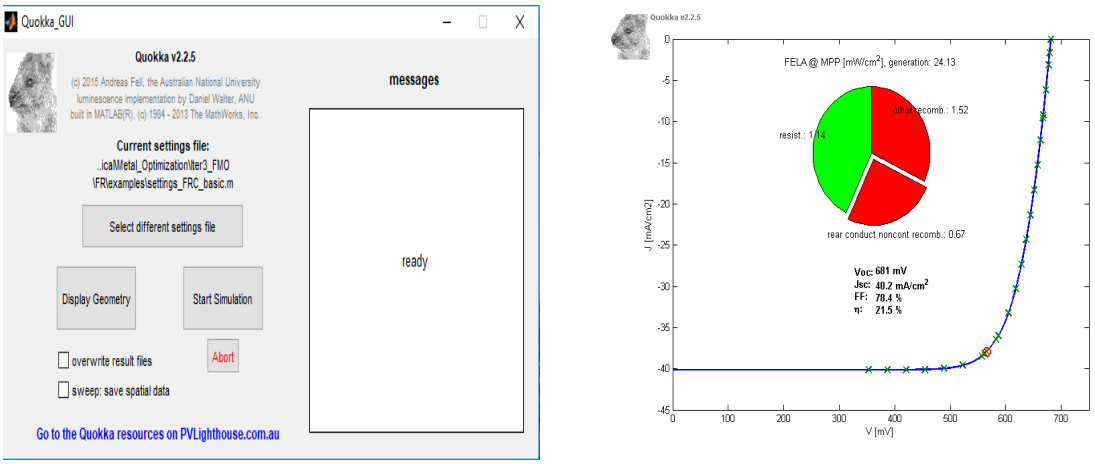

(a) (b)

Figure 2.7: a - Quokka GUI. b - IV curve of a model simulation

Quokka uses a setting file to define the solar cell structure to be simulated. The generation profile file should be an input in the settings file. The required output can be configured via the settings file. The setting file can be created using the file generator available in quokka website [28]. A model setting file for reference is made available in the appendix D. The figure 2.7a shows the GUI of the quokka simulator where the setting file can be loaded and simulated. The figure 2.7b shows a typical result display.

2.4.2. BIGEYE - Bi-facial yield simulator

BIGEYE is a highly accurate bi-facial yield simulator developed by ECN part of TNO [29]. The BIGEYE supports configurable system parameters like size, pitch, tilt angle, azimuth, ground clearance, albedo of the ground etc, the module parameters like dimensions, cell size, thermal coefficient, transparency and cell parameters like the five parameters representing the module IV curve at STC [21]. BIGEYE simulator is very versatile that it can predict the yield of both fixed axis systems and single axis tracking systems.

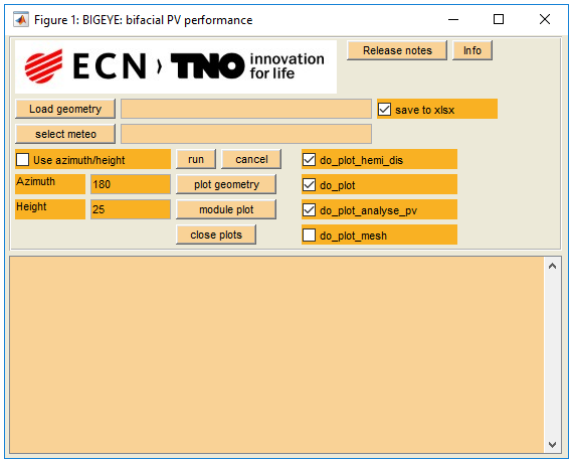

Figure 2.8: GUI of the BIG EYE simulator

BIGEYE uses irradiance model explained in chapter 2.2.1 with 3 dimensional view factors for each panel. All the shading effects caused by other modules in the systems are also considered in calculating the view

factors. The sky irradiance on the a 2 shed model using BIGEYE is shown in the figure 2.9. The temperature of the module is predicted using the temperature model described in chapter 2.2.2. The temperature model uses the ambient temperature and wind speed from the meteorological data provided to the simulator. The electrical output is predicted using the electrothermal model by DeSoto [21].

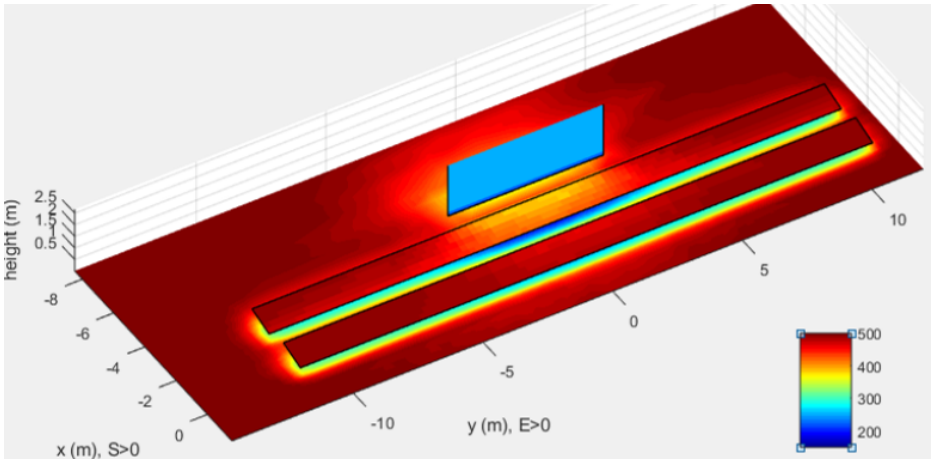

Figure 2.9: Sky irradiance on a configuration of 2 sheds and a single diffuse reflecting wall behind those sheds [29]

The BIGEYE simulator uses an excel configuration file for the defining the system, module and cell parameter. It can also be used to study the yield variation due to varying parameters.The design of experiments (DOE) option in configuration file can be used to specify the varying parameters and theire values.

3

Yield maximizing parameter

3.1. Introduction

The section 2.1 explains the dependence of bi-facial yield on climatic conditions, module installation etc. Now, we can discuss the importance of two major contributors of yield at a given location, the front side efficiency and bifaciality factor. Usually, the front side efficiency and bi-faciality factor are related to each other and after a certain threshold, one cannot be increased without the cost of the other. So, it is important to identify how much of the efficiency reduction can be compensated by increase in bi-faciality factor. An experiment was designed to find the whether the front side efficiency can be compromised to increase bi-faciality factor in a tilted PV system. The energy yield for different locations for a single module, North - South facing system was simulated using BIGEYE software 2.4.2. Simulations were carried out for different combinations of efficiency and bifaciality factor for ground albedo values varying from 0.2 to 0.8. The yield data matrix was used to find the bifaciality factor increase needed to compensate for the relative efficiency decrease.

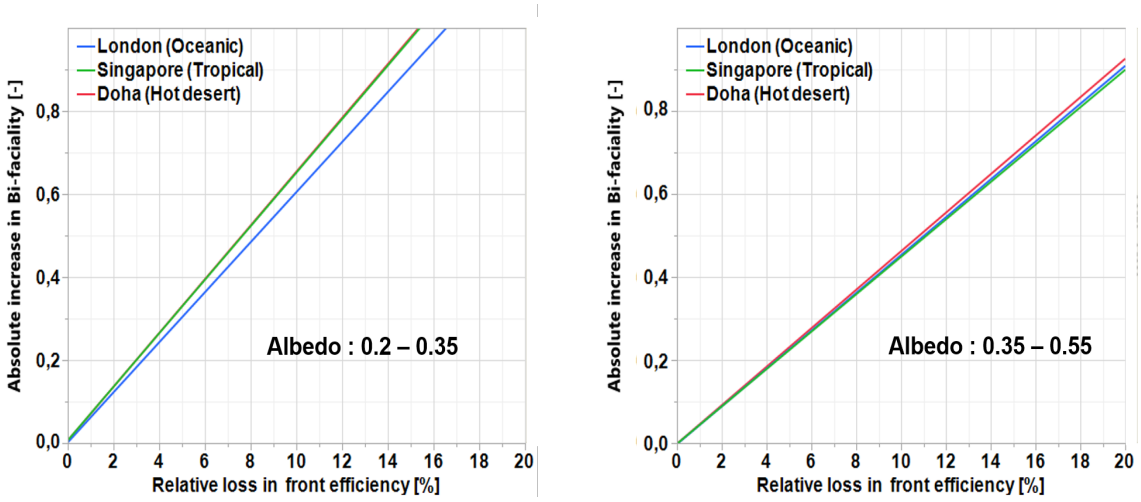

Figure 3.1: The absolute increase in bi-faciality factor needed to compensate the yield lost due to relative front side efficiency loss at different albedo ranges. The figure in the left shows the data for low albedo range of 0.2 - 0.35. The figure in the right shows the data for high albedo range of 0.35- 0.55

The graphs in the figure 3.1 shows the bi-faciality factor needed to compensate the yield lost due to relative front side efficiency loss at different albedo ranges. In the low albedo range, energy yield lost due to 10 % loss of relative efficiency can be compensated by increase in absolute bi-faciality factor of 0.6 and in the mid albedo range, 10% front efficiency loss can be compensated by increase in the bi-faciality of 0.5 to maintain the yield. For instance for a cell with a bi-faciality factor of 0.7, compensating the 10% efficiency loss with 0.6 increase in bi-faciality factor is impossible. This data clearly shows yield loss due to small percentage loss of

front side efficiency cannot be compensated fully. So, the front side efficiency is the major contributor to the yield. It is obvious that contribution of bi-faciality to the yield increases with albedo increase but its is not very significant. Also, there is hardly any difference in trend between different climatic zones.

Front efficiency being the major contributor to the yield, it is important to study which of the parameters in the efficiency equation helps maximize the yield at different climatic conditions.

The cell design is usually optimized for maximum efficiency at standard test condition of $1000 W/m^2$ and $25°C$. But, a STC efficiency can be achieved through different IV curves and their conversion efficiency at non STC conditions will be different. We must identify the IV curve at which has high conversion efficiency at the climatic condition of the location. So, the cell must be optimized for an IV curve suitable for the location. This ensures more yield for same cost, a better LCoE will be obtained. This chapter explains the experiment devised to identify the parameters of the solar cell that needs to be improved for a better yield at different climatic regions.

The next section, 3.2 gives the details about the parameters considered for the test, assumptions made, tools used for simulation etc. The section 3.3 provides the results of the experiment at certain chosen locations, analyses the yield trend, find the yield maximizing parameter for each of the locations. The section 3.4 consolidates the results and concludes with the relation between climate and yield maximizing parameter.

3.2. Test setup

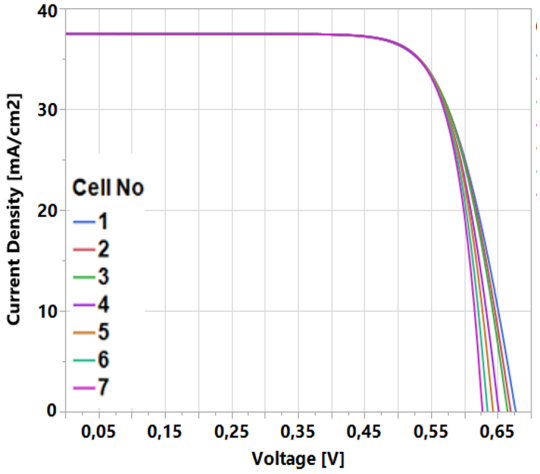

(a) IV curves with same J_{sc}

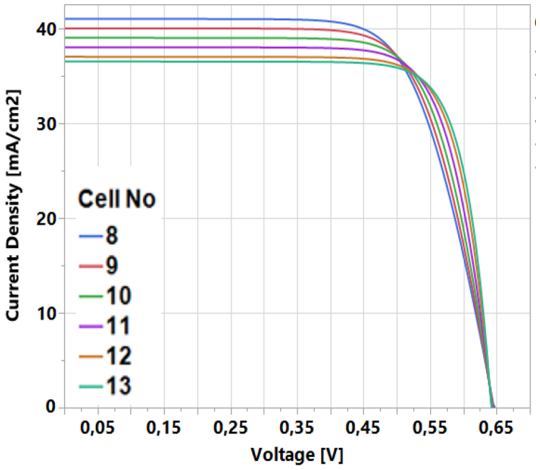

(b) IV curves with same V_{oc}

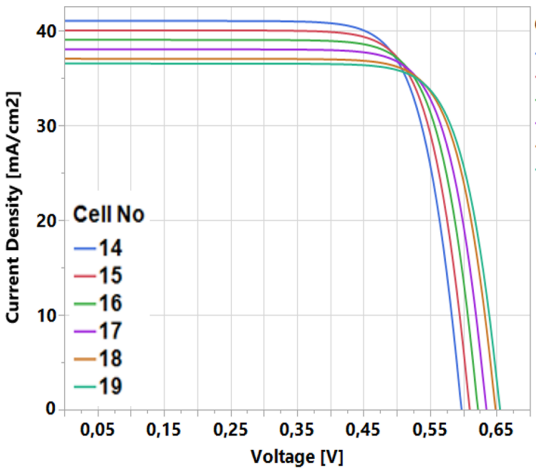

(c) IV curves with same FF

Figure 3.2: IV curves of theoretical cells with same efficiency

The first step in the experiment was to create a set of theoretical cells with same efficiency but different IV curve parameters. The online Equivalent circuit calculator [30] from the PV lighthouse website was used to design the theoretical cells with same efficiency. A reference cell was taken and the single diode parameters, J_l, J_o and R_s were adjusted to form different cells with same efficiency. The table 3.1 tabulates the single diode parameters of the reference cell. The change in the diode parameters translated into the change in I_{sc} ,V_{oc} and FF respectively. The theoretical cells were translated to the modules with 60 cells connected series. Total of nineteen theoretical modules with total area efficiency of 16.5 % and bi-faciality factor of 0.8 was considered.

$I_l(A)$	$I_o(A)$	$R_s(Ohm)$	$R_{sh}(Ohm)$
9.21	5.32e-08	0.51	5000

Table 3.1: Single diode parameters of reference cell

The first set of the cells were designed with I_l same as that of the reference cell shown in the table 3.1. I_o and R_s were varied to maintain the efficiency constant. The second set of the cells were designed with I_o same as that of the reference cell and the third set of cells were designed with R_s same as that of the reference cell. First set of modules had constant I_{sc} but varying V_{oc} and FF. The second set of modules had constant V_{oc} but varying I_{sc} and FF. The third set of modules had constant FF but varying I_{sc} and V_{oc}. The IV curves of the theoretical cells are shown in the figures 3.2a, 3.2b and 3.2c.

Since there might be one or more IV parameters that might be important for yield maximizing for a climatic zone, the products $V_{oc} \times I_{sc}$, $I_{sc} \times FF$ and $V_{oc} \times FF$ were also considered along with I_{sc}, V_{oc} and FF. Of the 19 modules considered, module no 1 had the highest V_{oc}. Module 8 had the highest $V_{oc} \times I_{sc}$ product. Module 13 has highest FF and highest $V_{oc} \times FF$ product. Module 14 has highest I_{sc} and $I_{sc} \times FF$ product. The table 3.2 summarizes this.

Module No.	**Parameter**
1	V_{oc}
8	$V_{oc} \times I_{sc}$
13	FF, $V_{oc} \times FF$
14	I_{sc}, $I_{sc} \times FF$

Table 3.2: Modules with highest performance parameter values

The BIGEYE software [29] (ECN.TNO Bi-facial PV yield simulator) was used to calculate the yield of the modules for a range of locations. To reduce the system variables certain assumptions were made for this experiment. This study will be conducted on a equator facing system. The yield was simulated for a single module system as to remove the effect of direct shading from the yield simulation. The module tilt will be optimized for the maximal yield at the location. The results of the optimal tilt experiment is shown in Appendix A. The module will be placed at an elevation of $0.5m$ from the ground to minimize self shading. The yield was simulated for the albedo values of 0.25, 0.5, 0.75. The table 3.3 shows the simulation constraints considered for the experiment.

Parameter	**Value**
System size	1 module
Orientation	Equator facing - Portrait
Elevation	0.5 m
Tilt	Optimized for location
Module Bi-faciality	0.8
Albedo	0.25,0.5 & 0.75

Table 3.3: yield simulation constraints

13 locations were selected across different climatic zone as shown in the table 3.4. The location selection was based on the Koppen climate classification, explained in section 2.3. The meteorological data for the location was extracted from PVGIS website [31].

Climate	Location	Country
Oceanic / Temperate	London	UK
	Amsterdam	Netherlands
	Vancouver	Canada
	Chonqing	China
	Malabo	Equatorial Guinea
Tropical / Humid sub tropical	Singapore	Singapore
	Chennai	India
	Perth	Australia
	Durban	South Africa
	Los Angeles	California
Hot semi arid / Desert	Doha	Qatar
	Port Loius	Madagascar
	Cairo	Egypt

Table 3.4: Locations chosen for each climatic zones

The hourly meteorological data was considered for yield measurement. To analyze the performance of each module, conversion efficiency and performance ratio of the module at each instance of the yield measurement were considered.

$$ConversionEfficiency(\eta_i) = \frac{Pmpp_i}{G_i \cdot Modulearea} \tag{3.1}$$

The conversion efficiency is the ratio of the power generated to the irradiation incident on the module and is represented by the equation 3.1 and the performance ratio is the ratio of actual energy produced to the energy that will be produced at standard test condition and is computed using the equation 3.2. G_i denotes the sum of the front in-plane irradiance and rear irradiance on the module at an instance i.

$$PerformanceRatio(PR) = \frac{Yield_i}{G_i \cdot Modulearea \cdot \eta_{module}} \tag{3.2}$$

3.3. Results and Discussion

The yield simulations showed that some specific modules performed better at certain climates. When the data was analyzed, the yield was higher in climatic region when a particular IV parameter was higher. Below subsections explain the yield variation and its relation to the IV parameters at different climatic zones. The bifaciality factor is not considered in the analysis. It will be addressed in the upcoming chapters.

3.3.1. Oceanic Climate - London

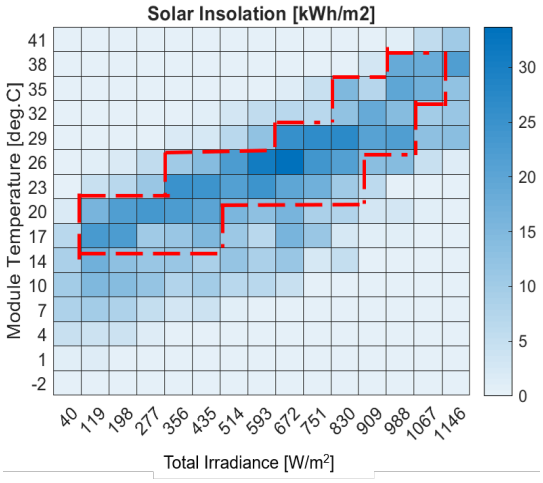

(a) Distribution of annual solar insolation. The region marked by the red lines is the bins of significance with major contribution to the annual solar insolation.

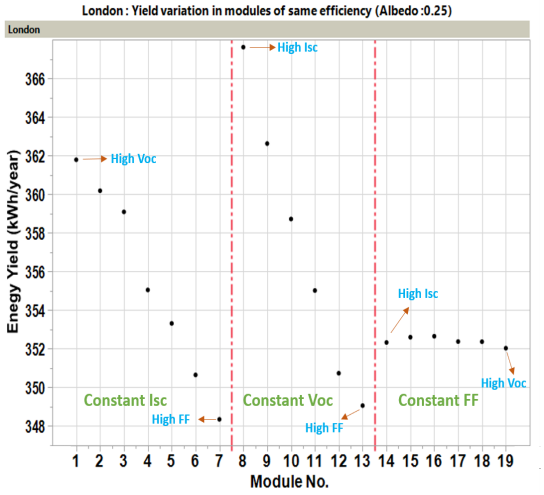

(b) Simulated yield for theoretical modules at albedo of 0.25. The red dotted lines are to indicate the separation between the three sets of modules with constant Isc, constant Voc and constant FF

Figure 3.3: Climate and yield simulation result for London

London is classified as an oceanic climate under the Köppen climate classification (Refer section 2.3). Oceanic climate has low irradiance conditions with warmest month temperature not more than 20 °C. It has long periods of overcast skies and modest annual rainfall. The figure 3.3a shows solar insolation data over range of irradiance and module temperature bins. We can notice there is almost equal distribution of insolation over a wide range of the irradiance and temperature.

The figure 3.3b shows the variation in yield for different modules with same efficiency at ground albedo of 0.25. There is a yield variation of 5.4%. The modules 1 to 7 are the modules with constant I_{sc}. The V_{oc} and FF are varied to maintain a constant efficiency. The module 1 has high V_{oc} and low FF. The module 2 has slightly lower FF and higher FF than module 1. This trend continues and thus the module 7 has lower V_{oc} and higher FF. We can notice that the module with high V_{oc} gives a better yield than with high FF. Similarly when we consider the modules 8 to 13 with constant V_{oc} and varying I_{sc} and FF, module 8 has higher I_{sc} and the module 13 has higher FF. The module with higher I_{sc} has a better yield than the module with higher FF. But when we consider the module set 14 to 19 with constant FF, there is no significant change in the yield when I_{sc} and V_{oc} are varied. This shows that under this climatic conditions V_{oc} and I_{sc} play equal part in contribution to the yield.

We can now analyze each modules using the performance ratio. We can consider the modules 1,8,13,14 which have highest V_{oc}, highest $V_{oc} \times I_{sc}$, highest FF and highest I_{sc} respectively. Performance ratio is computed by the formula 3.2.

The figure 3.4 shows the performance of each module considered. The region marked by the red lines in the graph is the region of significance with major contribution to the total annual insolation in the location. In this climate condition we can notice that module number 8 shown in figure 3.4b has the best performance ratio in the region of significance. This module has the highest $V_{oc} \times I_{sc}$ product, whereas the module number 13 shown in figure 3.4c has poor performance ratio in region of significance. Higher $V_{oc} \times I_{sc}$ implies that the cell must have more active area and less recombination. It should also be noted that the this module has the lower FF. It clearly indicates that we can reduce the metal content, thereby reducing the FF. Now, we have to see if there is a trend in the data where increasing $V_{oc} \times I_{sc}$ would increase the yield.

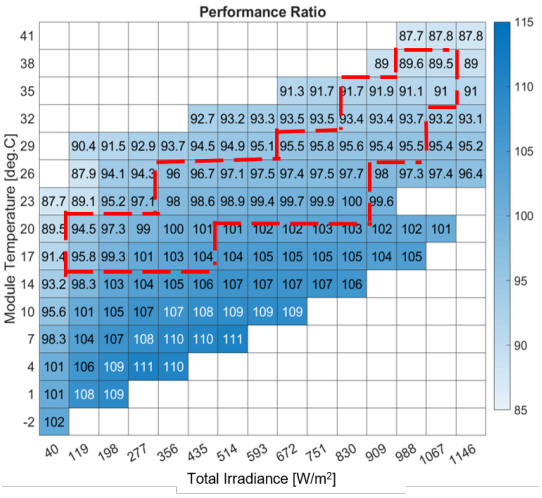

(a) Performance of module #1 with high V_{oc}

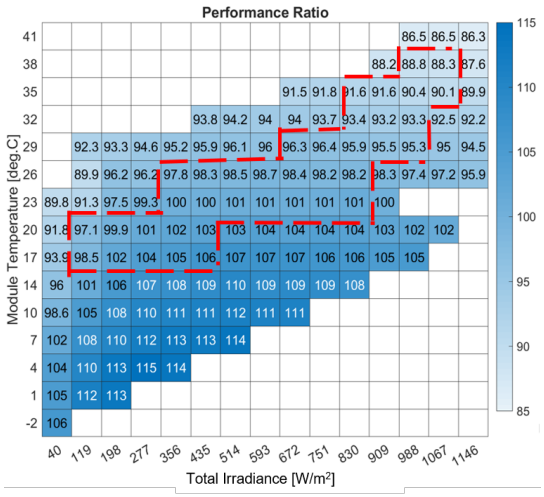

(b) Performance of module #8 with high $V_{oc}xI_{sc}$

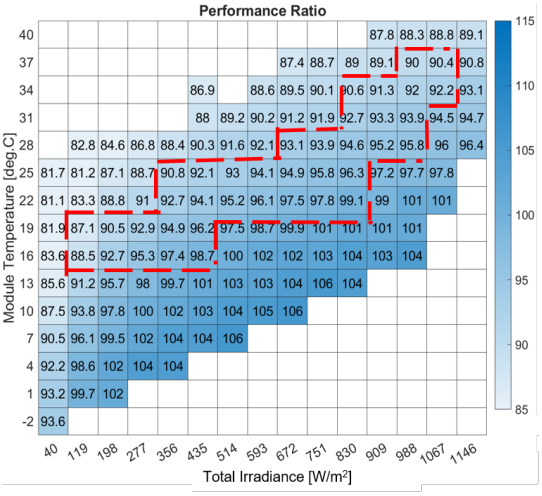

(c) Performance of module #13 with high FF

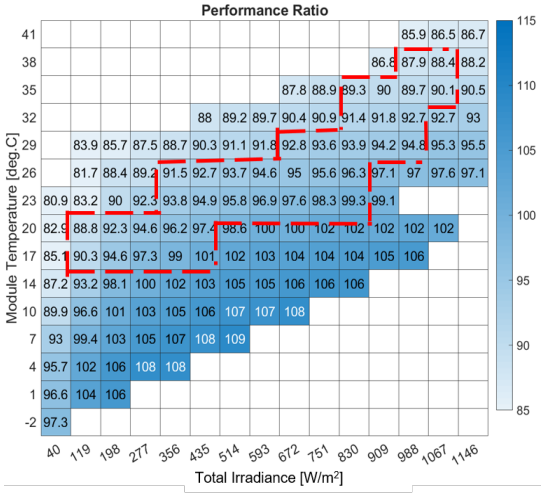

(d) Performance of module #14 with high I_{sc}

Figure 3.4: Oceanic climate : London - performance comparison of different modules

To identify the trend and support our conclusion, SAS JMP statistical software was used. The yield data was fitted against the variables I_{sc}, V_{oc}, FF, $V_{oc} \times I_{sc}$, $V_{oc} \times FF$ and $I_{sc} \times FF$. The variables were arranged in the order of goodness of fit. The variable with the the best fit will have good correlation with the yield at the location.

The graphs in figure 3.5 are arranged in the order of the best fit. It is understandable that the graphs for other three parameters considered FF, $I_{sc} \times FF$, $V_{oc} \times FF$ are mirror images of the $V_{oc} \times I_{sc}$, V_{oc}, I_{sc} respectively. It is very clear from the graphs that the parameter $V_{oc} \times I_{sc}$ has the best linear fit with the yield. This proves that by increasing the the $V_{oc} \times I_{sc}$ product yield can be improved at locations under oceanic climate.

This trend was also seen at Amsterdam (oceanic), Vancouver (oceanic) climates too. So we can generalize that for oceanic climates, the modules with higher $V_{oc} \times I_{sc}$ product will convert the light effectively. This can be attributed to the fact that that these regions have relatively low currents due to lower irradiation. The lower the currents, the less significant the series resistance (Rs) becomes in determining the energy yield. On the other hand, a high I_{sc} improves efficiency at low irradiance conditions. So, while designing the cell for these regions, FF can be reduced in favour of higher I_{sc} and V_{oc}. Thus, $V_{oc} \times I_{sc}$ is the yield maximizing parameter at oceanic climate.

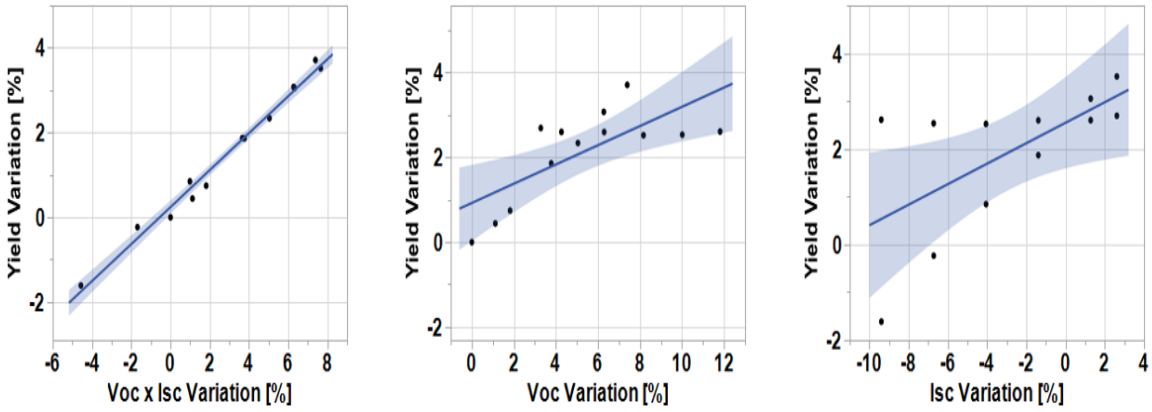

(a) $V_{oc} \times I_{sc}$ (b) V_{oc} (c) I_{sc}

Figure 3.5: Yield variation with respect to the performance parameters at London (albedo :0.25). The fitted data is arranged in the order of best fit.

3.3.2. Tropical climate - Singapore

Singapore lies one and a half degrees above equator and is classified as a tropical equatorial climate under Koppen climate classification. It has no distinct seasons. Climate is hugely influenced by geographic location and maritime exposure. Temperature varies between $25-33°C$ with high humidity and abundant rainfall. The figure 3.6a shows the distribution of solar insolation data. It can be noted from the graph that even at the lowest irradiation situation, the temperatures are well above $26°C$. Data spread is linear confined to a narrow region. The region marked by the red lines is the region of significance with major contributions to the total annual insolation.

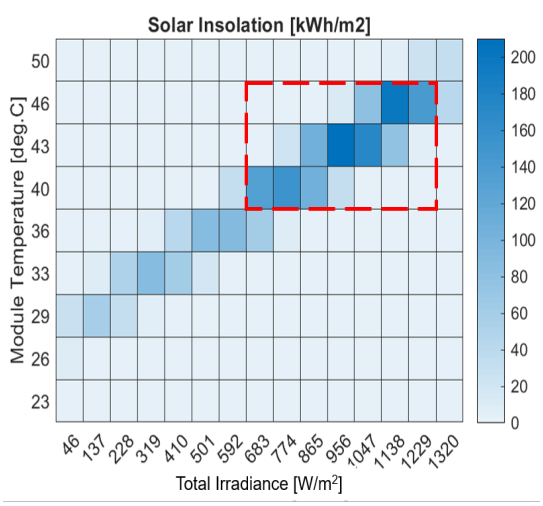

(a) Distribution of annual solar insolation. The region marked by the red lines is the bins of significance with major contribution to the annual solar insolation

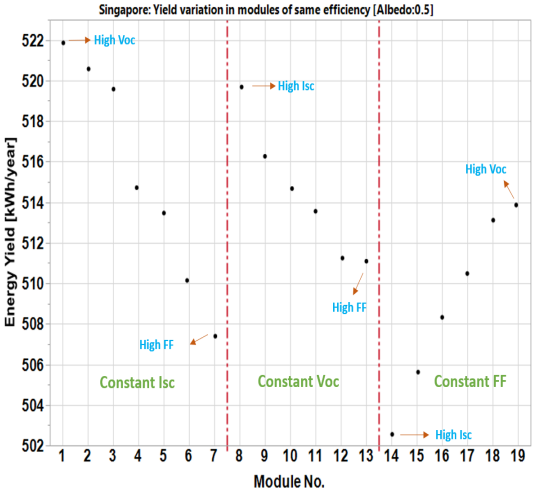

(b) Simulated yield for theoretical modules at albedo of 0.5. The red dotted lines are to indicate the separation between the three sets of modules with constant I_{sc}, constant V_{oc} and constant FF

Figure 3.6: Climate and yield simulation results for Singapore

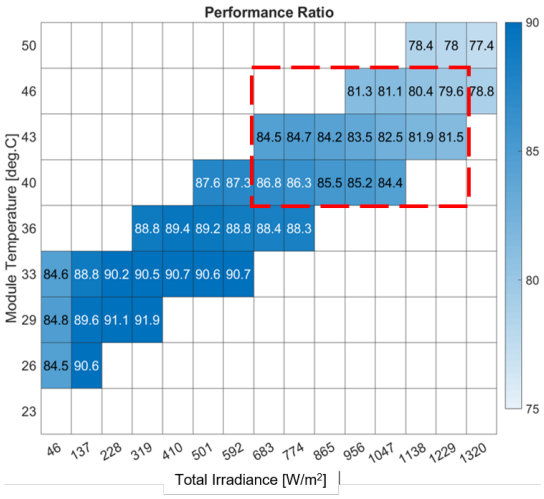

(a) Performance of modules with highest $V_{oc} \times I_{sc}$

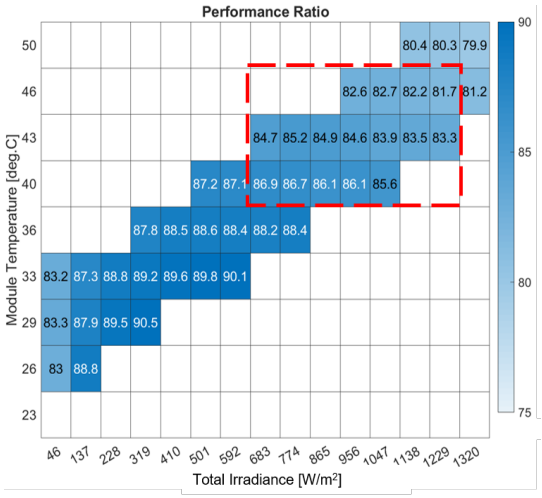

(b) Performance of modules with highest V_{oc}

Figure 3.7: Tropical Climate: Singapore - performance comparison of different modules

When the theoretical modules were simulated for yield at Singapore, there was a yield change of up to 4% and the yield trend was slightly different than the one noted at oceanic climate (London). When comparing this with trend at London (3.3b) we can notice that module no 1 performs best at Singapore when compared to the module no 8 at London. Module no 1 has the highest V_{oc} of the lot and module no 8 has the highest $V_{oc} \times I_{sc}$. Module 1 overtaking the module 8 shows that as the irradiation and temperature increases, V_{oc}

influences the yield more than I_{sc}. This can be clearly seen in the trend of modules 14 - 19. With constant FF the module 19 with high V_{oc} gives more yield than the module 14 with high I_{sc}. As done in the previous we can compare the modules performance using the performance ratio.

The yield difference between the module no 1 and module no 8 is very minimal. The figure 3.7a and 3.7b shows the performance ratio in different regimes of Singapore climate. The region marked by the red lines in the graph is the region of significance with major contribution to the total annual insolation in the location. When we observe the performance ratio of the module no 8 and module 1 in the region of significance, module 1 with highest V_{oc} has better performance than module 8 high $V_{oc} \times I_{sc}$.

When we compare the yield of different modules in the Singapore (3.6b) to that of the London (3.3b) there is trend change in the yield data for module set (Module no 14-19) with constant FF. Modules at London at constant FF performed similar showing that the parameters V_{oc} and I_{sc} are equally important. But in Singapore at constant FF, the module no 14 (High I_{sc}) performs lower at all irradiation conditions than module no 19 (High V_{oc}).This shows that we have to give more importance to V_{oc} when compared to I_{sc} at this climatic conditions.

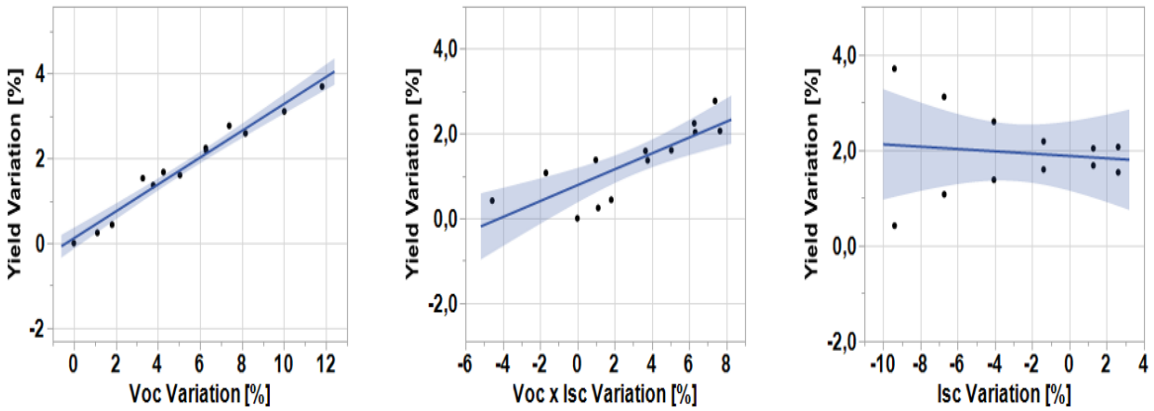

(a) V_{oc} (b) $V_{oc} \times I_{sc}$ (c) I_{sc}

Figure 3.8: Yield variation with respect to the performance parameters at Singapore (albedo : 0.5). The fitted data is arranged in the order of best fit.

The JMP analysis showed that the parameter V_{oc} has the best correlation with the yield. The results of the fit test arranged in order of goodness of fit are shown in the figures 3.8a, 3.8b and 3.8c. So V_{oc} has a better correlation with yield than $V_{oc} \times I_{sc}$. The same trend was seen in other locations such as Los Angeles, Perth, Durban and Chennai which fall under tropical / humid sub tropical climate. (Refer the appendix B for results for other mentioned locations). This can also be attributed to the elevated temperatures at this region. The higher the V_{oc}, the lower the temperature coefficient. For these regions with fairly high temperatures, we can trade off I_{sc} and FF to increase the V_{oc}. So, we can conclude that yield maximizing parameter at tropical equatorial climate is V_{oc}.

3.3.3. Hot desert climate - Doha

Doha, the capital of Qatar is classified as hot desert climate under Köppen climate classification. Hot month average temperature is between $29-35°C$ and mid-day temperature of $43-46°C$ are common. The figures 3.9a and 3.9b shows the insolation distribution at this climate. It can be clearly noted that the concentration of the irradiation conditions are above $700 W/m^2$ and cell temperatures above 30 °C. With the higher albedo of 0.75 we the rear irradiance increases and we can clearly see that in the graph 3.9b.

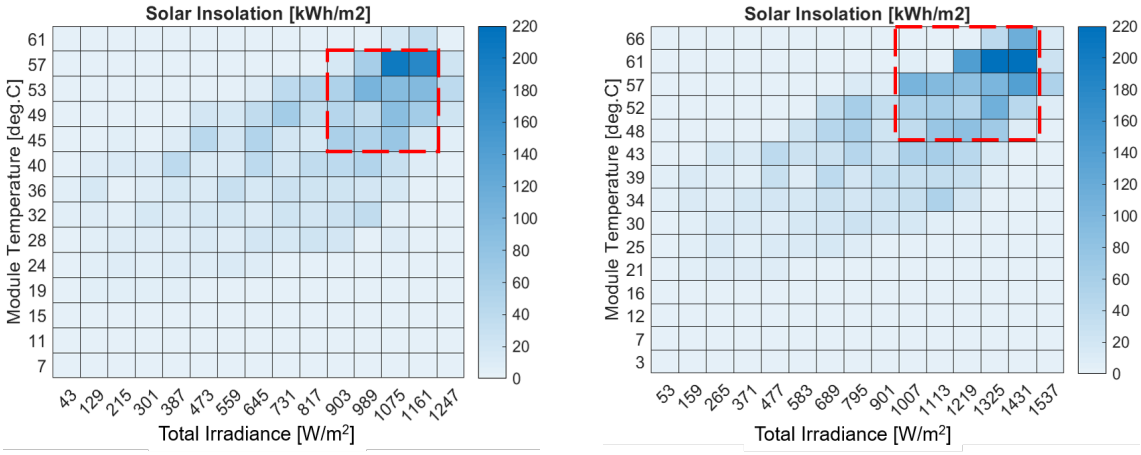

(a) Distribution of annual solar insolation at albedo of 0.25. The region marked by the red lines is the bins of significance with major contribution to the annual solar insolation

(b) Distribution of annual solar insolation at albedo of 0.75. The region marked by the red lines is the bins of significance with major contribution to the annual solar insolation

Figure 3.9: Climate at Doha

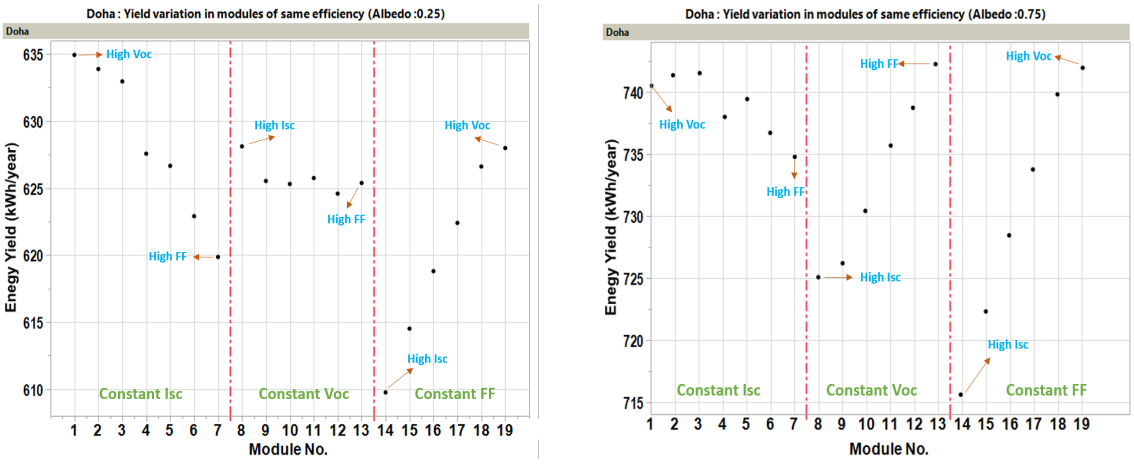

(a) Simulated yield for theoretical modules at albedo of 0.25. The red dotted lines are to indicate the separation between the three sets of modules with constant I_{sc}, constant V_{oc} and constant FF

(b) Simulated yield for theoretical modules at albedo of 0.75. The red dotted lines are to indicate the separation between the three sets of modules with constant I_{sc}, constant V_{oc} and constant FF

Figure 3.10: Yield simulation results for Doha

The figure 3.10a and the figure 3.10b shows the yield simulation at Doha for all the considered modules at albedo of 0.25 and 0.75 respectively. We can notice an yield change variation of about 4% in both the cases. We can clearly notice variation in module performance at different albedos (increased rear irradiation and cell temperature at higher albedo). Considering the modules 8 - 13, with constant V_{oc}, the change in the yield to the variation of I_{sc} and FF are very minimal at albedo of 0.25. But, at albedo of the 0.75 the module with high FF has better yield. This shows the importance of FF at high irradiance and temperature.

The figure 3.11 shows the performance ratio computed using the equation 3.2. The region marked by the red lines in the graph is the region of significance with major contribution to the total annual insolation in

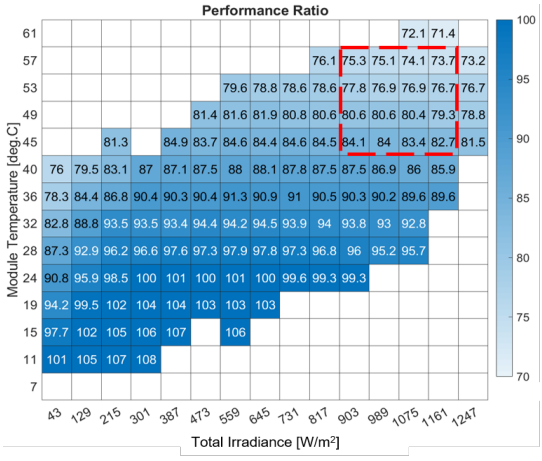

(a) Average performance ratio of module no.8

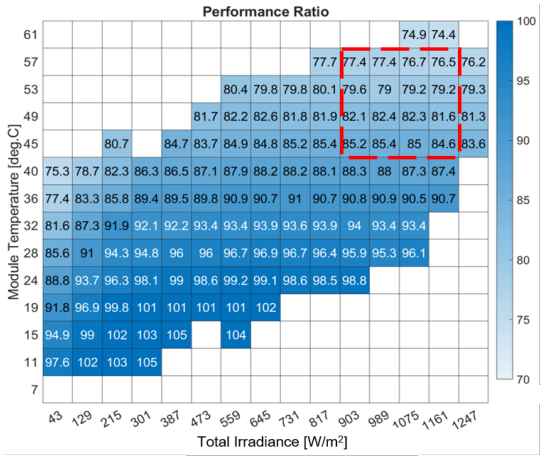

(b) Average performance ratio of module no.1

Figure 3.11: Performance of modules at Doha with ground albedo:0.25

the location. We can see that in the region of significance, the module 1 (highest V_{oc}) has higher performance ratio when compared to module 8 (highest $V_{oc} \times I_{sc}$).

This is similar to the trend noted at Singapore. Comparing the module set 8 to 13 in figures 3.3b, 3.6b, 3.10a and 3.10b we can notice that at constant FF, contribution of I_{sc} to the yield has dropped while the contribution of the FF has increased at Doha. This can be taken as a transition climate above which we need to start focusing on the FF in our design. To substantiate this pattern we can look at the performance of the modules at Doha with ground albedo of 0.75 (High rear irradiance and high cell temperature).

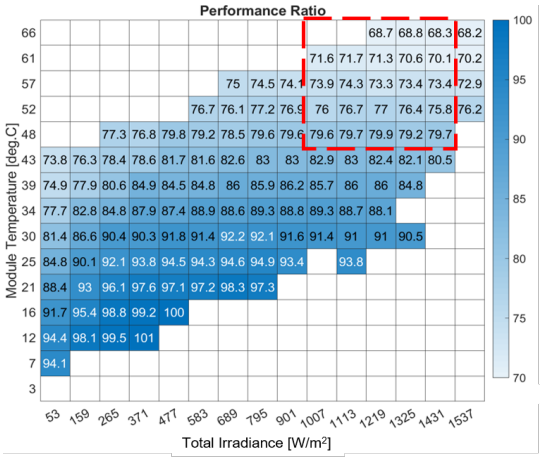

(a) Average performance ratio of module no.1

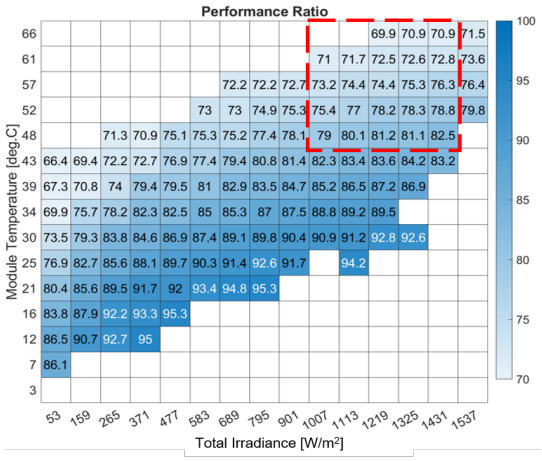

(b) Average performance ratio of module no.13

Figure 3.12: Performance of modules at Doha with ground albedo:0.75

The figure 3.12 shows the performance ratio calculated using the equation 3.2 for modules 1 and 13 at albedo of 0.75.The region marked by the red lines in the graph is the region of significance with major contribution to the total annual insolation in the location. From the figures 3.12a and 3.12b we can observe that in the region of significance, module 13 with higher FF (Also higher $V_{oc} \times FF$ product) have higher performance compared to module no 1 (with high V_{oc}).

The figures 3.13 shows the JMP analysis results at albedo of 0.25. The figures 3.13a, 3.13b, 3.13c shows yield variation with respect to variation in V_{oc}, $V_{oc} \times I_{sc}$ and $V_{oc} \times FF$ respectively at albedo of 0.25. They are arranged in the order of best fit. The yield increase strongly correlates with increase in V_{oc}. We can conclude that V_{oc} is the yield maximizing parameter of Doha at lower albedo of 0.25.

The figures 3.14 shows the JMP analysis results at albedo of 0.75. The module no 1 (High V_{oc}) which was performing best at albedo of 0.25 is being outperformed by the module no 13 (High $V_{oc} \times FF$ product). This is

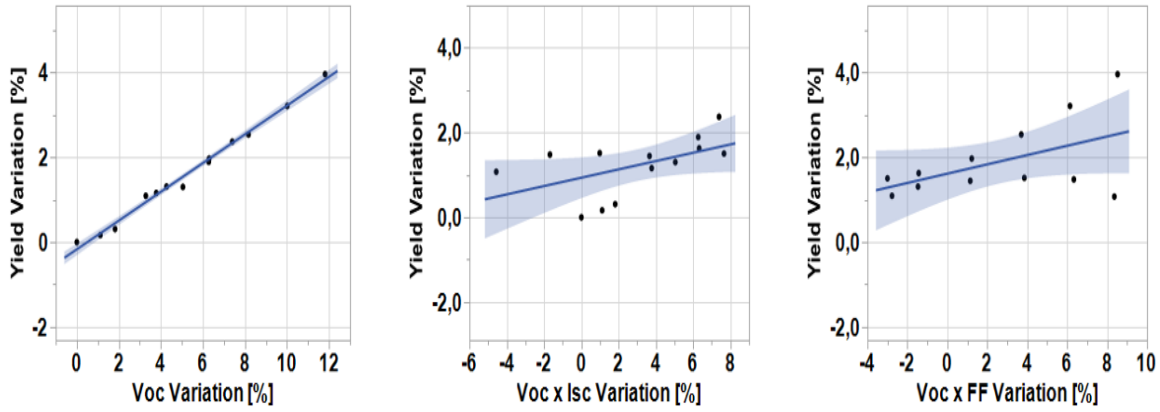

(a) V_{oc} (b) $V_{oc} \times I_{sc}$ (c) $V_{oc} \times FF$

Figure 3.13: Yield variation with respect to the performance parameters at Doha (albedo : 0.25). The fitted data is arranged in the order of best fit.

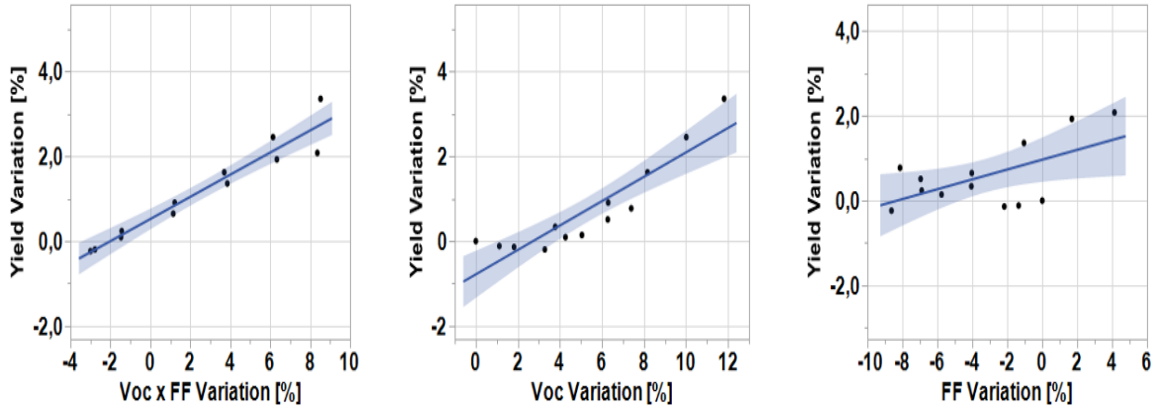

(a) $V_{oc} \times FF$ (b) V_{oc} (c) FF

Figure 3.14: Yield variation with respect to the performance parameters at Doha (albedo :0.75). The fitted data is arranged in the order of best fit.

due to the fact that increased albedo has shifted the average total irradiance to more than $1000 W/m^2$ where module 13 has better performance ratio compared to module 1. The figures 3.14b, 3.14c and 3.14a shows yield variation with respect to variation in V_{oc}, FF and $V_{oc} \times FF$ respectively at albedo of 0.75. They are arranged in the order of best fit. Here we can see that here is no strong correlation as we see in case of albedo of 0.25. As we move from albedo of 0.25 to 0.75 we can see the importance of FF improving. 3.13c and 3.14a projects the same. This can also be attributed to the fact that there will be high currents due to high irradiance and associated, high temperature. Having lower series resistance reduces the current losses and having higher V_{oc} reduces the temperature losses. We can trade off I_{sc} to improve V_{oc} and FF. The same trend was seen in the hot desert climates like Cairo and Port Louis at high albedos. We can conclude that at hot desert climates with high albedos, the product of V_{oc} and FF is the yield maximizing parameter.

3.4. Conclusion

From the above discussion we can conclude that designing cells for the maximal yield at the climate is needed to bring down the LCoE. Summary of all the conclusions from this experiment is given below.

Oceanic and temperate climate : Yield simulations at locations like London, Vancouver and Amsterdam, with relatively low irradiance and moderate temperatures, showed that the yield improved when the product of V_{oc} and I_{sc} increased. This is due to the fact that these regions have relatively low currents due to lower irradiation. The series resistance (Rs) becomes less significant. While designing the cell for these regions, FF can be reduced in favour of higher I_{sc} and V_{oc}.

Tropical, humid and subtropical : Yield simulations at locations like Singapore, Chennai, Los Angeles and Durban, with average irradiance, but fairly high temperatures, showed that the yield determining parameter for these regions is V_{oc}. The higher the V_{oc}, the lower the temperature coefficient. This makes V_{oc} the yield maximizing parameter at this climatic zone.

Hot desert and arid climates : Yield simulations at locations like Doha and Cairo, with high irradiance, high albedo and high temperatures, showed that yield improved when the product of V_{oc} and FF increased. High irradiance and high temperature in these regions requires low series resistance and high V_{oc} to reduce the losses. Thus the product of V_{oc} and FF is the yield maximizing parameter at this climatic zone.

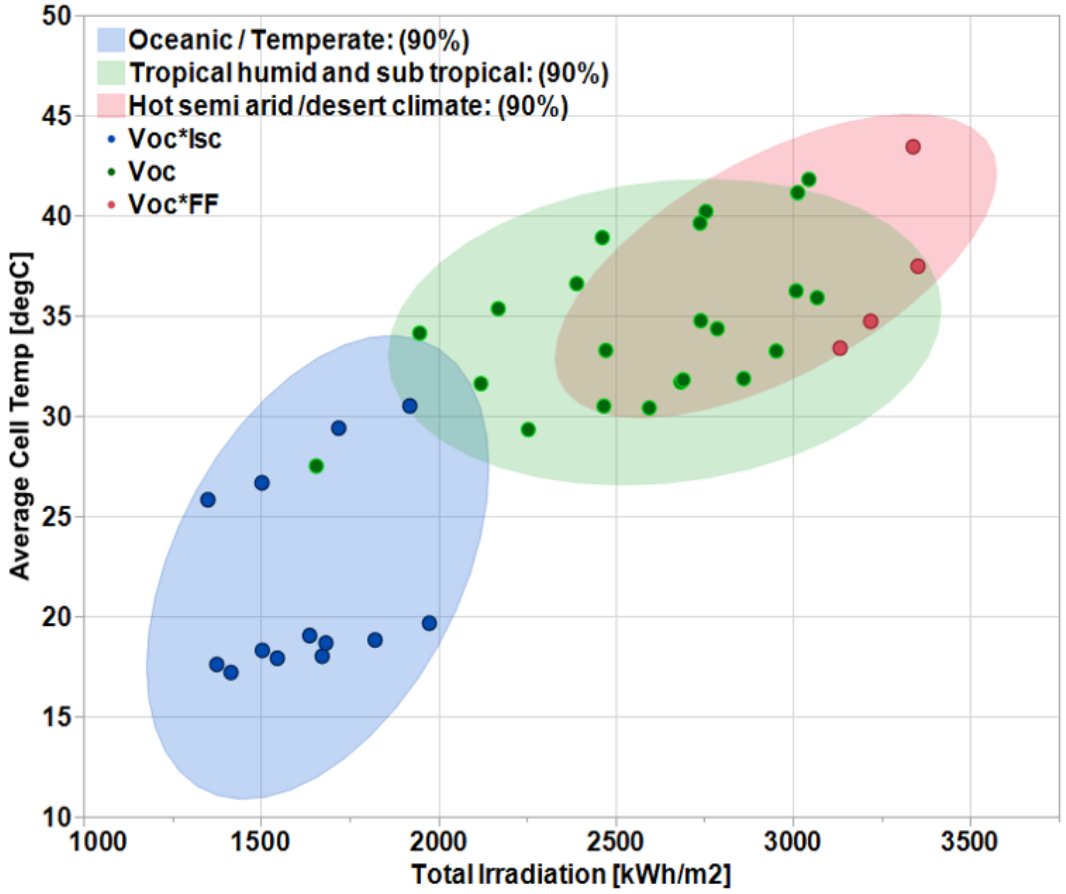

Figure 3.15: Yield maximizing parameter at different climatic zones. Three colored bubble signifies the three climatic zones.

The figure 3.15 gives the summary of the experiment. We can clearly notice the trend in changing yield maximizing parameter from one climatic region to other. Designing cells and modules to suit the climatic conditions using the presented data will increase the yield, thereby reducing the LCoE of solar power.

4

Optimizing the metal pattern for different geographic location

4.1. Introduction

The metal grid is an important non-semiconductor part in the solar cell. Most of the metallization paste used in current c-Si solar cells contains silver as the major constituent[32]. Cost of silver depends on the world market and it fluctuates. Silver is most expensive non-silicon component of a solar cell and it accounts for about 13% of non Si cell costs [32]. Therefore, it is necessary to optimize the metal pattern to reduce the silver usage. The figure 4.1 shows the decreasing trend in silver per cell for a mono-facial cell. Current mono-facial cells use around 100 mg/ cell [32]. It is over 350 mg/cell when we consider a bi-facial cell with more rear metal coverage and thick patterns. Bi-facial cells are expected to gain a market share of 40% by 2028 [32]. Cell technologies like nPERT and n-type PERPoly Bi-facial cells have silver metal patterns on both sides.These cell technologies have additional cost component due to additional silver on the rear side. As the technology finds its place in the market it is also necessary to make it economical and sustainable.

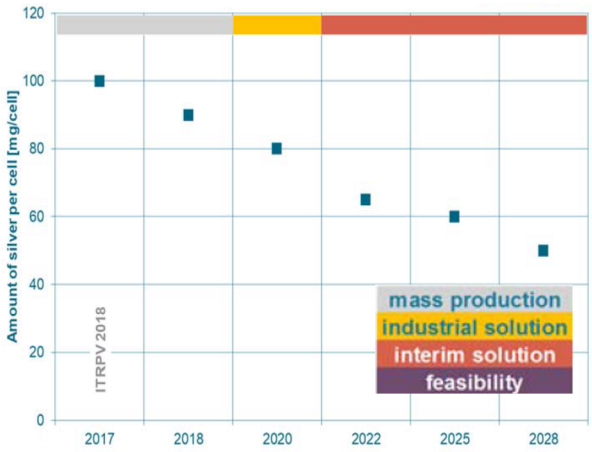

Figure 4.1: Trend for remaining silver per cell (156 X156 mm)[32]

This experiment is targeted on n-type bi-facial cell. The experiment is designed to check the feasibility of three aspects. First is to find whether the IV parameters can be manipulated by varying the metal grid to increase the yield maximizing parameter at different climatic zone. The second is find the amount of silver reduction feasible when we optimize the metal pattern suiting a climatic condition. The third aspect is to address the financial benefit to have different metal patterns for different climatic conditions.

4.2. Test setup

The previous experiment on yield maximizing parameter (Chapter 3) proved that there is a unique performance parameter for every climatic zones. This experiment is aimed to manipulate the performance parameter to achieve higher yield by optimizing the metal pattern. To study, a reference solar cell of TOPCon (also call PERPoly) architecture from ECN part of TNO is chosen for this experiment. This experiment studies the variation yield with different metal patterns. Metal grid pattern parameters such as finger count, finger width, finger height, busbar height are varied in full factorial matrix and its effect on the yield of the solar cell at different climatic zones are studied.

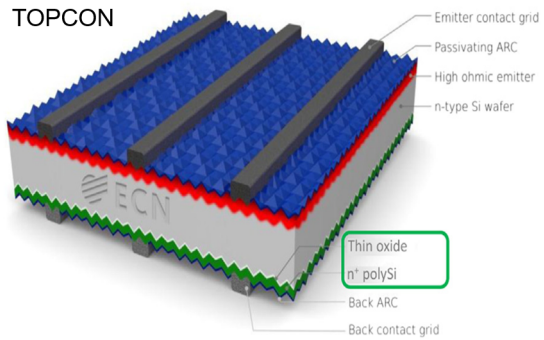

Figure 4.2: TOPCON Architecture, ECN part of TNO

4.2.1. Reference cell and module

The figure 4.2 shows the reference TOPCon cell chosen for this experiment [33]. The cell has n-type Si wafer. It has uniformly diffused emitter at front with sheet resistance of $63 ohm/sq$. Front surface is passivated with Al_2O_3 and coated with $SiN_x : H$. The rear has n^+ poly-silicon layer with sheet resistance of $70 ohm/sq$. The metal grid is screen printed on both front and rear sides with metal coverage of 4.6% and 7.3% respectively. The metal pattern of the reference cell is given in the table 4.1 and it requires 380 mg of silver.

	Busbars			Fingers		
Side	**Number**	**Width (μm)**	**Height (μm)**	**Number**	**Width (μm)**	**Height (μm)**
Front	4	800	20	100	40	20
Rear			15	138	60	15

Table 4.1: Front and rear metal pattern data for the reference TOPCon cell

A 60 cell module with the reference cell mentioned above was theorized. The IV parameters of the reference module is given in the table 4.2.

Isc [A]	**Impp [A]**	**Voc [V]**	**Vmpp [V]**	**FF [%]**	**Module Efficiency [%]**	**Bi-faciality factor [-]**
9.12	8.64	40.8	33.9	78.7	17.8	0.83

Table 4.2: IV parameters of 60 cell module with the reference TOPCon cell

4.2.2. Metal pattern variable matrix

To find the optimum metal pattern, first the front side pattern was swept with values from the table 4.3 with rear pattern same as that of the reference cell. The metal pattern with yield within the top 1% range and less silver content is chosen. Then with chosen front metal pattern, the rear metal pattern is varied with the values from the table 4.3. After rear metal optimization, the pattern with yield within the top 1% range and silver less than that of the reference cell is chosen to be the optimal pattern.

No of busbars (#)	4				
Busbar Width (μm)	800				
Busbar Height (μm)	2	3	5	10	20
Finger Height (μm)	2	3	5	10	20
No of fingers (#)	100	95	90	85	80
		75	70	65	
Finger Width (μm)	25	35	45	55	65

Table 4.3: Metal grid parameter variation matrix

4.2.3. Simulation

Grid characteristics of metal pattern like metal coverage, series resistance, metal content etc are obtained for different metal pattern combinations using the grid calculator from PV lighthouse [34]. Then, the TOPCon cell with different metal pattern is simulated for the IV characteristics using Quokka simulator [35]. The IV parameters are used to obtain the single diode parameters using IVFIT tool [36]. The single diode parameters, a, I_l, I_o, R_s, R_{sh} along with PV system configuration are fed to the BIG EYE bi-facial yield simulator [29]. the table 4.4 shows the PV system considered for simulation. The simulation is carried out for different climatic conditions. One location from each of the climatic classification that was referred in previous experiment (chapter 3) is chosen. The table 4.5 shows the locations selected from each zone. The high albedo values are chosen to study the extreme cases.

Parameter	**Value**
System size	1 module
Orientation	Equator facing - portrait
Elevation	0.5 m
Tilt	Optimized for location
Albedo	0.25, 0.5,0.75

Table 4.4: simulation constraints used for BIG EYE bi-facial yield simulation

Climatic zone	**Location**	**Albedo**
Oceanic/ Temperate	London	0.25
Tropical / Humid sub tropical	Singapore	0.5
Hot semi arid and desert climate	Doha	0.75

Table 4.5: Location with albedo chosen for metal optimization

4.3. Results and Discussion

In this section we discuss the results of the metal grid optimization experiment. First the front metal pattern is varied and the yield for each of the patterns is computed and then the pattern with less silver and similar yield when compared to the reference module is chosen and then the rear metal is varied to see the effect of the yield. Although, the three locations were considered for the optimization, results of London and Doha are only discussed in full extent. The results of the metal optimization for the Singapore are just stated.

4.3.1. Front metal optimization

The front metal pattern is varied with a constant rear metal. Same metal patterns were simulated for all three locations. The figure 4.3 shows the yield simulated for different front metal patterns at London, oceanic climate and Doha, hot desert climate. We can clearly see a trend in the data where the data points accumulate separately for each pattern height. We can clearly notice that in both the cases the yield is higher for pattern with narrow fingers but yield at London exhibits strong correlation with narrowness of the finger than Doha because the increase in I_{sc} due to reduced metal coverage increases yield more in London when compared to Doha. This is can be attributed to the previous result of I_{sc} being the one of the yield maximizing parameter

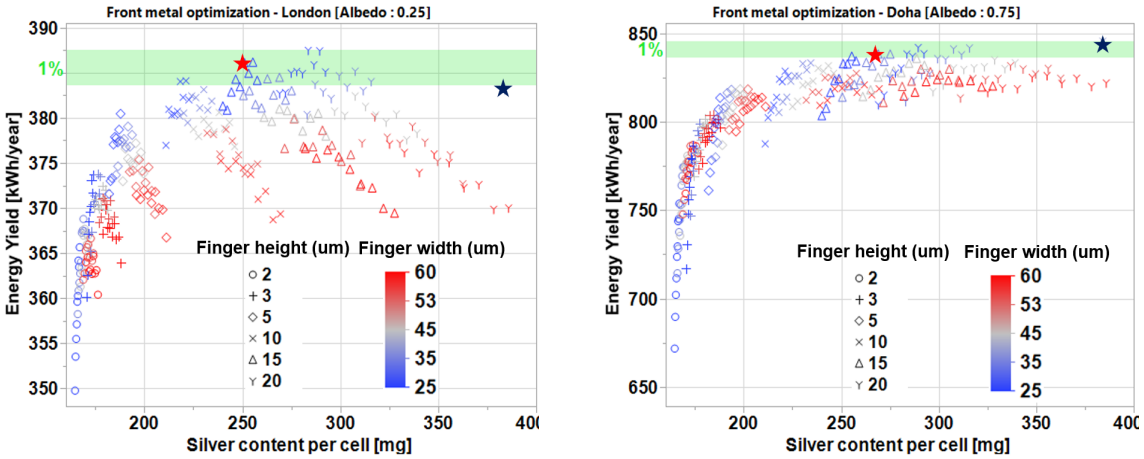

(a) Yield data for different front metal patterns - London[Albedo:0.25]

(b) Yield data for different front metal patterns - Doha [Albedo:0.75]

Figure 4.3: Front metal optimization results for two different climatic zones. The blue star denotes the yield performance of the reference cell. The red star denotes the pattern of the cell chosen as optimized front metal as the yield is within the 1% zone and has lesser silver content.

of Oceanic climate. We can also notice that yield reduces as we reduce the thickness of the fingers. The blue star in the graphs in the fig 4.3 is the performance of the reference cell. In London we can clearly see that patterns with less metal than the reference cell has better yields. but whereas in Doha at high albedo conditions the reference cell has the better performance.

The yield variation noticed in oceanic climate like London is around 40 kWh whereas for hot desert climate like Doha is around 180 kWh. As we move from Oceanic climate to hot desert climate yield sensitivity to metal pattern increases. The green region marked in the graphs shows the metal patterns with yield within maximum 1%. In London we can notice there are are patterns with 10 μm thickness falling in the 1% zone. In Doha we can notice that only certain patterns with 15 and 20 μm thickness fall within the 1% zone. The figure 4.4a shows the comparison of yield change at finger height of 20 μm. The figure 4.4b shows the yield variation to the change in the $V_{oc} \times I_{sc}$ product of the modules. Both the figures looks like mirror images of each other. As the metal content reduces the $V_{oc} \times I_{sc}$ product increases. The graph reveal that the increase in $V_{oc} \times I_{sc}$ product favours yield increase at London (Blue) than at Doha (Red). This is in correlation with the results from the previous chapter 3, Where the yield maximizing parameter for oceanic climate is $V_{oc} \times I_{sc}$ and for Hot desert at high albedo is $V_{oc} \times FF$. So for better yield at hot desert climates, it is advised to focus of FF with more metal coverage.

The figure 4.5 shows the yield change with respect to the finger spacing. Finger spacing can be directly attributed to the number of fingers. Higher the spacing, lower the number of fingers and vice verse. At London for finger widths of 25 μm and 35 μm, yield decreases with increasing the finger spacing. This is largely due to

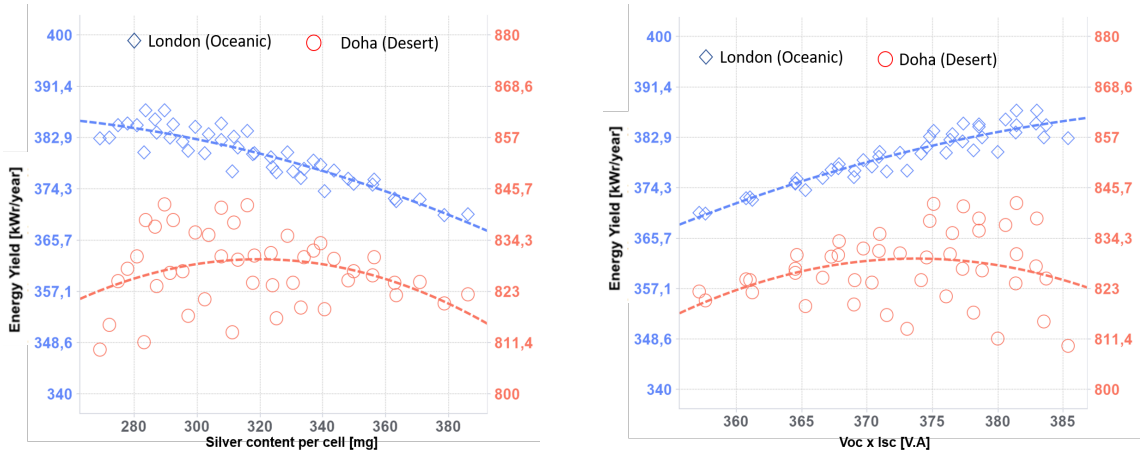

(a) (b)

Figure 4.4: a - Yield variation with respect to the silver content in solar cell for Oceanic and Hot desert climate at the front metal pattern height of 20 μm with varied finger count and width. b - Yield variation with respect to the change $V_{oc}xI_{sc}$ variation at oceanic climate and hot desert climate at the front metal pattern height of 20 μm with varied finger count and width

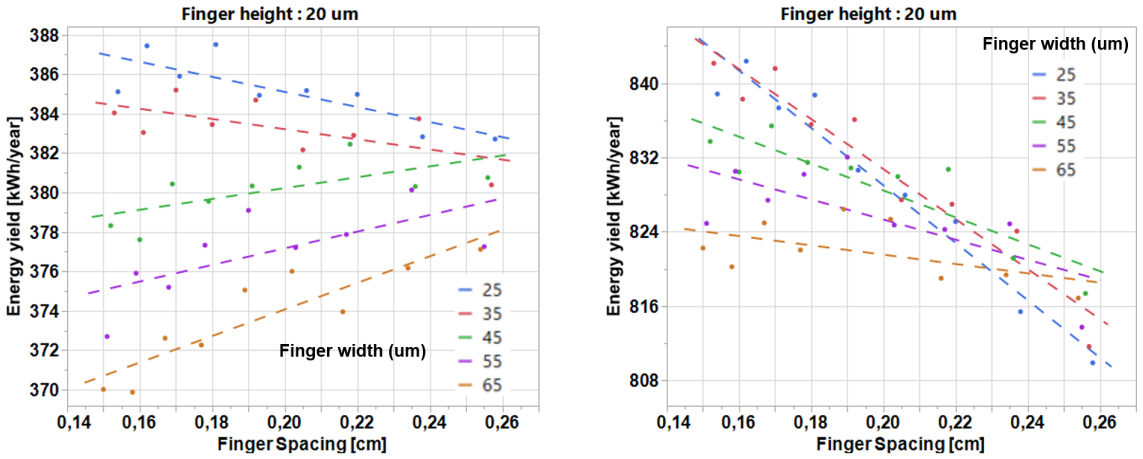

(a) (b)

Figure 4.5: Yield change with finger spacing at finger height of 20 μm for different finger widths. a - London (Oceanic climate) at albedo of 0.25. b - Doha (Desert climate) at albedo of 0.75.

the FF loss dominating the I_{sc} and V_{oc} increase. Whereas for finger widths above 35 μm, the FF loss becomes due to the increased finger spacing becomes less dominant. But in Doha at higher albedo, at all finger widths, Loss in FF at higher finger spacing is not compensated by the Isc and Voc increase. This is because change of yield to change in FF is more significant hot desert climate like Doha. The figure 4.6 shows that sensitivity of the yield towards the FF change is more at hot desert climate like Doha than at London. This correlates with our previous result that yield maximizing parameter at desert climate is $V_{oc} \times FF$.

Optimal front metal pattern is selected from the metal patterns within the 1% region and has less metal when compared to the reference cell. The red star in the graphs shown in fig 4.3 denotes the the metal pattern chosen for the rear metal optimization.

4.3.2. Rear metal optimization

With the front metal pattern chosen from the previous optimization for each of the location, the rear metal is varied with the values from the variable matrix (table 4.3). The figure 4.7 shows the relation between the metal coverage, front side efficiency, bi-faciality and yield at London climate. When we reduce the rear metal coverage the bi-faciality increases and efficiency remains constant for the most range of the metal coverage. We can notice that in the figure (Left) the efficiency does not vary until the metal coverage is below 4%. Both

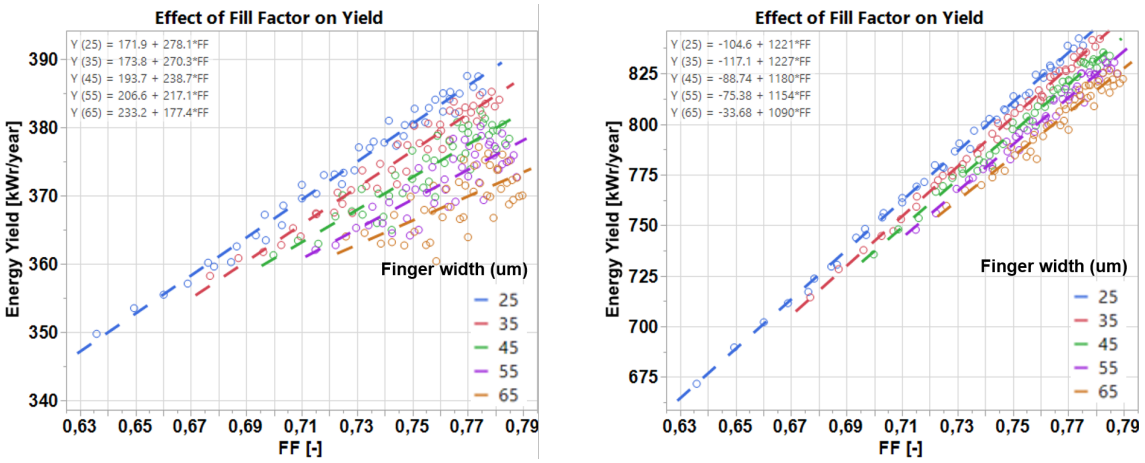

(a) (b)

Figure 4.6: Yield sensitivity to fill factor change at finger height of 20 μm for different finger widths. a - London (Oceanic climate) at albedo of 0.25. b - Doha (Desert climate) at albedo of 0.75.

I_{sc} and V_{oc} are less sensitive to the rear metal coverage, FF reduces drastically for about 20%. Yield loss due to the FF loss was compensated by the increase in bi-faciality. The similar trend was seen in Doha.

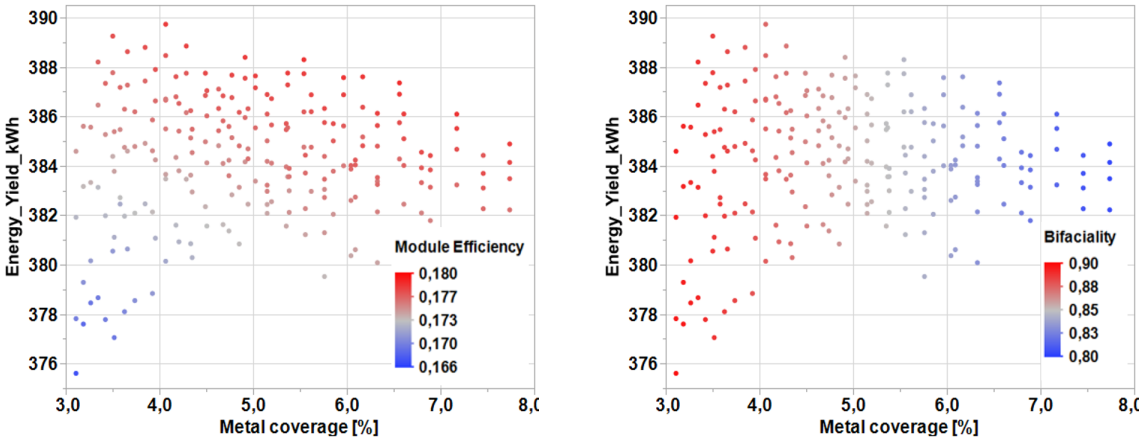

(a) (b)

Figure 4.7: Effect of rear metal coverage, efficiency and bi-faciality on the yield. a - color scale represents the module efficiency. b - color scale represents the bi-faciality factor.

The graph in the figure 4.8a and 4.8b shows the yield for different patterns at London and Doha respectively. The green area marked in the graphs denote the patterns within 1% yield variation from the high yield pattern. There is a similar trend in the yield data as noted in the front metal optimization. The narrow fingers seems to increase the yield at London. Whereas in Doha, relatively wider fingers are needed for better yield. Again as stated before, desert climate like Doha we need to improve the FF to reduce the resistive losses at high current conditions.

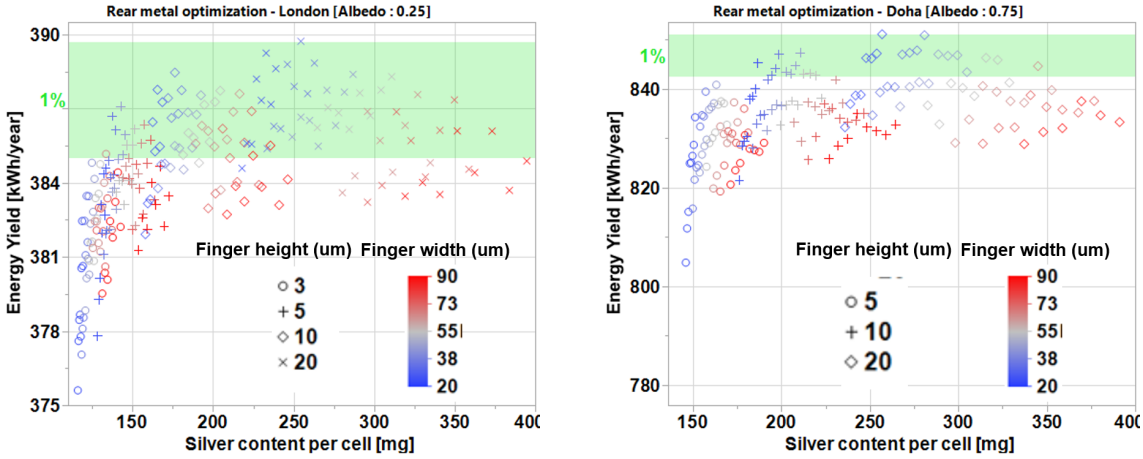

(a) (b)

Figure 4.8: Rear metal optimization results for two different climatic zones.a - London, Oceanic climate , albedo:0.25. b - Doha, Desert climate, albedo:0.75

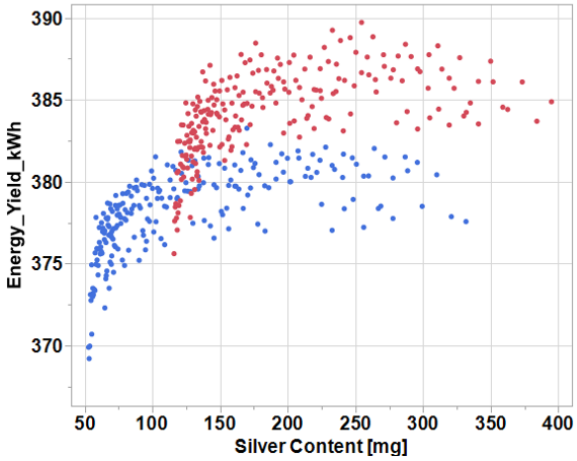

Figure 4.9: Rear metal optimization trend when different front metal pattern is used. The red dots in the graph signifies the rear optimization data cloud when a thick front pattern of 15 μm is used. The blue dots in the graph represents the rear optimization data cloud when thin front pattern of 5 μm is used.

The figure 4.9 shows the different yield trend when the rear metal is optimized with different front metals. The red dots represent the yield trend with front pattern thickness of 15 μm and the blue dots represents the yield trend with the front pattern thickness of 5 μm. Both shows the same trend but at different yield levels. This shows that the front metal is important for improving the yield. With a front metal of good yield, the rear metal can be reduced until the yield loss due to the FF loss is compensated by the increasing bi-faciality factor.

4.3.3. Optimal Pattern

The yield results of all the metal pattern combination that simulated are plotted against the silver content. The figure 4.10a and 4.10b shows the optimization results for London and Doha respectively. Flat bed screen printing technology can print metal patterns as narrow as 27 μm but 18μm thick and the Rotary screen printing can print as thin as 12 μm but 45 μm wide fingers[37]. Assuming the current research progress will reach 10 μm thick and 25 μm wide patterns, we can segregate the simulated patterns as manufacturable patterns and R&D patterns. The blue data points shown in the graphs corresponding to the metal patterns with height of 10 μm and above. The red data points are thinner metal patterns. Feasibility of those patterns are a subject of future research. The blue star denoted in the graph represents the yield data of the reference cell. The red star represents the metal pattern with yield within 1% region and can be manufactured with currently avail-

able (near future) technology. The yellow star represents the thinner pattern with yield within 1% region and needs to be researched.

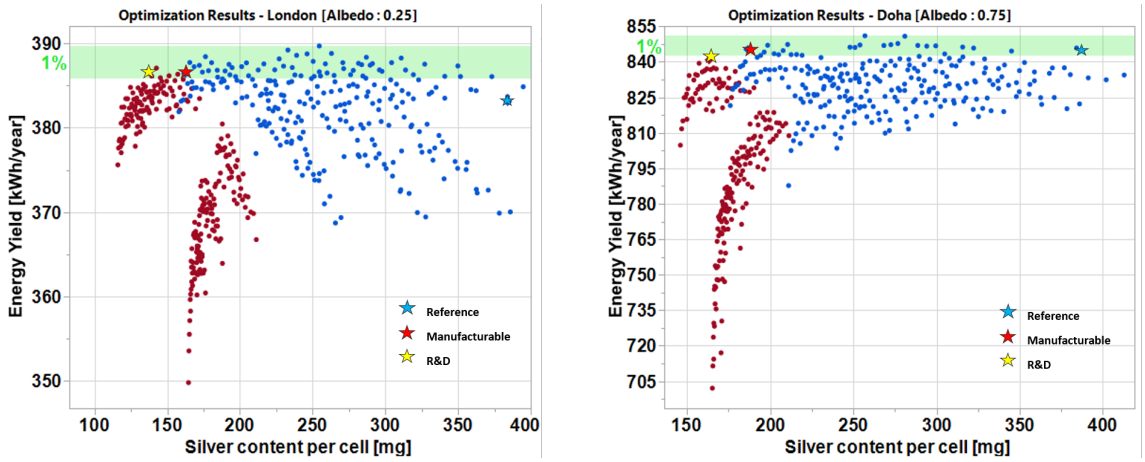

(a) (b)

Figure 4.10: Metal pattern optimization results for two different climatic zones.a - London, Oceanic climate , albedo:0.25. b - Doha, Desert climate, albedo:0.75. Blue dots indicate patterns with height above 5um. Red dots indicate the pattern with thickness of 5 μm. The blue star denotes the reference pattern. The red star denotes the optimal pattern with height above 5 μm. The yellow star denotes the optimal pattern with height 5μm

		Busbars			Fingers			Metal
Location	Side	**Number**	**Width** (μm)	**Height** (μm)	**Number**	**Width** (μm)	**Height** (μm)	**Coverage (%)**
London (Oceanic)	Front	4	800	15	85	25	15	3.42
	Rear			10	80	25	10	3.34
Singapore (Tropical)	Front	4	800	15	85	25	15	3.42
	Rear			10	90	35	10	4.07
Doha (Hot desert)	Front	4	800	15	90	35	15	4.07
	Rear			10	100	35	10	4.29

Table 4.6: Optimal metal pattern for different climatic conditions that can be printed using the current/near future technology.

The table 4.6 give the details of the optimal metal pattern in each climatic zone. It can be clearly noted that metal coverage increases as we move from oceanic climate to the desert climate. Similarly from the table 4.7 we can notice that the $V_{oc} \times I_{sc}$ product is more at oceanic climate than at desert climate and FF increases from oceanic climate to desert climate making the $V_{oc} \times FF$ product high. These results are in correlation with the results of the previous experiment, yield maximizing parameter.

The table 4.8 gives the R & D patterns that will have similar performance. We can notice the trend in the metal coverage as well as in the FF. When we observe the the rear pattern the finger height is reduced contributing to major silver saving while the fingers are made wider to compensate for the FF lost in reducing the height. As the rear pattern is contributing less to I_{sc}, making the cells wider does not affect the it. For Singapore and Doha, the thinner finger will lose the more yield.

Location	Isc [A]	Impp [A]	Voc [V]	Vmpp [V]	FF [%]	Module Efficiency [%]	Bi-faciality factor [-]	Yield Change [%]	Silver Saved [%]
London (Oceanic)	9.34	8.8	41.1	32.8	75.1	17.5	0.89	0.87	58
Singapore (Tropical)	9.34	8.8	41.1	33.1	75.8	17.7	0.87	0.2	54
Doha (Desert)	9.22	8.7	40.9	33.4	77.1	17.7	0.88	0.1	48

Table 4.7: IV parameters of optimal patterns for different climatic conditions that can be printed using the current/ near future technology

		Busbars			Fingers			Metal Coverage (%)
Location	**Side**	**Number**	**Width (μm)**	**Height (μm)**	**Number**	**Width (μm)**	**Height (μm)**	
London (Oceanic)	Front	4	800	15	85	25	15	3.42
	Rear			5	90	35	5	4.07
Singapore (Tropical)	Front	4	800	15	85	25	15	3.42
	Rear			5	90	45	5	4.63
Doha* (Hot desert)	Front	4	800	15	90	35	15	4.07
	Rear			5	100	45	5	4.91

Table 4.8: Optimal metal pattern (R&D) for different climatic conditions. Doha* - there were no thinner pattern that was within the 1% yield range. So the next best cell with thinner pattern is chosen.

Location	Isc [A]	Impp [A]	Voc [V]	Vmpp [V]	FF [%]	Module Efficiency [%]	Bi-faciality factor [-]	Yield Change [%]	Silver Saved [%]
London (Oceanic)	‘9.34	8.8	41.1	32.8	75.2	17.6	0.88	0.93	64
Singapore (Tropical)	9.34	8.8	41.1	32.9	75.6	17.6	0.86	-0.16	62
Doha (Desert)	9.22	8.7	40.9	33.3	76.8	17.6	0.87	-0.5	57

Table 4.9: IV parameters of optimal patterns (R&D) for different climatic conditions

4.4. Conclusion

The results of the above experiment conclude that the metal patterns can be manipulated to increase the yield maximizing parameter at a climatic zone. The cell with optimal metal pattern for oceanic climate had high $V_{oc} \times I_{sc}$ product and cell with optimal metal pattern for desert climate had high $V_{oc} \times FF$ product. This successfully answers the first aspect of this experiment.

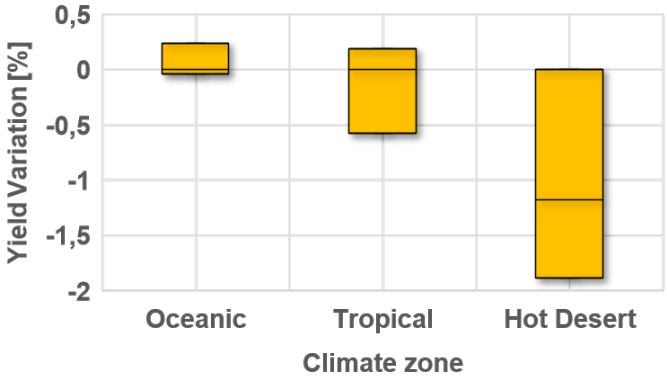

Figure 4.11: Yield variation when the optimal patterns for each climate zone is simulated for yield performance at other two climate zones.

To see if the there is a need for separate metal patterns for each of the climatic zones. The optimal metal optimal patterns for each climatic zone from the table 4.6 is simulated for the performance at other two climates. The figure 4.11 shows the yield variation due to the using a module with optimal pattern of different climate. At oceanic climate, the variation is minimal because the insolation is distributed almost equally over a wide irradiance range (refer 3.3a) and using the module optimal at any region of irradiance will not lead to a huge variation. On the other hand at hot desert climate, the yield reduction is over 2% because the insolation is accumulated over a small range of high irradiance (refer 3.9b) and using the module optimal at other irradiance regions will lead to more yield reduction. We can optimize the metal for desert climate and use it for all the other climatic zones but we might lose some of the calculated metal savings in oceanic and tropical climate conditions.

	Reference Module	**Module with 50% less silver**
Silver per cell [mg]	380	190
Cost of the metallization paste [$/kg]	650	
Metallization paste cost for 60 cell module [$]	14.8	7.4
Module cost* [$]	136	129
Module cost reduction [%]		5.4

Table 4.10: Cost analysis for 50% silver saving.* Module price is taken from NREL as 0.47$/$W_p$ (2018) and it is assumed as the price of the reference module including the metallization cost.

when optimizing the metal patterns for the yield rather than efficiency, over 50% of the silver can be saved at all climatic conditions. The cost of the industrial Ag metallization paste is around 650 $/$kg$. A 290 W_p module costs 136 $ at rate of 0.47 $/$W_p$ (2018) [38]. Assuming that as baseline price for the reference module with a cell with 380 mg silver, Ag paste cost for the reference module is 14.8$. With half of the metal reduced the silver paste cost per module is 7.4$. So the module cost drops 5.4% to 129$.

To understand the impact on LCoE of the system, NREL's comparative LCoE calculator was used [39]. With the reduction of the module cost from 0.47 $/$W_p$ to 0.44 $/$W_p$, increase in the yield of 1% for the London climate, there was reduction in LCoE by 4.5%.

5

Optimizing the metal pattern for different system configurations

5.1. Introduction

In the previous chapter the metal grid was optimized for a different climatic condition with a underlying constraint that the system configuration is an equator facing system. Bi-facial modules opens a path to new system configuration of vertical systems. The contribution of the rear side irradiation in equator facing system is very less compared to the front side, whereas in vertical systems the contribution to the yield is equal from both sides. This gives the motivation to find the optimal pattern for the vertical system and analyze how different it would be from equator facing systems and east-west titled systems.

5.2. Test setup

This experiment was designed to find the optimal metal pattern for equator facing system, east-west tilted system, east-west vertical systems at particular climatic condition. Amsterdam with oceanic climate was chosen for this experiment. In a same climatic condition the module placed in a different configurations are subjected to different levels of irradiation. Below subsections explain the system configurations, the irradiation profile incident on each of the configuration and simulation constraints used. These configurations were selected as they are part of test fields that are being build in frame work of the HER project POLARIS, currently carried out by ECN.TNO and partners.

5.2.1. Equator facing system

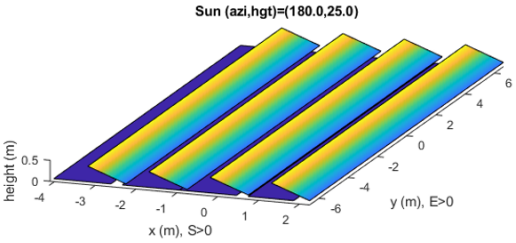

Figure 5.1: Schematic representation of equator facing system used for yield simulation

Parameter	Value	Units
Elevation	0.1	m
Axis tilt	20	deg
Orientation	Landscape	-
Albedo	0.55	-
No of Rows	4	#
Modules per row	8	#
Rows considered for analysis	2,3	#

Table 5.1: System parameters used for yield simulation

The equator facing system is a traditional PV system configuration that has been used for decades. The system used for this experiment has 32 PV modules arranged in 4 rows with 8 modules in each row. The modules are elevated 10 cm from the ground, with axis tilt of 20°. The ground albedo used is 0.55. The system is depicted in the figure 5.1. Although the entire system is used to calculate the irradiance profile incident on each of

the module, the yield is simulated only for the two middle rows as they capture the shading effect and gives conservative value for the yield of the system. This is done just to reduce the simulation time.

5.2.2. East - West Tilted system

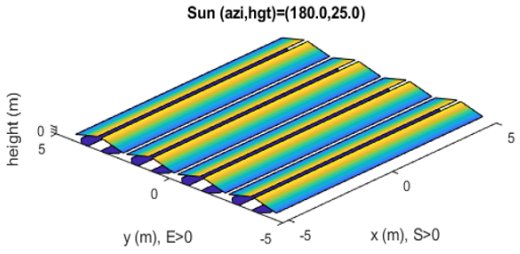

Figure 5.2: Schematic representation of east-west tilted system used for yield simulation

Parameter	Value	Units
Elevation	0.05	m
Axis tilt	12	deg
Orientation	Landscape	-
Albedo	0.55	-
No of Rows	8	#
Modules per row	6	#
Rows considered for analysis	3,4	#

Table 5.2: System parameters used for yield simulation

The East-West tilted systems are optimal for roof top applications with small area. the system has alternative rows with east and west facing modules. The system has 48 modules arranged in 8 rows with 6 modules each. The modules are elevated by 5cm and axis tilted at 12°. The system has aground albedo of 0.55. The figure 5.2 depicts the system to be simulated for yield. Similar to the previous system, for reducing the simulation time the only row 3 and 4 were simulated for yield.

5.2.3. East - West Vertical system

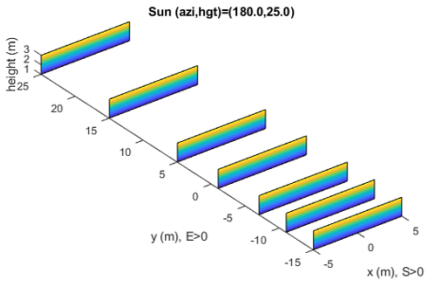

Figure 5.3: Schematic representation of east-west vertical system used for yield simulation

Parameter	Value	Units
Elevation	1	m
Axis tilt	90	deg
Orientation	Landscape	-
Albedo	0.3	-
No of Rows	7	#
Modules per row	12	#
Rows considered for analysis	6	#

Table 5.3: System parameters used for yield simulation

The east-west vertical systems are unique and specific for bi-facial modules. The system has 84 modules arranged in 7 rows. Each row has 12 modules arranged in a matrix of 2 rows and 6 columns. The modules are elevated at a height of 1m. The ground has an albedo of 0.3. The figure 5.3 shows the rows are arranged at different spacing between them to analyze the effect of shadowing for each each rows. For this experiment the yield was simulated for row 6 which has the maximum spacing.

5.2.4. Irradiation analysis

The yield simulation was run for Amsterdam. When analyzed each of the system has was exposed to a different irradiation profile through out the day. The figure 5.4 shows the irradiation profile on $30^{th} June$, incident on the modules in different system configuration. In the figure 5.4a we can see the front in-plane irradiation of different system configuration. Equator facing system (Purple) incidents the maximum front irradiation. In the east-west tilted system, east facing (blue) and west facing (red) module incidents similar levels of irradiation but less than that of the equator facing system. The east-west vertical system (green) incidents least irradiation of all of the other configurations.

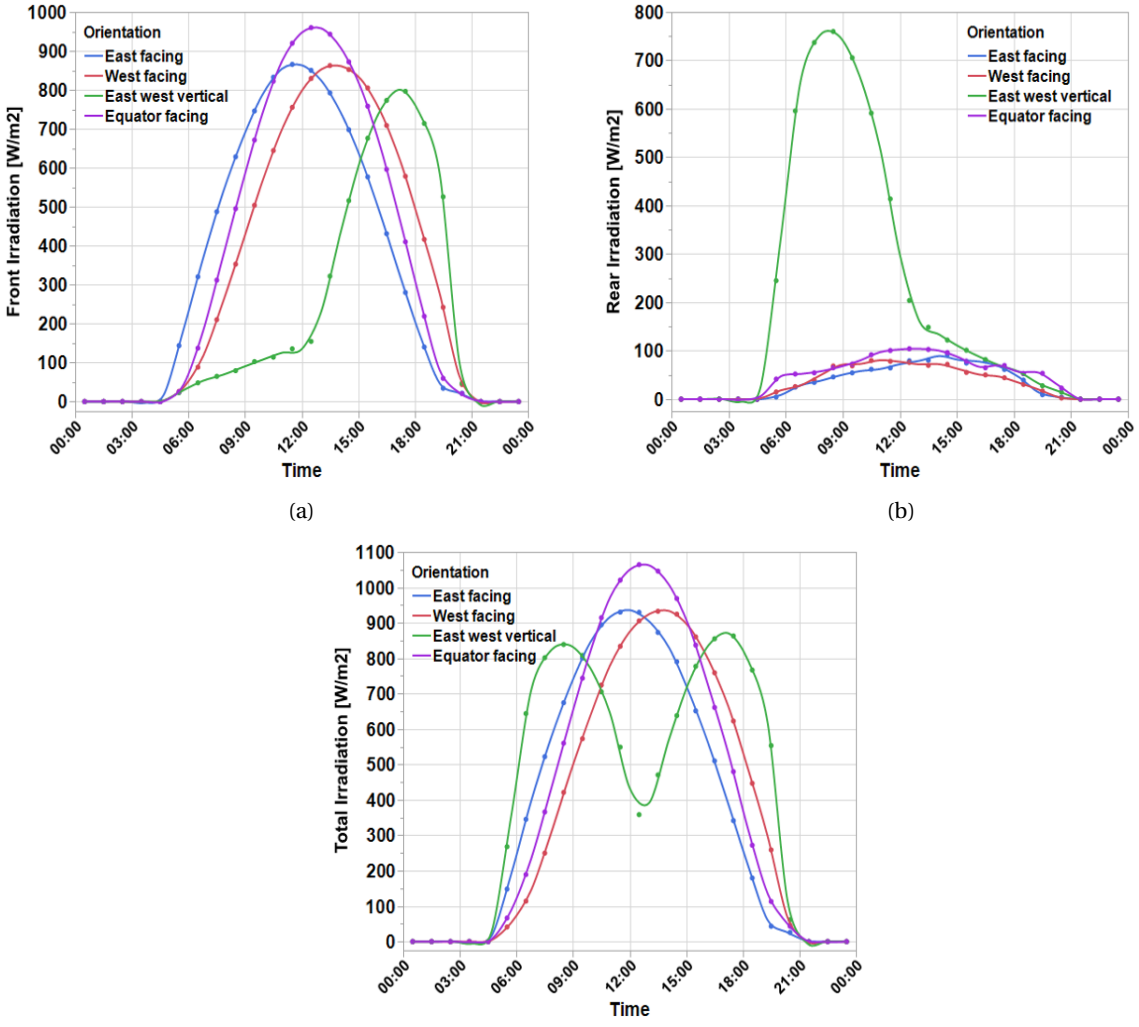

Figure 5.4: Irradiation profile on $30^{th} June$ incident on the module. a - front irradiance profile. b - rear irradiance profile. c - total irradiance

The figure 5.4b shows the rear irradiation. As discussed previously the rear irradiation is decided by the albedo, elevation, cell transparency etc. The rear irradiation of the east west tilted system and equator facing system are less and similar. The vertical system incidents irradiation equal to that of the front side. The figure 5.4c shows the total irradiation. All the systems have different irradiation intensity and distribution. It gives the motivation to find the optimal metal pattern at these configurations.

5.2.5. Reference cell

The cell taken as a reference for this experiment is the TOPCon cell similar to the one used in the previous experiment(4.2.1). The cell has n-type bulk with resistivity of 2.7 ohm.cm, emitter sheet resistance of 85

Side	No of Busbars [#]	Busbar width [μm]	Busbar height [μm]	No of Fingers [#]	Finger width [μm]	Finger height [μm]	Metal Coverage [%]
Front	5	700	20	100	40	20	4.74
Rear			15	138	60	15	7.40

Table 5.4: Metal grid patter of the reference cell

	Isc [A]	Impp [A]	Voc [V]	Vmpp [V]	FF [%]	Pmpp [W]	Module efficiency [%]	Bi-faciality [-]
Ref	9.9	9.33	40.73	33.62	77.8	313.87	19.1	0.82

Table 5.5: IV parameters of the reference cell

ohm.sq and BSF sheet resistance of 70 ohm.sq. This cell has a different metal pattern than the cell used in previous experiment. The table 5.4 shows the metal pattern currently implemented in the cell. The metal pattern is 5 busbar pattern which uses 400 mg of silver. The table 5.5 shows the IV parameters of the reference cell with metal pattern shown in the table 5.4.

5.2.6. Metal pattern variable matrix

To find the optimum metal pattern, first the front side pattern was swept with values from the table 5.6 with rear pattern same as that of the reference cell. The metal pattern with yield within the top 1% range and less silver content is chosen. Then with chosen front metal pattern, the rear metal pattern is varied with the values from the table 5.6. After rear metal optimization, the pattern with yield within the top 1% range and silver less than that of the reference cell is chosen to be the optimal pattern.

No of busbars [#]	5			
Busbar width [um]	700			
Busbar height [um]	5	10	15	20
Finger height [um]	5	10	15	20
No of Finger [#]	60	70	80	90
	100	120	130	140
Finger width [um]	25	35	40	45
		50	60	

Table 5.6: Metal grid parameter variation matrix

5.3. Results and discussion

This section details the results of the metal pattern optimization experiment and discusses the results. The results for each of the system configuration is discussed in subsections below.

5.3.1. Equator facing system

The system contains the 4 rows with 8 modules each. As stated before, the simulation results discussed here are for the two middle rows.

Front metal optimization

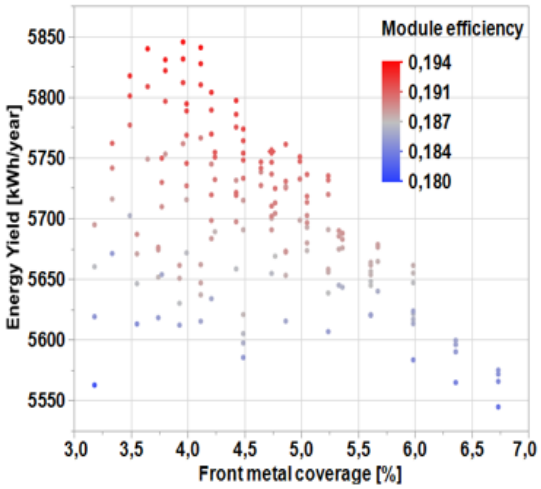

(a) Effect of front metal coverage on front efficiency and energy yield

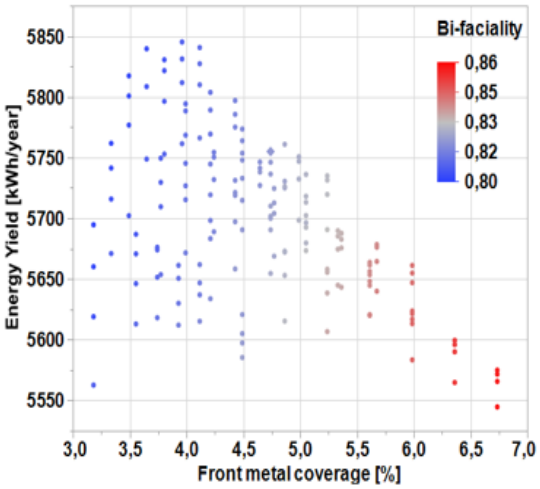

(b) Effect of front metal coverage on bi-faciality and energy yield

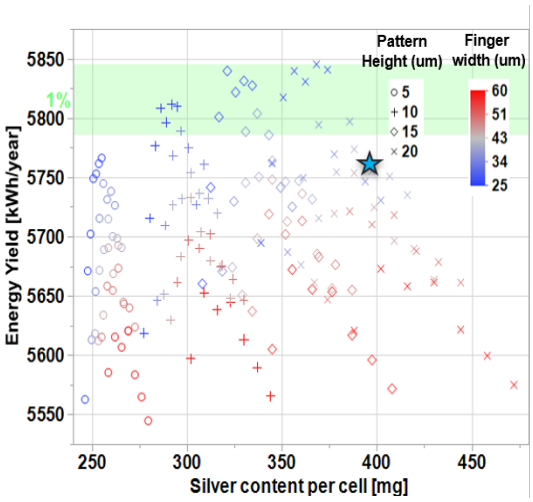

(c) Energy yield of the cells with different front metal patterns plotted against their silver content. The green region denotes the metal patterns within the max 1% yield range.

Figure 5.5: Results - Front metal optimization of equator facing system configuration

First the front metal pattern is varied with the values from the variable matrix table [5.6]. The rear metal patter is kept the same as that of the reference cell shown in the table 5.4. The figure 5.5 shows the results of yield simulation for the front metal optimization. At a pattern height of 20 um, reducing the metal coverage by 45% I_{sc} increases by 6.2%, V_{oc} increases by 1.4%, FF reduces by 2.8%, efficiency increases relatively by 4.65 %, bi-faciality reduces by 6.3% With the all the above changes yield improves by 4.7%. The above statistics helps us understand the front metal optimization.

In the figures 5.5a and 5.5b we can notice the relation between metal coverage, front side efficiency and bi-faciality factor. As the metal coverage decreases, front efficiency increases and bi-faciality decreases (because rear metal is kept constant at this point). we can notice the critical front metal coverage of 4% with high efficiency and low bi-faciality factor, after which the yield starts to falls. The figure 5.5c shows the yield simulation results plotted against the silver content in a cell. The green region marked in the graph represents the metal patterns with maximum 1% yield. The blue star represents the yield performance of the reference cell. we can notice that there are thinner and narrower metal patterns that gives better yield and has less silver than the reference cell. Among the patterns in the green region, a pattern with 15 um thickness was chosen for the rear metal optimization.

Rear metal optimization

With the chosen front metal pattern the rear metal is optimized. The rear metal pattern changed with the values from the variable matrix. when the rear metal was varied, at 15 μm pattern height, for metal reduction of 50%, I_{sc} does not vary, V_{oc} increases by 0.53% FF reduces by 2.3%, efficiency reduces by 1.8% and bi-faciality increases by 8%. This leads to a yield decrease of 1%. The figures 5.6a and 5.6b shows the relationship be-

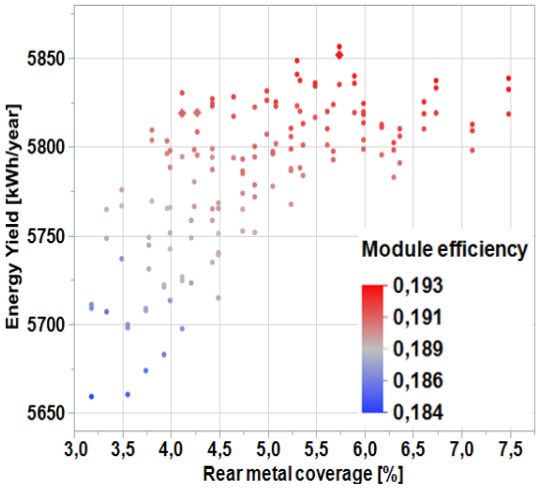

(a) Effect of rear metal coverage on front side efficiency and energy yield

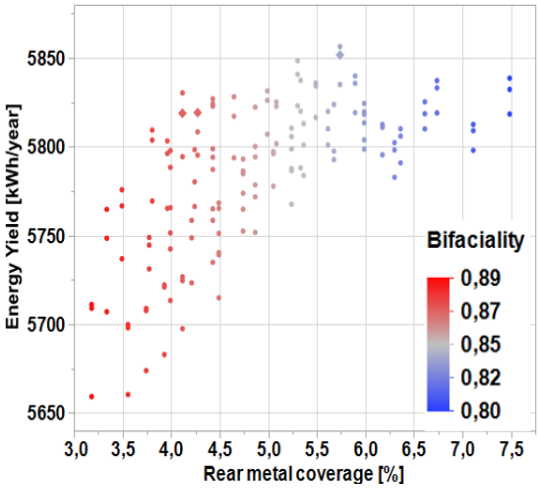

(b) Effect of rear metal coverage on bi-faciality and energy yield

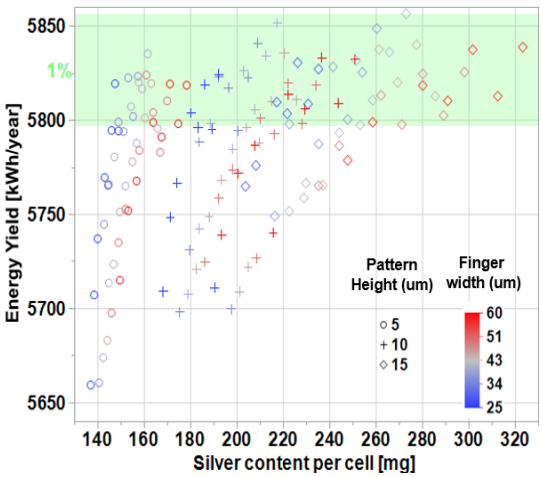

(c) Energy yield of the cells with different rear metal patterns plotted against their silver content. The green region denotes the metal patterns within the max 1% yield range.

Figure 5.6: Results - Rear metal optimization of equator facing system configuration

tween metal coverage, front side efficiency and bi-faciality factor. We notice that bi-faciality factor increases

with reduction in metal coverage and front side efficiency is remains almost unaffected for large range of reduction in the rear metal coverage. This helps to maintain the yield while removing a large portion of the metal. The figure 5.6c shows the yield simulated plotted against the silver content of the cell. the green region shows the metal patterns with max 1% yield. There are thinner and narrower patterns within the green region which has silver content as less 140 mg per cell.

Optimal pattern

The figure 5.7 shows the the metal optimization experiment with equator facing systems. The green region represents the patterns with max 1% yield. The blue star represents the yield performance of the reference cell. The current solar cell metal grid printing industry can print patterns above the height of 5 μm [ref]. Anything below that height is a R&D work.

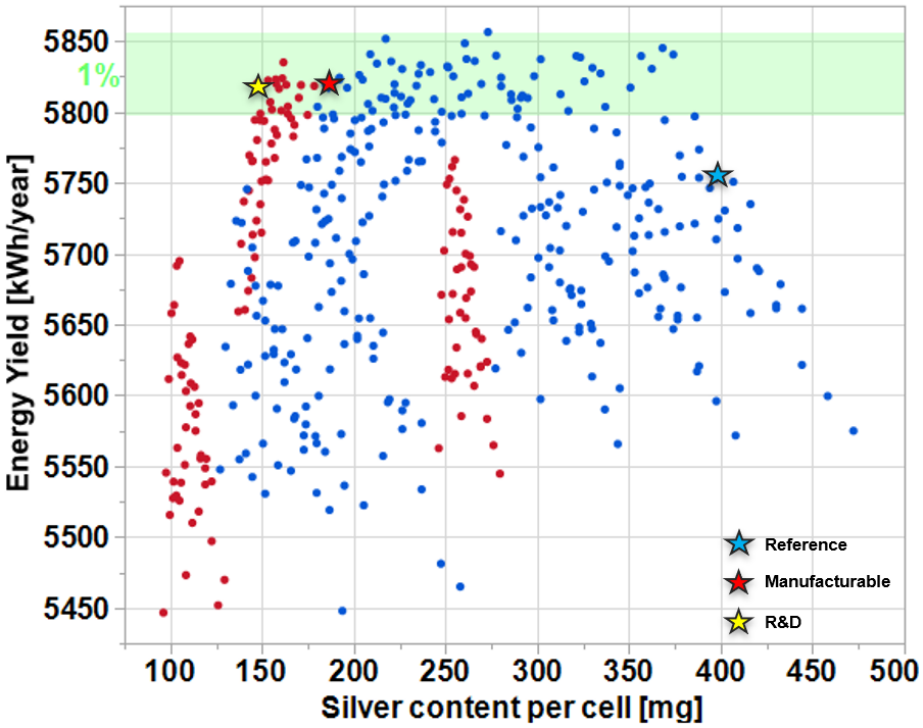

Figure 5.7: Metal optimization results of the equator facing system. Blue dots indicate patterns with height above 5 μm. Red dots indicate the pattern with thickness of 5 μm. The blue star denotes the reference patter. The red star denotes the optimal pattern with height above 5 μm. The yellow star denotes the optimal pattern with height 5 μm

To differentiate it, R&D patterns are denoted by red color dots while the manufacturable patterns are denoted by blue color dots. The red star denote the manufacturable pattern with less silver content and the yellow star represents the thinner R&D pattern with yield within the max 1%.

Side	No of Busbars [#]	Busbar width [μm]	Busbar height [μm]	No of Fingers [#]	Finger width [μm]	Finger height [μm]	Metal Coverage [%]	Yield change [%]	Silver saved [%]
Front	5	700	15	90	25	15	3.63	1.1	53.2
Rear			10	120	25	10	4.11		
Front	5	700	15	90	25	15	3.64	1.1	62.9
Rear			5	130	25	5	4.27		

Table 5.7: Optimal patterns for the equator facing system.

The first metal pattern in the table 5.7 is the chosen manufacturable pattern (Red star). It has 1.1% more yield than the reference cell and 53.2% less silver than that of the reference cell. The second pattern is the R&D pattern (Yellow star) which has thinner rear pattern. The loss in FF of the thinner pattern was compensated

by slightly more coverage. The R&D pattern has 1.1% yield increase and 62.9% silver reduction than that of the reference cell.

	Isc [A]	**Impp [A]**	**Voc [V]**	**Vmpp [V]**	**FF [%]**	**Pmpp [W]**	**Module efficiency [%]**	**Bi-faciality [-]**
Manufacturable	10.11	9.47	41.17	32.98	75.04	312.24	19.0	0.86
R & D	10.01	9.4	41.07	32.94	75.24	309.67	18.82	0.87

Table 5.8: IV parameters of the cells with optimal metal patterns

The table 5.8 shows the IV parameters of the optimized cells. when we compare it with the IV parameters of the reference cell we can notice that I_{sc} and V_{oc} has increased and FF has reduced. This can be correlated to the results of the yield maximizing parameter where at oceanic climatic conditions V_{oc} and I_{sc} must be increased while decreasing the FF to improve the yield. R&D pattern has slightly lesser front - side efficiency which is compensated by the bi-faciality factor.

5.3.2. East - West tilted system

The system consists of alternative rows with East and West facing modules. Total of 48 modules arranged in 8 rows. The simulation results discussed below are for 12 modules of row 3 and 4.

Front metal optimization

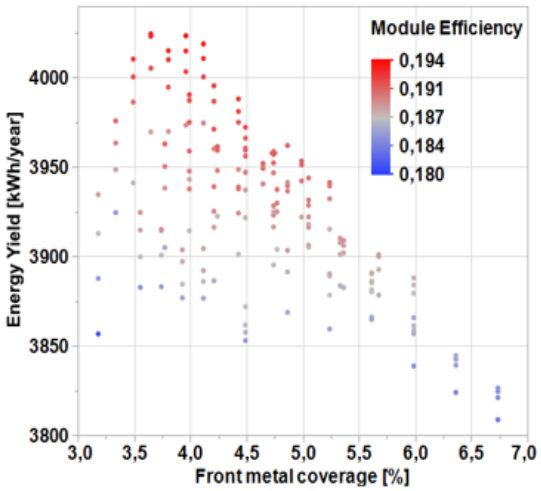

(a) Effect of front metal coverage on front efficiency and energy yield

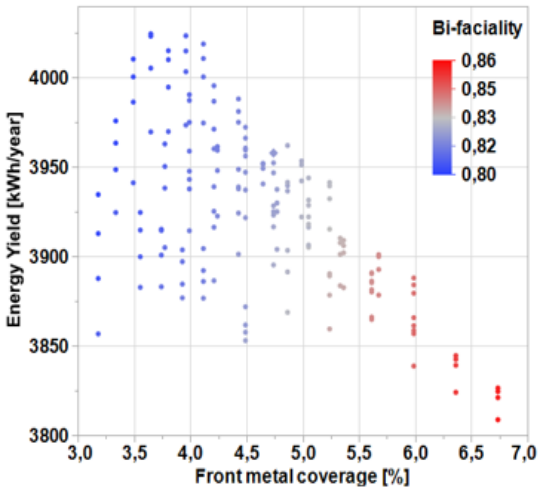

(b) Effect of front metal coverage on bi-faciality and energy yield

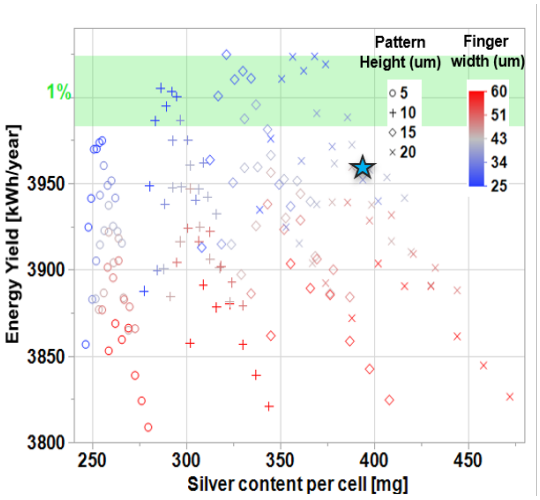

(c) Energy yield of the cells with different front metal patterns plotted against their silver content. The green region denotes the metal patterns within the max 1% yield range.

Figure 5.8: Results - Front metal optimization of East-West tilted system configuration

Front metal pattern is varied with constant rear metal. The metal pattern is varied with values from the variable matrix table 5.6. With constant rear pattern, at pattern height of 20μm when the front metal metal coverage was reduced by 45%, I_{sc} increases by 6.2%, V_{oc} increases by 1.4%, FF reduces by 2.8%, efficiency increases relatively by 4.65 %, bi-faciality reduces by 6.3% With the all the above changes yield improves by 5.4%. The above statistics helps us understand the consequence of front metal optimization. The number looks similar to that discussed in the front metal optimization of the equator facing system. The figure 5.8a and 5.8b shows the relation between energy yield, front side efficiency and bi-faciality factor. The trend seen is similar to that of noticed in the results of the equator facing configuration. Reducing front metal coverage increases the efficiency and thereby the energy yield. The figure 5.8c plots the simulated energy yield of the cells with different metal pattern against their silver content. The data points in the green region denotes

the patterns that have max 1% energy yield. the blue star represents the yield performance of the reference cell. We can notice that there are patterns with less silver and more yield than that of the reference cell. The optimal front pattern is chosen to be the one with 15 μm pattern height.

Rear metal optimization

The rear metal is optimized with chosen front metal pattern. when the rear metal was varied, at 15 μm pattern height, for metal reduction of 55%, I_{sc} does not vary, V_{oc} increases by 0.27% FF reduces by 2.4%, efficiency reduces by 2.3% and bi-faciality increases by 10%. This leads to a yield decrease of 1.3%. These statistics are also similar to the rear metal optimization of equator facing systems.

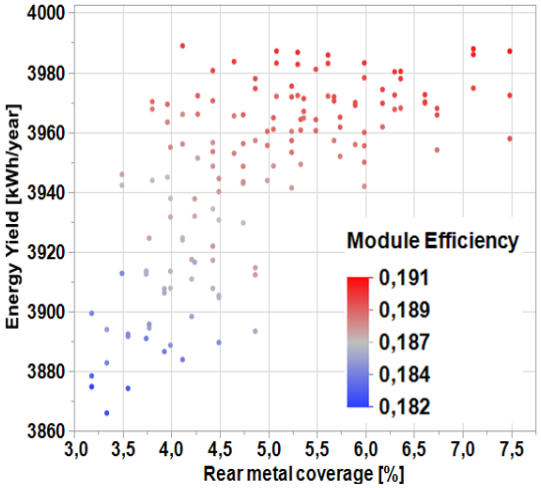

(a) Effect of rear metal coverage on front efficiency and energy yield

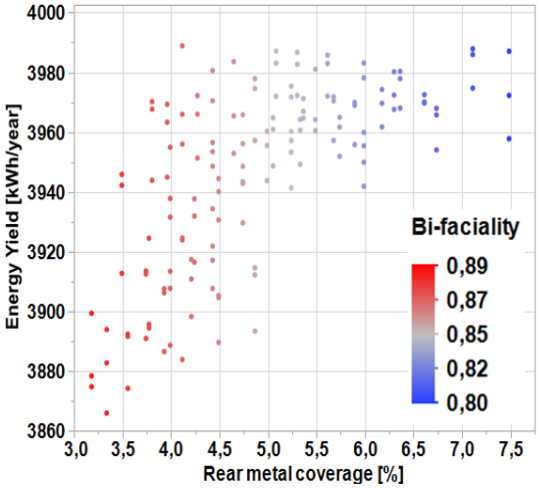

(b) Effect of rear metal coverage on bi-faciality and energy yield

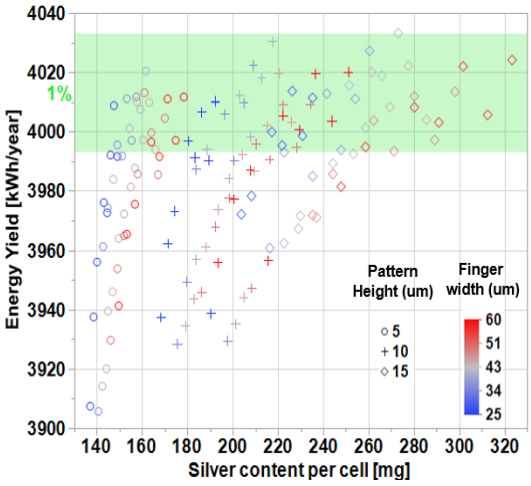

(c) Energy yield of the cells with different rear metal patterns plotted against their silver content. The green region denotes the metal patterns within the max 1% yield range.

Figure 5.9: Results - Rear metal optimization of East-West tilted system configuration

The figure 5.9a and 5.9b shows the relation between metal coverage, front side efficiency and bi-faciality factor. Rear metal coverage when reduced improves the bi-faciality factor but does not improve the yield. Yield is maintained constant for large portion of rear metal coverage range. Yield does not improve as the rear irradiance available at this configuration is very small to make any significant contribution to the yield. The figure 5.9c shows the simulated yield of the cells with different metal patterns against their silver content. The data points in the green region denotes the patterns within maximum 1% yield range.

Optimal pattern

The figure 5.10 shows the the metal optimization experiment with east-west tilted system. The green region represents the patterns with max 1% yield. The blue star represents the yield performance of the reference cell. The blue dots represents the metal patterns with pattern height above 5 μm and the red dots represents the metal patterns with pattern height of 5 μm and these are considered to be the R&D patterns.

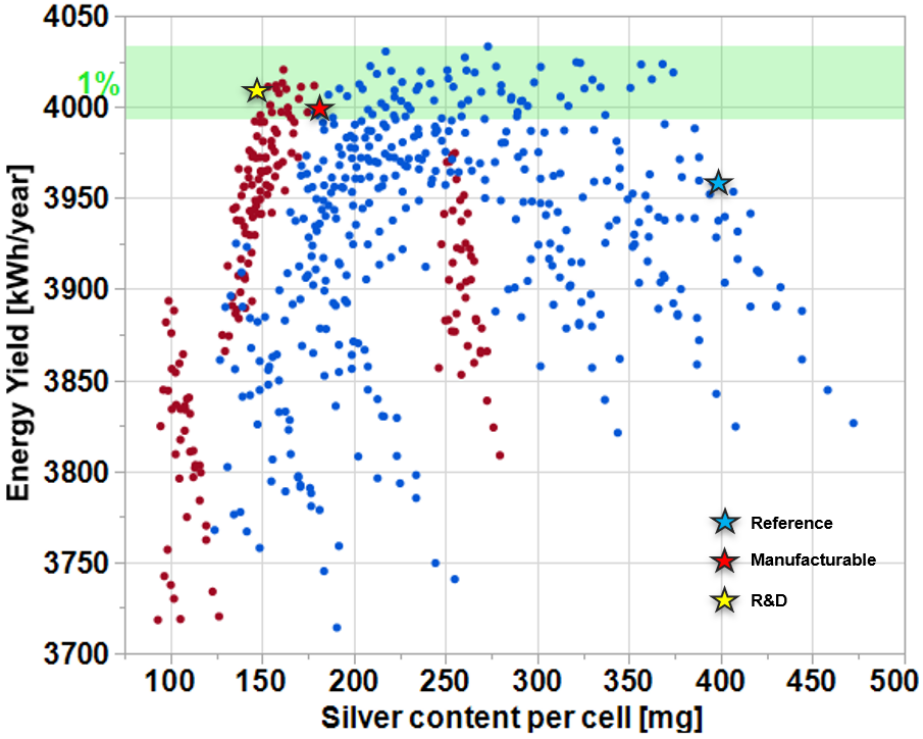

Figure 5.10: Metal optimization results of the east-west tilted system. Blue dots indicate patterns with height above 5um. Red dots indicate the pattern with thickness of 5 μm. The blue star denotes the reference patter. The red star denotes the optimal pattern with height above 5 μm. The yellow star denotes the optimal pattern with height 5 μm

The red stars represents the optimal pattern with pattern height more than 5 μm and the yellow star represents the optimal pattern with height 5 μm. The table 5.9 shows the chosen optimal patterns. The first set of the patterns are currently manufacturable patterns and the second set of the patterns are the R&D patterns. When we compare this with the optimal patterns for the equator facing system (table 5.7), we can notice that both are similar.

Side	No of Busbars [#]	Busbar width [μm]	Busbar height [μm]	No of Fingers [#]	Finger width [μm]	Finger height [μm]	Metal Coverage [%]	Yield change [%]	Silver saved [%]
Front	5	700	15	90	25	15	3.64	1	54.6
Rear			10	100	25	10	3.80		
Front	5	700	15	90	25	15	3.64	1.3	62.9
Rear			5	130	25	5	4.27		

Table 5.9: Optimal patterns for the East-West tilted system

The table 5.10 tabulates the IV parameters of the optimal cells. As seen earlier in the equator facing system, The I_{sc} and V_{oc} have improved while FF has reduced. We can clearly see that there is no difference in the optimal patterns for equator facing system and east-west tilted systems. We can use the same cells for both the locations have similar performance.

	Isc [A]	**Impp [A]**	**Voc [V]**	**Vmpp [V]**	**FF [%]**	**Pmpp [W]**	**Module efficiency [%]**	**Bi-faciality [-]**
M	10.11	9.47	41.11	33.10	75.5	313.85	19.1	0.86
R & D	10.11	9.47	41.21	33.06	75.18	313.27	19.04	0.87

Table 5.10: IV parameters of the cells with optimal metal patterns

5.3.3. East - West vertical system

The simulated system consists of 84 modules arranged in 7 rows with each row has 12 modules arranged in a matrix of 2 rows and 6 columns. Each row is placed at increased spacing from row 1. The results discussed are for the 12 modules of row 6, which has the maximum space.

Front metal optimization

First the front metal pattern is varied with the values from the variable matrix table 5.6. The rear metal patter is kept the same as that of the reference cell shown in the table 5.4. The figure 5.11 shows the results of yield simulation for the front metal optimization. At a pattern height of 20 μm, reducing the metal coverage by 40%, I_{sc} increases by 5.2%, V_{oc} increases by 1%, FF reduces by 1.5%, efficiency increases relatively by 4.65 %, bi-faciality reduces by 3.3% With the all the above changes yield improves by 2.5%. The above statistics is similar to the front metal optimization results of the equator facing and East-West tilted systems. In the figures 5.11a

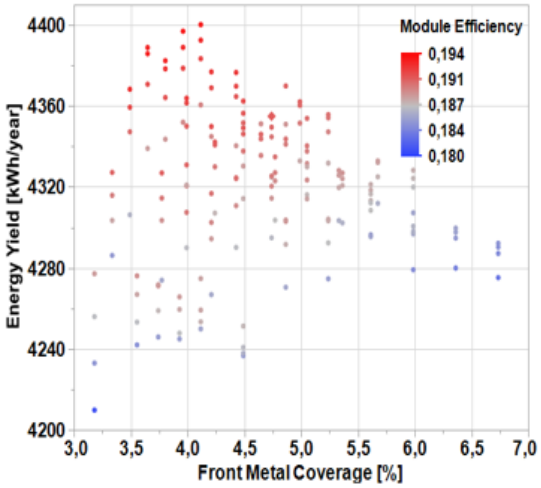

(a) Effect of front metal coverage on front efficiency and energy yield

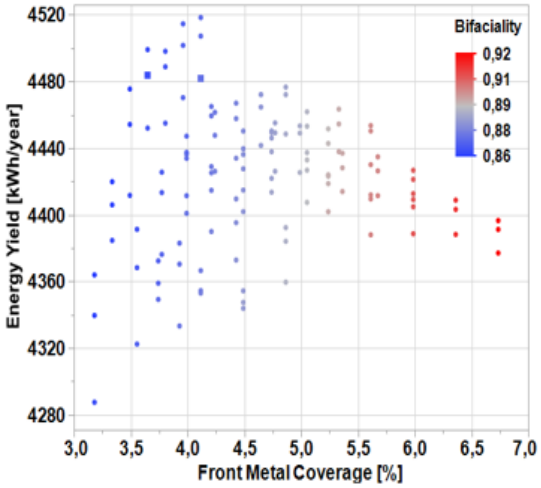

(b) Effect of front metal coverage on bi-faciality and energy yield

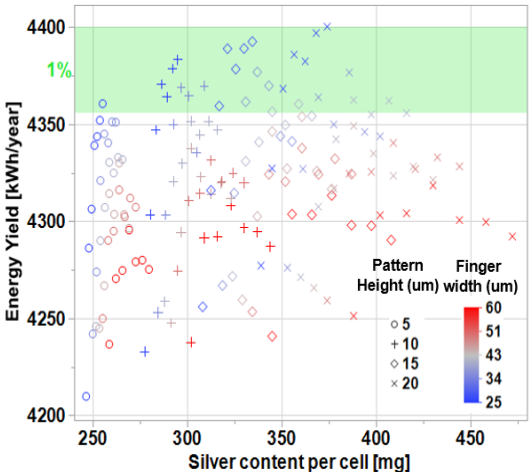

(c) Energy yield of the cells with different front metal patterns plotted against their silver content. The green region denotes the metal patterns within the max 1% yield range.

Figure 5.11: Results - Front metal optimization of east-west vertical system configuration

and 5.11b we can notice the relation between metal coverage, front side efficiency and bi-faciality factor. As the metal coverage decreases, front efficiency increases and bi-faciality decreases (because rear metal is kept

constant at this point). we can notice the critical front metal coverage of 4% with high efficiency and low bi-faciality factor, after which the yield starts to falls. The figure 5.11c shows the yield simulation results plotted against the silver content in a cell. The green region marked in the graph represents the metal patterns with maximum 1% yield. The blue star represents the yield performance of the reference cell. The optimal cell with less silver and yield within the yield range is chosen.

Rear metal optimization

The rear metal is varied with the chosen front metal. when the rear metal was varied, at 15 um pattern height, for metal reduction of 50%, I_{sc} reduces slightly by 0.1% , V_{oc} increases by 0.06%, fill factor reduces by 1.2%, efficiency reduces by 1.2% and bi-faciality increases by 9%. This leads to a yield increase of 3%. This is different from those of the other system configurations. Yield increased as we improved the bi-faciality factor. This is because the rear irradiance is equal to the front irradiance. The figures 5.12a and 5.12b shows the

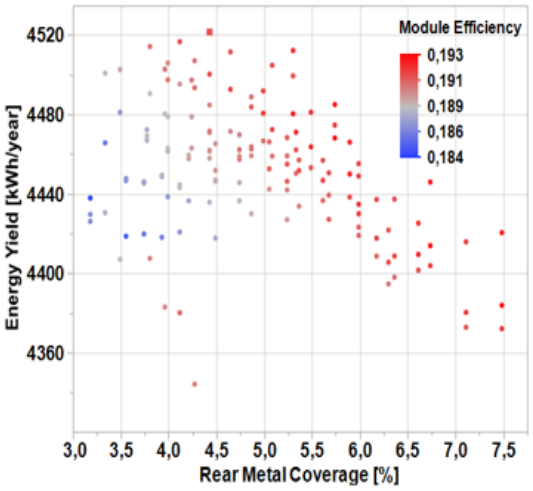

(a) Effect of rear metal coverage on front efficiency and energy yield

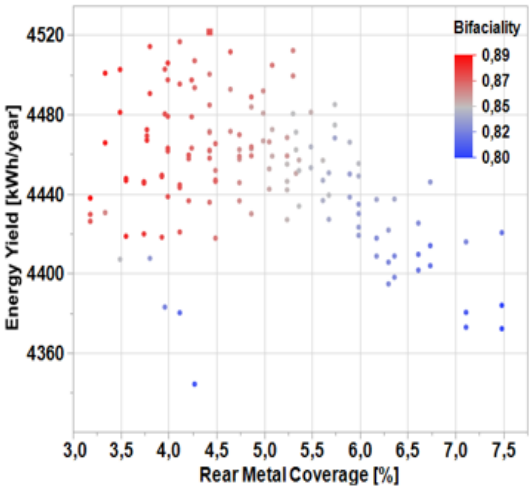

(b) Effect of rear metal coverage on bi-faciality and energy yield

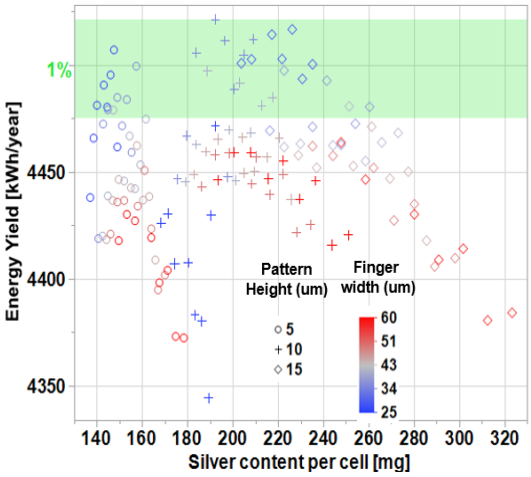

(c) Energy yield of the cells with different rear metal patterns plotted against their silver content. The green region denotes the metal patterns within the max 1% yield range.

Figure 5.12: Results - Rear metal optimization of east-west vertical system configuration

relationship between metal coverage, front side efficiency and bi-faciality factor. We notice that bi-faciality factor increases with reduction in metal coverage and front side efficiency is remains almost unaffected for large range of reduction in the rear metal coverage. But the yield increases with the bi-faciality factor. We can notice the critical efficiency and bi-faciality factor after which yield starts to drop. This is because the loss due

to the FF reduction becomes dominant after that point. The figure 5.12c shows the yield simulated plotted against the silver content of the cell. the green region shows the metal patterns with max 1% yield. There are thinner and narrower patterns within the green region which has silver content as less 140 mg per cell.

Optimal pattern

The figure 5.13 shows the the metal optimization experiment of East-West vertical systems. The green region represents the patterns with max 1% yield. The blue star represents the yield performance of the reference cell. The blue dots represents the metal patterns with pattern height more than 5 μm and red dots represents the metal patterns with pattern height of 5 μm. The red star represent the optimal pattern with pattern height

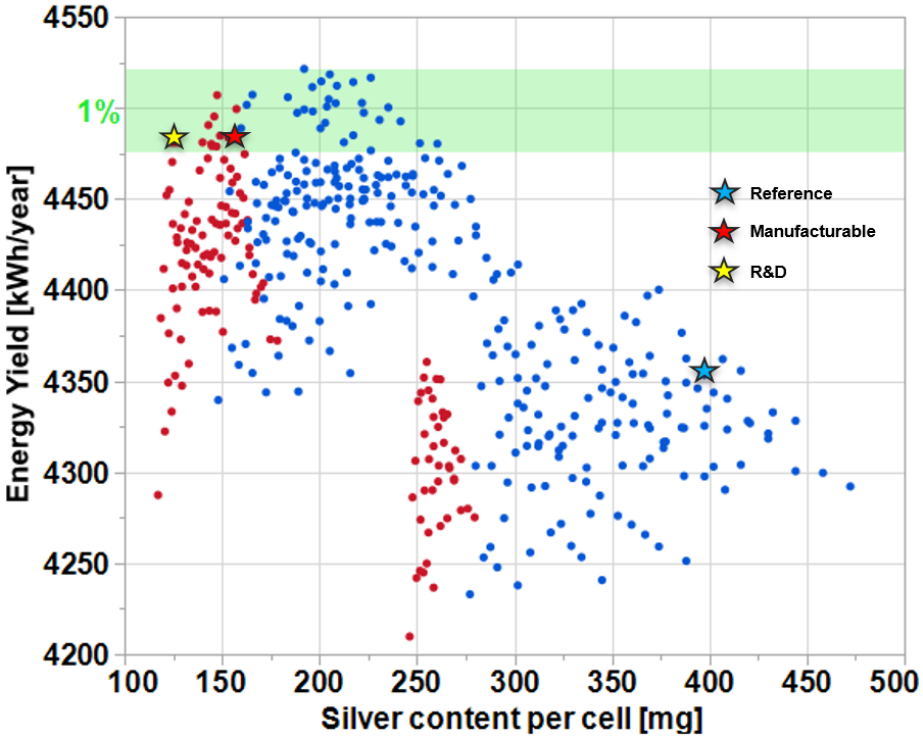

Figure 5.13: Metal optimization results of the East-West vertical system. Blue dots indicate patterns with height above 5um. Red dots indicate the pattern with thickness of 5 μm. The blue star denotes the reference patter. The red star denotes the optimal pattern with height above 5 μm. The yellow star denotes the optimal pattern with height 5 um

more than 5 μm and yellow star denotes the optimal pattern with 5 μm height. The table 5.11 tabulates the optimal metal patterns chosen. The first set of the pattern is the currently manufacturable pattern. When we compare this with the optimal pattern of the East-West tilted system and Equator facing system, these patterns are thinner. This is because the irradiation intensity on the vertical modules is less and well distributed through out the day and also the module temperature is also less than that of the other systems.

Side	No of Busbars [#]	Busbar width [μm]	Busbar height [μm]	No of Fingers [#]	Finger width [μm]	Finger height [μm]	Metal Coverage [%]	Yield change [%]	Silver saved [%]
Front	5	700	10	90	25	10	3.65	2.96	60.53
Rear			10	100	35	10	4.43		
Front	5	700	5	120	25	5	4.12	2.91	68.31
Rear			10	100	35	10	4.4284		

Table 5.11: Manufacturable optimal pattern with lesser metal and better yield than the reference cell

The table 5.12 shows the IV parameter of the optimal cells for the East-West vertical systems. The values are similar to that of the other system configurations.

	Isc [A]	Impp [A]	Voc [V]	Vmpp [V]	FF [%]	Pmpp [W]	Module efficiency [%]	Bi-faciality [-]
M	10.11	9.47	41.17	32.98	75.04	312.24	19.0	0.86
R & D	10.01	9.4	41.07	32.94	75.24	309.67	18.82	0.87

Table 5.12: IV parameters of the optimized cells

5.4. Conclusion

After optimizing the front metal, it was observed that the yield was more sensitive to the front metal coverage as it directly affected the front side efficiency. The above behavior was seen in all three system configurations. With an optimal front pattern, when the rear metal pattern was optimized by reducing the rear metal coverage and thickness, FF reduced and at the same time the bi-faciality factor increased. The loss of yield due to the FF reduction was compensated by the increased bi-faciality factor. The rear metal was reduced until the loss due to fill factor cannot be compensated anymore by the bi-faciality factor. Yield increase due to bi-faciality increase was minimal in equator facing and east-west tilted systems when compared to the vertical systems. Due to this fact the vertical systems have thinner optimal metal patterns.

		Busbars			Fingers			Metal Coverage (%)
Configuration	**Side**	**Number**	**Width (μm)**	**Height (μm)**	**Number**	**Width (μm)**	**Height (μm)**	
Equator Facing	Front	4	800	15	90	25	15	3.63
	Rear			10	120	25	10	4.11
East-West Tilted	Front	4	800	15	85	25	15	3.42
	Rear			10	100	25	10	3.8
East-West Vertical	Front	4	800	10	90	25	10	3.63
	Rear			10	100	35	10	4.91

Table 5.13: The optimal metal pattern for different system configuration

The table 5.13 compares the optimal patterns for different system configurations. So, we can conclude that metal pattern in the cells for vertical systems can be made thinner than those for other system configurations, saving more silver.

6

Yield maximizing cell architecture for different climatic conditions

6.1. Introduction

Reaching the theoretical efficiency of 29.43% [40] has been the driver for the c-Si industry to research different cell architectures. Each architecture employs different strategies to reach the the theoretical efficiency limit. By that each architecture has varying magnitudes of the IV parameters contributing to the efficiency. Thus each architecture has some advantage over the other. This chapter uses the results of the previous experiment yield maximizing parameter (chapter 3) and qualitatively assess and categorize different solar cell technologies available in the market based on its suitability to different climatic zones. It is to be noted that the comparison made among cell technologies are purely based on magnitude of their IV parameters. Reference cells chosen for each technology are based on the their cell area (more that $100 m^2$ and availability of data in the public domain (data for recent development in some technologies were not available). So there is high uncertainty in the results concluded but this could be seen as a start for this exercise which can be perfected in future works.

6.2. Architectures

This experiment considers different c-Si architectures like PERC, PERL, PERT, TOPCon and hetero-junction IBC. Below section discusses the unique features of each architecture, their advantage, record efficiency at lab scale and at industrial scale.

6.2.1. Passivated Emitter Rear Contact solar cell (PERC)

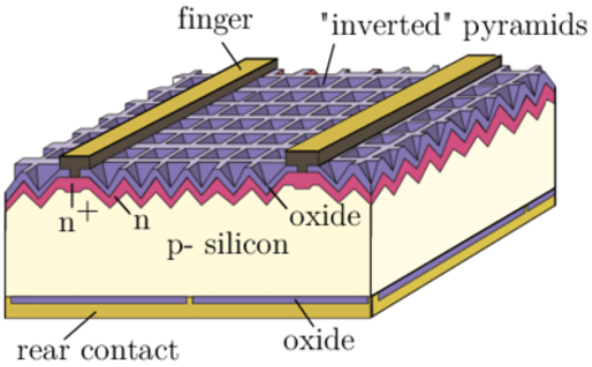

Figure 6.1: Schematic cross section of p-type PERC cell as described in [41]

The full rear *Al* BSF solar cell has limited efficiency of 20% because of marginal recombination suppressing at the rear and absorption of infrared light by *Al* [42]. PERC cell was first introduced in 1989 [41] to tackle

the above mentioned issue. The distinctive feature of the PERC cell was the reduced rear metal contact area which reduces the surface recombination considerably. This led to an increased efficiency at lab scale of 22.8% [41] (J_{sc} = 40.3 mA/cm^2; V_{oc} = 696 mV; FF = 81.4 %) for cell area of 4cm^2. The figure 6.1 shows the schematic representation of the PERC described in [41].

At lab scale the recombination was suppressed by rear passivation of SiO_2 layer grown at high temperatures of 900°C [41]. To achieve lab scale efficiency at industrial scale, passivation at lower temperatures was required [43]. First PERC module was first commercialized by Suntech solar with efficiency of 19.7% [44] with SiN_x rear passivation. With continuous efforts on improving the rear passivation, record cell efficiency of 22% was achieved by SolarWorld innovations in 2015 with rear passivation stack of AlO_x and SiN_x [45]. The IV parameter of the cell are tabulated in the table 6.1. The recent record efficiency of 24% was reported by LONGI solar in Jan 2019 [46]. The technical details of the which are not made public.

Area [cm2]	Voc [mV]	Jsc [V]	FF [%]	Eta [%]
242.8	679	39.90	81.31	22.03

Table 6.1: IV parameters of record efficient PERC solar cell at industrial scale [47]

6.2.2. Passivated Emitter Rear Locally diffused solar cell(PERL)

PERL architecture is an advancement to the PERC architecture with proven lab scale efficiency of 24.7% [48] (J_{sc} = 42.2 mA/cm^2; V_{oc} = 706 mV; FF = 82.8%) for 4 cm^2 cell area. The main limitation of the PERC cell was recombination due to the direct metal contact to the silicon solar cell. This was addressed by PERL architecture by introducing a highly doped local boron diffusion over the metal contact at the rear. This led to V_{oc} over 700 mV [48]. The lab scale cell with record efficiency was realized using p-type float zone substrate with resistivity of 1Ω.cm

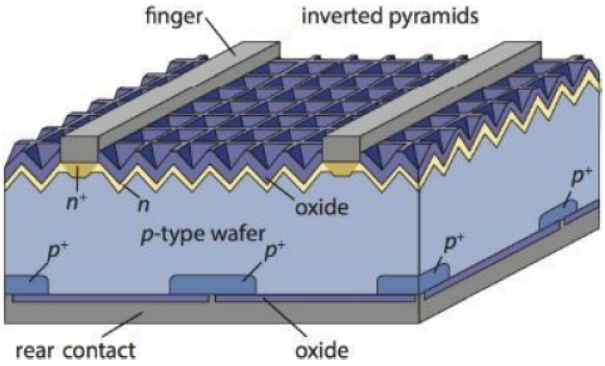

Figure 6.2: Schematic cross section of p-tpye PERL cell [49]

The industrialization of the PERL cells started at same time as that of the PERC cells. In 2011, Suntech power announced its PERL module with the cell efficiency of 20.3%. The heavily doped p^+ region at the rear side acts as localized BSF and reduces the minority carrier recombination. This led to an higher J_{sc} values when compared to then available PERC cells [44]. Further improvements were made to improve rear passivation with Al_2O_3/SiO_xN_y stack to cell efficiency of 21% at industrial level [50]. The IV parameters of the industrial scale cells are tabulated in the table 6.2.

Area [cm2]	Voc [mV]	Jsc [V]	FF [%]	Eta [%]
239	669	40.1	78.1	21

Table 6.2: IV parameters of record efficient industrial scale PERL solar cell [50]

The limitation of the efficiency in PERL is mainly due to the increased series resistance due to the current crowding at rear contact points [51].

6.2.3. Passivated Emitter Rear Totally diffused solar cell (PERT)

PERT architecture is similar to the PERL architecture except a lightly doped boron layer is diffused over the entire rear surface. This is to reduce the current crowding effect seen in PERL cells. The record efficiency of 24.5% ($J_{sc} = 41.6\,mA/cm^2; V_{oc} = 704\,mV; FF = 83.5\%$) was realized in lab scale using a p-type MCZ Si-wafer [48]. The figure 6.3a represents the p-PERT cell.

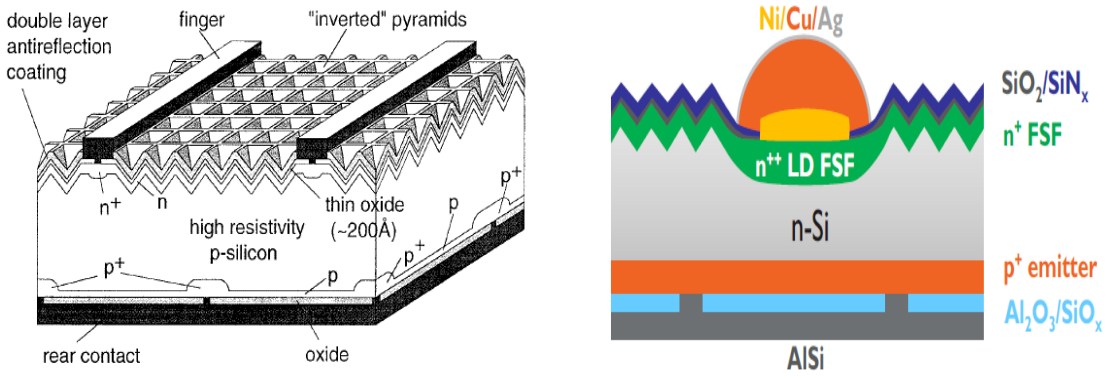

(a) (b)

Figure 6.3: a - Schematic cross section of p-type PERT cell. b -Schematic cross section of rear junction n-type PERT cell.

Although record efficiency was achieved in p type PERT cell, PV industry started to move towards the n-type wafers for its excellent resistance to the light induced degradation. One of the earlier industrial scale n-PERT cell was realized with an efficiency of 20.5% by L. Tous et al [52]. On continuous improvements in metalization process, back reflection and selective front surface field, efficiency of 22.5% was achieved [53].

Area [cm2]	Voc [mV]	Jsc [V]	FF [%]	Eta [%]
227	689	40.3	80.9	22.5

Table 6.3: IV parameters of record efficient industrial scale PERT solar cell.

6.2.4. Tunnel Oxide Passivated Contact cell (TOPCon)

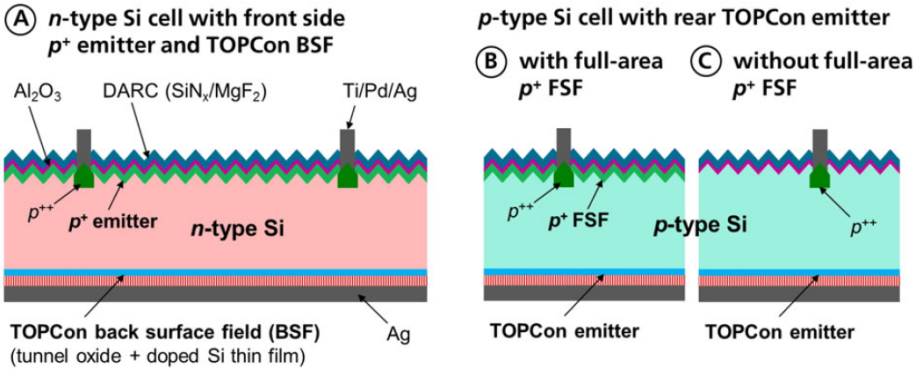

Figure 6.4: A. Schematic cross section of n-type solar cell with boron doped front emitter and TOPCon rear. B and C are the p-type TOPCon cells with with and without FSF [54].

Unlike the PERC cells which employ partial contacts in the rear to reduce recombination, TOPCon cells employs full area, carrier selective passivated contacts at the rear[55]. TOPCon architecture was introduced by Fraunhofer ISE. TOPCon removes patterning from back side which helps to increase the efficiency by reducing the current path. The rear passivation is achieved by the thin SiO_2 layer which will allow the charge carriers to tunnel through [55]. A thin layer of highly doped poly-crystalline or nano-crystalline Si layer is deposited on top of the oxide layer to pull the charge carriers [54].

Due to the excellent passivation of the Polysilicon/SiO2 layer, TOPCon cell have very high V_{oc} [54]. Lack of lateral current flow ensures a high FF [54]. The record efficiency of 25.7% for TOPCon architecture was achieved by Richter et al [56] with ntype wafer. The figure 6.4 (left) shows the cell structure corresponding to the record cell. The TOPCon architecture was also implemented with a p-type base with and without a Front Surface field (FSF) reaching the efficiency of 24.3% and 23.9% respectively. This was also achieved by Ricter et al [54]. This cell is shown in the figure 6.4 (right). As an advancement in TOPCon architecture, feasibility of industrially viable double sided TOPCon cells has be proved by Zhi Peng Ling, et al [57]. Further industrially feasible bi-faciality in the TOPCon cells have been implemented at an efficiency of 21% by ECN.TNO [33].

N-type base: The record efficiency of 25.7% ($J_{sc} = 42.4\,mA/cm^2; V_{oc} = 724.9\,mV; FF = 83.3\%$) was achieved with n-type float zone Si wafer. The cell had a wafer thickness of 200um with 1 ohm.cm resistivity. The front emitter was boron doped P^+ layer passivated by 10 nm Al_2O_3 layer resulted in a sheet resistance of 300 ohm/sq [56]. The front side was coated with double anti reflection coating of SiN_x and MgF_2. Heavily doped P^{++} is diffused at the bottom of the front contacts to reduce the recombination. The rear side contact surface has SiO_2 layer covered with 15nm thick doped Si layer [56]. The rear metallization is achieved by thermally evaporating Ag.

P-type base: The record efficiency of the p-type base cell was 24.3% ($J_{sc} = 42.4 mA/cm^2; V_{oc} = 714.2 mV; FF =$ 80.2%). It was achieved by applying the same structure of n-type cell with a P^+ front surface field. This cell is a rear junction cell. The P-type base is 200 um thick float zone wafer with 10 ohm.cm resistivity. The front surface field has the sheet resistance of 300 ohm/sq.

The large area TOPCon cell efficiency of 23.4% was achieved by FSH ISE [58] and its IV parameters are tabulated in the table 6.4.

Area [cm2]	Voc [mV]	Jsc [V]	FF [%]	Eta [%]
100	697	41.4	81.2	23.4

Table 6.4: IV parameters of record efficient TOPCon solar cell.

6.2.5. Hetero Junction Interdigitated Back Contact cells (HJ-IBC)

HJ-IBC solar cell architecture holds the record conversion efficiency for C-si solar cell. Yoshikawa et.al [59] achieved the record efficiency of 26.6% on about $180 cm^2$ wafer with this architecture. It combines the advantages of the high efficiency concepts of hetero junction and inter-digitated back contact to achieve this record efficiency.

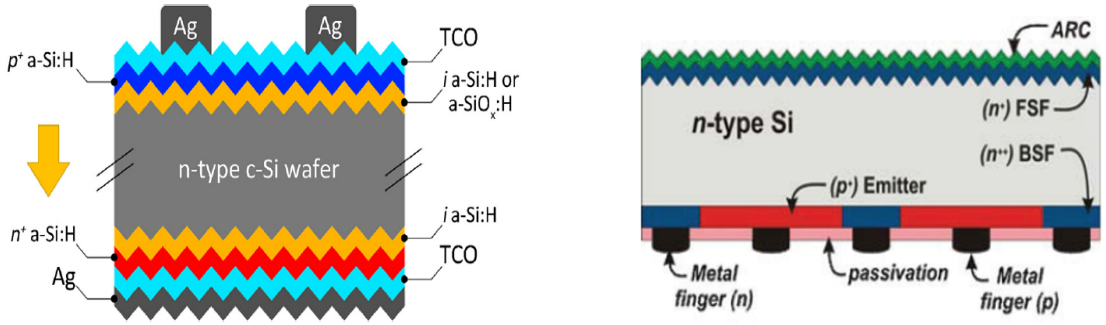

(a) (b)

Figure 6.5: a - cross section of a typical hetero-junction solar cell. b - cross section of a typical Interdigitated back contact solar cell

Hetero - junction structure is junction between silicon materials of different band gap. The mono c-Si material with band gap of 1.12 eV forms hetero junction with hydrogenated a-si material of band gap 1.7 eV. The a-Si layer acts an excellent passivation layer [49]. The doped amorphous silicon layer are used to form junctions and act as charge collectors thus isolating the metal contacts from the bulk forming a almost recombination free contacts [60]. Thus hetero junction structure has higher carrier life times and high Voc.

The advantage of the inter-digitated back contact structure is that it does not have any shading loss at the front side leading to higher J_{sc}. The IBC cells has n-type as the bulk for its immunity towards the light

induced degradation [49]. The front surface is passivated by highly doped n^+ region acting as front surface field. At the rear, it localized pn junctions to separate the holes and electrons. So, there are two metal grids at the rear. Since the grids are the rear, it can be made wider and thicker to reduce the resistance and improve the FF [49]. The main disadvantage of this architecture is that it has multiple processing steps with high costs and high processing time. This may lead to complexity in large scale industrial manufacturing [61].

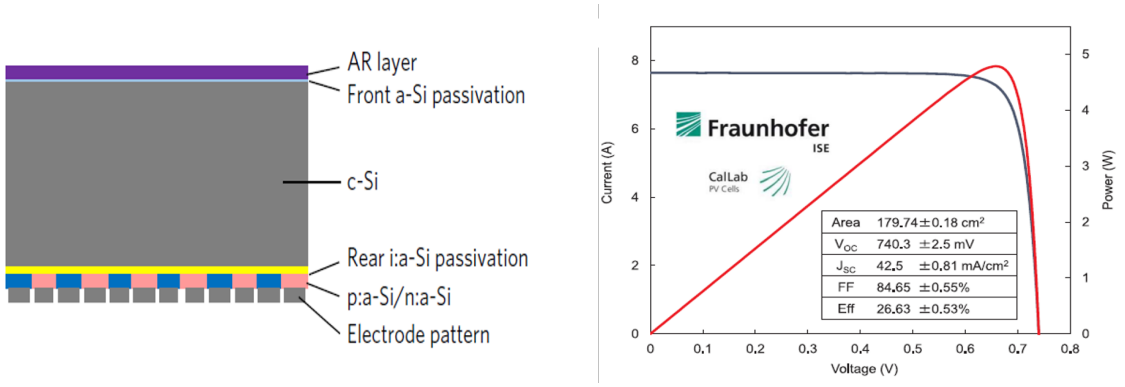

(a) (b)

Figure 6.6: a - cross section of record efficient HJ-IBC solar cell described in [59]. b - IV and PV curve of the HJ-IBC cell described in [59]

The record efficient HJ-IBC cell is shown in the figure 6.6. It has an 200um thick n-type bulk with resistivity of 7 ohm.cm. Front side is passivated by a-si:H layer. Di-electric anti reflection layer is coated on top of it. The rear side passivated with P^+ HJ layer stack and N^+ HJ layer stack. These stacks are patterned into inter-digitated layer at the rear. The metal grid structure is formed on both p and n layers to form an ohmic contact [59]. The IV characteristic shown in the figure 6.6 were measured and certified by Fraunhofer Institute of Solar Energy. Below table shows the IV characteristics of the record efficient solar cell.

Area [cm2]	Voc [mV]	Jsc [V]	FF [%]	Eta [%]
180	740	42.5	84.6	26.63

Table 6.5: IV parameters of record efficient HJ-IBC solar cell [59]

6.3. Climatic suitability of solar cells

To identify the technology suitable for different climatic zones we consider record efficient cells available at the industrial scale. Crystalline silicon cells with area more than 100 cm^2 are considered as industrial scale cell. The yield maximizing parameter experiment (chapter 3) was done with material parameters of a c-si cell.

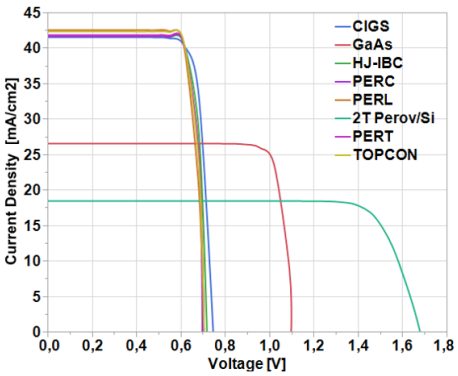

Figure 6.7: IV curves of the different cell technologies scaled to efficiency of 25%

To compare each of the architectures the record efficient cells available at the industrial scale is scaled to an efficiency of 25%. The table 6.6 show the IV parameters of the record efficient cells at 25% efficiency. Using

the results of the experiment yield maximizing parameter, architectures can be mapped to different climatic zones. To recall, at oceanic climate conditions the cell with higher $V_{oc} \times I_{sc}$ product gives better yield. At tropical climates, the cells with higher V_{oc} gives better yield and at hot desert climates, the cell with high $V_{oc} \times FF$ product gives better yield. Using the above rules all c-si cells will be categorized.

Cell Architecture	Voc [mV]	Jsc [mA/ cm2]	FF [%]	Voc x Jsc [mV.mA/cm2]	Voc x FF [V]
Crystalline Silicon					
HJ - IBC	724.8	41.6	82.9	30171	60058
TOPCon	712.2	42.3	83.0	30130	59096
PERC	708.3	41.6	84.8	29477	60069
PERT	714.0	41.8	83.8	29820	59861
PERL	709.6	42.5	82.8	30180	58779

Table 6.6: IV parameters of the c-si solar cells with their efficiency scaled to 25%

PERL: The PERL architecture of the c-Si solar cell has higher $V_{oc} \times I_{sc}$ product among the c-Si solar cells. Along with that it has highest I_{sc} and lower FF. This makes the cell best for the low temperature and low irradiation conditions of oceanic climate.

TOPCon: The TOPCon cells with the next best $V_{oc} \times I_{sc}$ product have better V_{oc} compared to PERL. This makes it suitable for slightly higher irradiance and temperature conditions compared to PERL cells.

HJ-IBC: The hetero-junction IBC cells are have second highest $V_{oc} \times I_{sc}$ product, highest V_{oc} and a reasonably good FF. With this HJ-IBC are more suitable for high irradiance and temperature conditions compared to PERL and TOPCon cells.

PERT: The PERT cells have better V_{oc} and FF when compared to TOPCon cells. This criteria pushes the PERT cells towards higher temperature and irradiance region making it more suitable for tropical climatic zone.

PERC: The PERC cells have highest $V_{oc} \times FF$ product among c-si solar cells. It also has the lowest I_{sc} and highest FF. This makes it suitable for high albedo conditions in hot desert climates.

Based on the above discussions the figure 6.8 shows the the cells that are expected to give maximum yield at different regions of the irradiance and temperature.

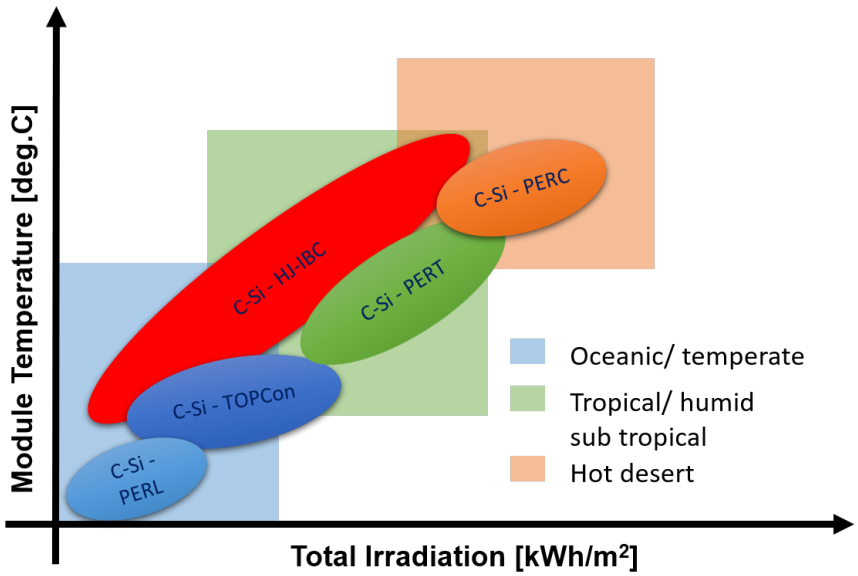

Figure 6.8: c-Si cell technologies that are expected to give maximum yield at different regions of the irradiance and temperature.

6.4. Conclusion

With above qualitative analysis, we arrived at an operating zone for each of the solar cell technologies. More the Jsc, the cells perform best at low irradiation, More the FF, the cell performs best at high irradiance. Higher the V_{oc} better it can perform in high temperature conditions. c-Si HJ-IBC solar cells performs best over a wide range of irradiance and temperature. With the increasing order of FF, PERL, TOPCon, PERT, PERC cells arranged in from left to right along the irradiance axis while magnitude of V_{oc} decides their position along the temperature axis. As stated before the results are of high uncertainty as the cells chosen may not of the latest of that kind and also monofacial/bifacial aspects of the cells are ignored and only the IV parameters are considered. This study can be improved further in future. Understanding the best operating conditions for each of the solar technologies, we can minimize the yield losses thereby, effectively reducing the least cost of electricity(LCoE).

7

Conclusion

This thesis on geography based design for better LCoE explained different design solutions to reduce the cost or to improve the yield, thus effectively reducing the LCoE of the system. First we identified that in a tilted system, yield loss due to loss in front side efficiency cannot be compensated with increase in bi-faciality factor in most cases. Then we found that for a same efficiency, with varying magnitude of IV parameters, energy yield varies. With that we identified that each climatic zone had a particular IV parameter that when increased, improved the yield. It was determined that increasing the $V_{oc}xI_{sc}$ product improves the yield at oceanic climate. Whereas, improving V_{oc} increased the yield at tropical climate and improving $V_{oc}xFF$ product increased the yield at high irradiance conditions of hot desert climate. yield increase up to 5% was noted. The figure 7.1a shows the yield maximizing parameters for different climatic conditions.

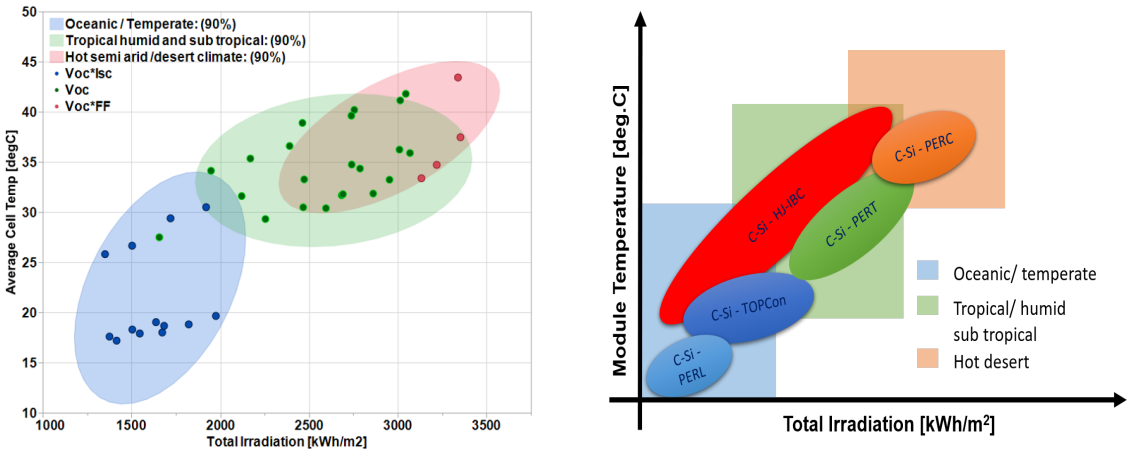

(a) (b)

Figure 7.1: a - Results of the yield maximizing parameter experiment. b - graph showing solar cell technologies suitable for different climatic conditions

Next when the metal pattern of a solar cell was varied to manipulate the IV parameters to improve the yield of equator facing system, different climatic zones had different optimal metal patterns(chapter 4). The optimal patterns for oceanic climate had the least metal coverage with narrow and thinner fingers at the front which had high $V_{oc}xI_{sc}$ product and less FF. Optimal metal patterns had higher FF and lower I_{sc} as we moved from oceanic to hot desert climate. This was in correlation with the results of the the yield maximizing parameter experiment. The results showed that yield could not be improved more than 1% but 50% of the silver could be saved. The optimal metal pattern for a vertical system had thinner pattern when compared to the equator facing system due to the less irradiance intensity incident on it (chapter 5). The metal reduction of 50% motivates the industry to research the printing technology for narrower and thinner fingers.

The results final study (chapter 6) acts as a guide for deploying the appropriate technology at different climatic conditions for better yield. We found different cell technologies the perform better at different oper-

ating zones. The results in the figure 7.1 b gives the best performance zones of each of the solar technologies under assumed constraints. This study is only based on the IV parameter magnitude and has lot of scope for improvement.

The entirety of this thesis work was based on the results of simulations. It would have been impractical to obtain these results on trial and error practical method. The amount of results obtained in short period of time makes us realize the importance of simulators in the field of research. This gives motivation to create more and better simulators to aid us in future researches. The above discussed results of each of the experiment will act as guide in the future design and deployment of PV systems for reducing the LCoE.

A

Optimal Tilt

The yield simulated in the all of the previous experiments was with a tilt angle that was optimized for maximum yield at that location. Optimal tilt for different albedos were calculated for the module elevation of 0.5 m. The results of the experiment is presented below.

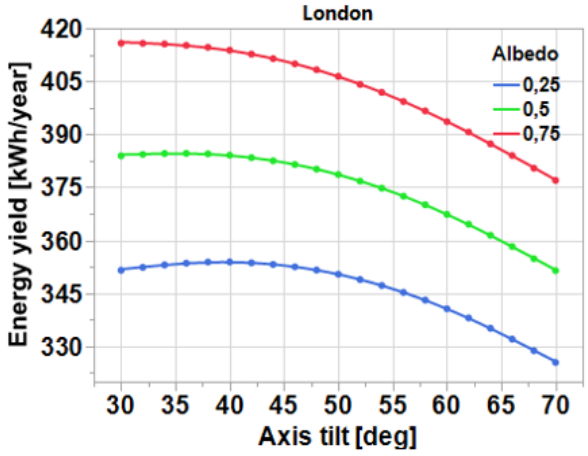

Figure A.1: London - Yield at different tilt angles

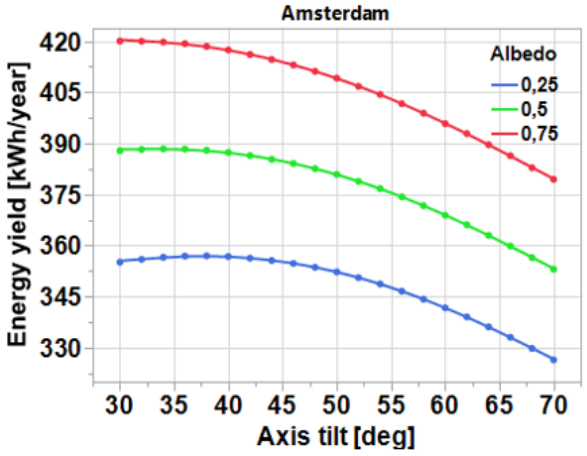

Figure A.2: Amsterdam - Yield at different tilt angles

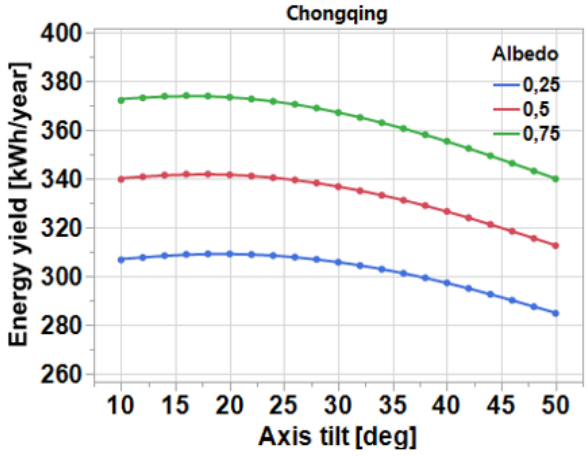

Figure A.3: Chongqing - Yield at different tilt angles

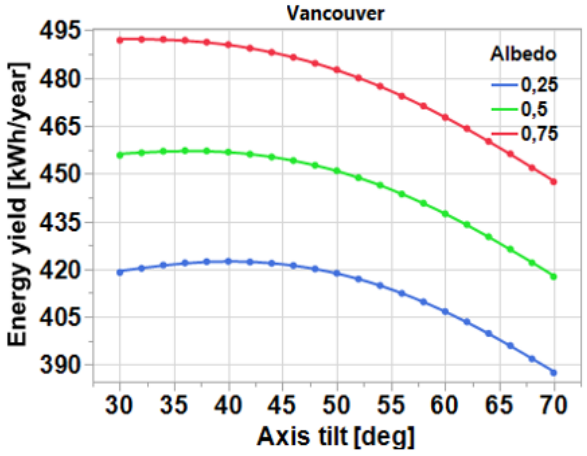

Figure A.4: Vancouver - Yield at different tilt angles

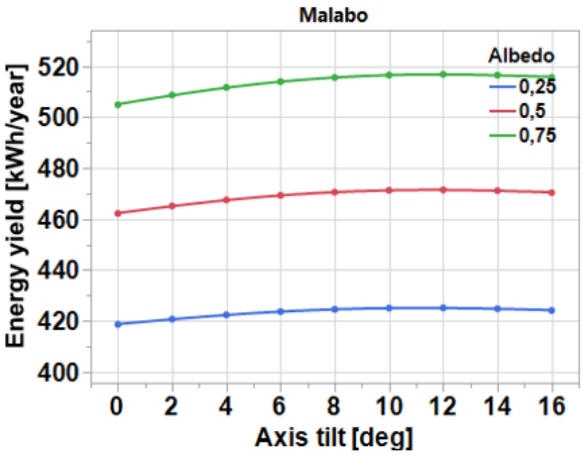

Figure A.5: Malabo - Yield at different tilt angles

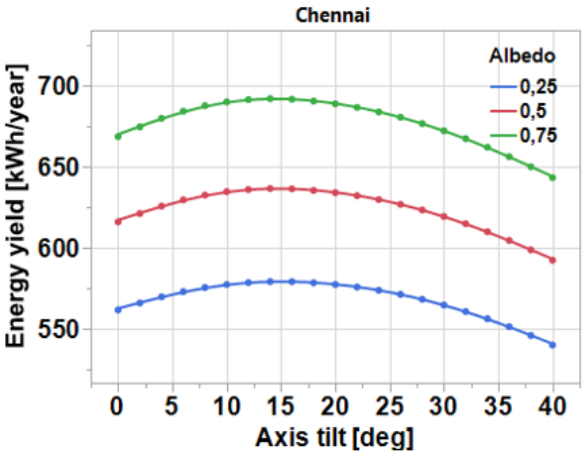

Figure A.6: Chennai - Yield at different tilt angles

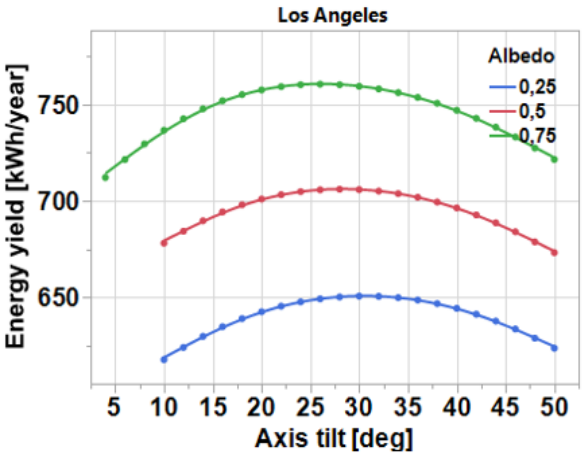

Figure A.7: Los Angeles - Yield at different tilt angles

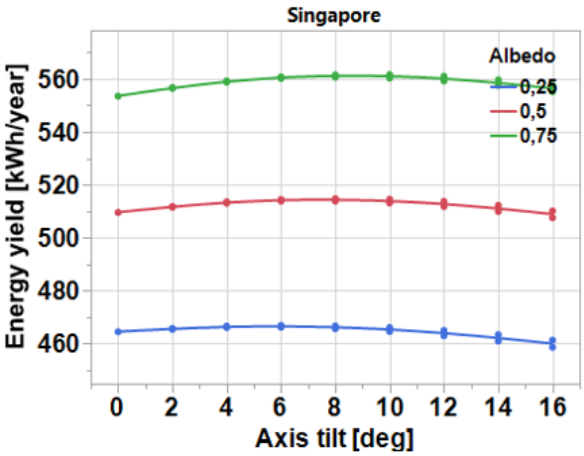

Figure A.8: Singapore - Yield at different tilt angles

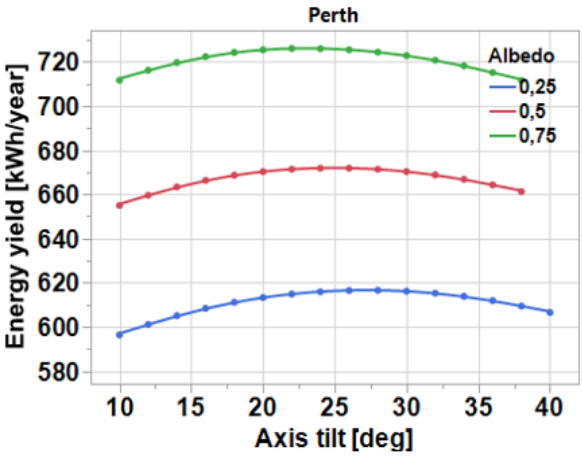

Figure A.9: Perth - Yield at different tilt angles

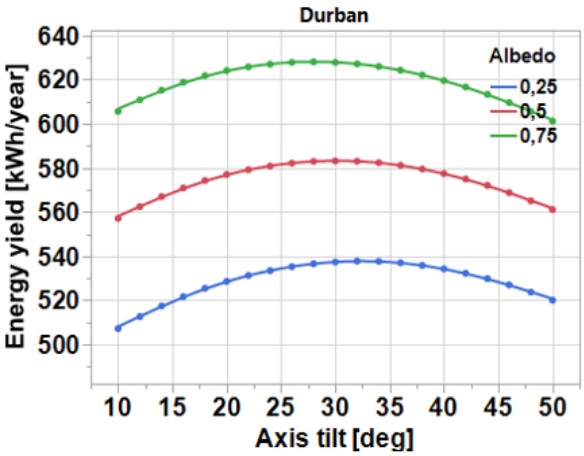

Figure A.10: Durban - Yield at different tilt angles

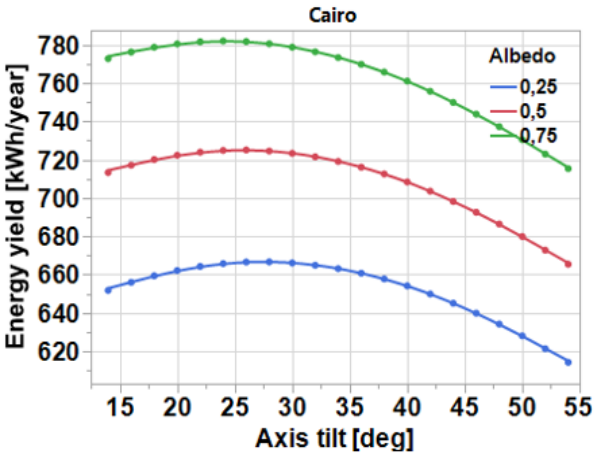

Figure A.11: Cairo - Yield at different tilt angles

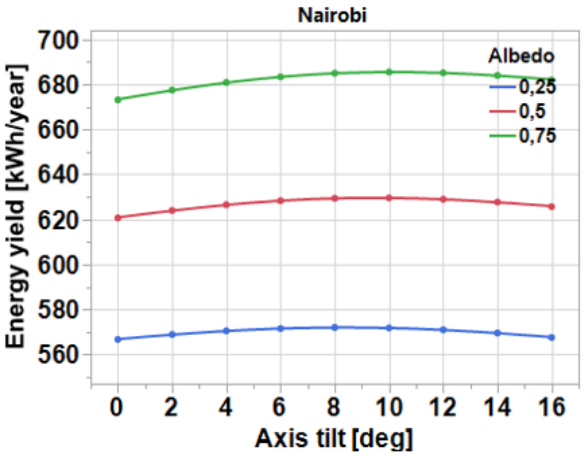

Figure A.12: Nairobi - Yield at different tilt angles

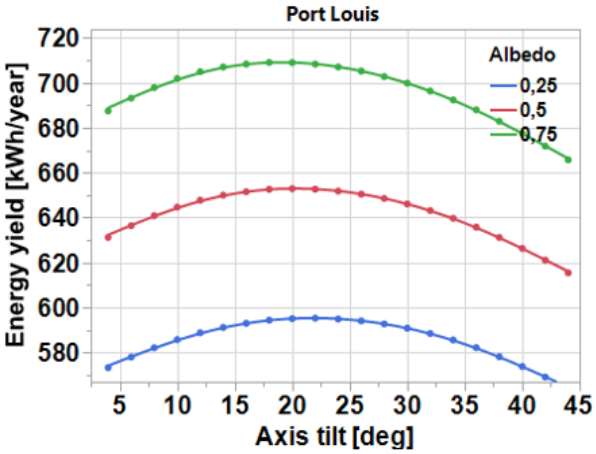

Figure A.13: Port Louis - Yield at different tilt angles

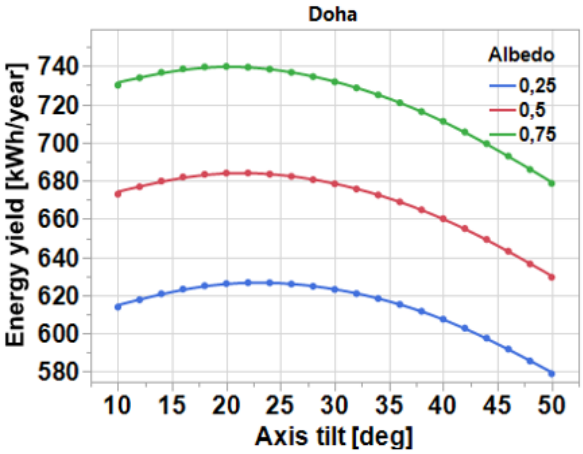

Figure A.14: Doha - Yield at different tilt angles

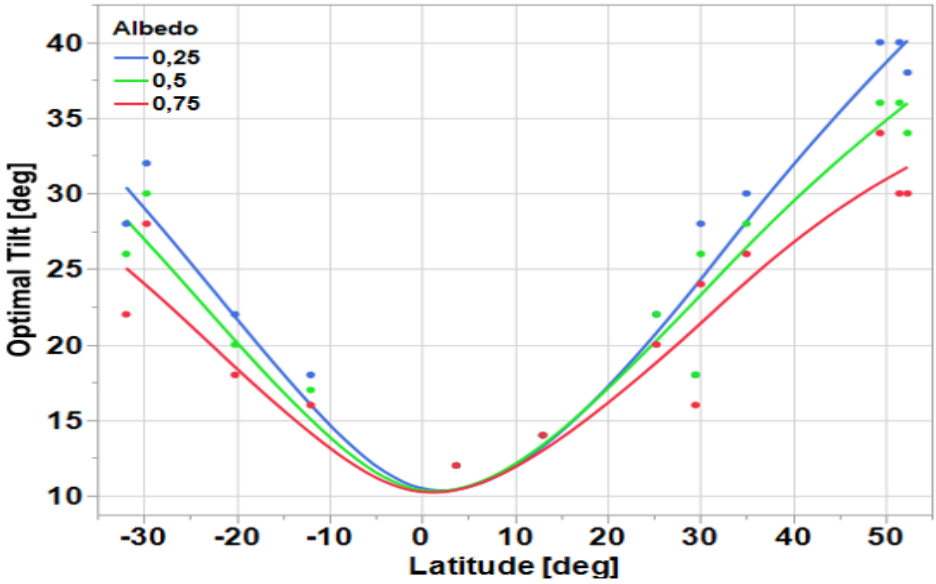

Figure A.15: Variation of optimal tilt with the latitude for different albedo

B

Yield maximizing parameter - additional results

B.1. Oceanic Climate - London

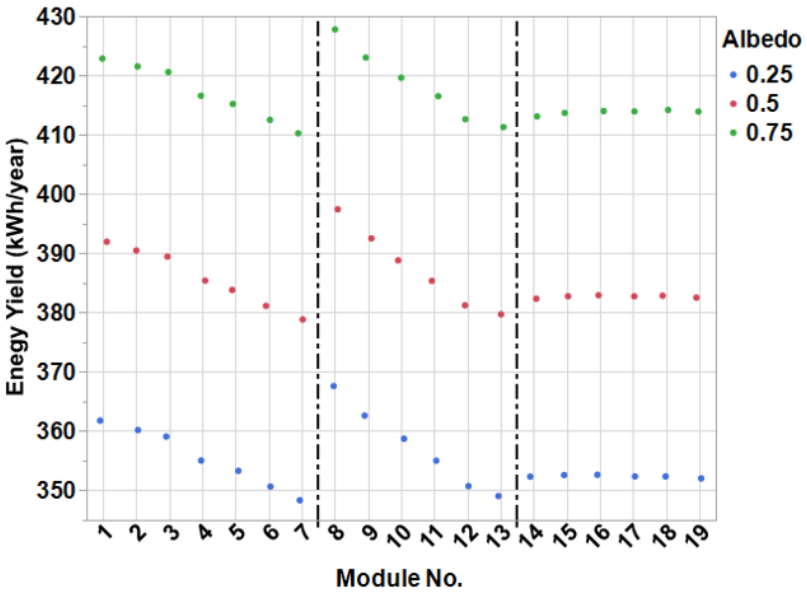

Figure B.1: Yield simulation results for the theoretical modules for different ground albedo at London

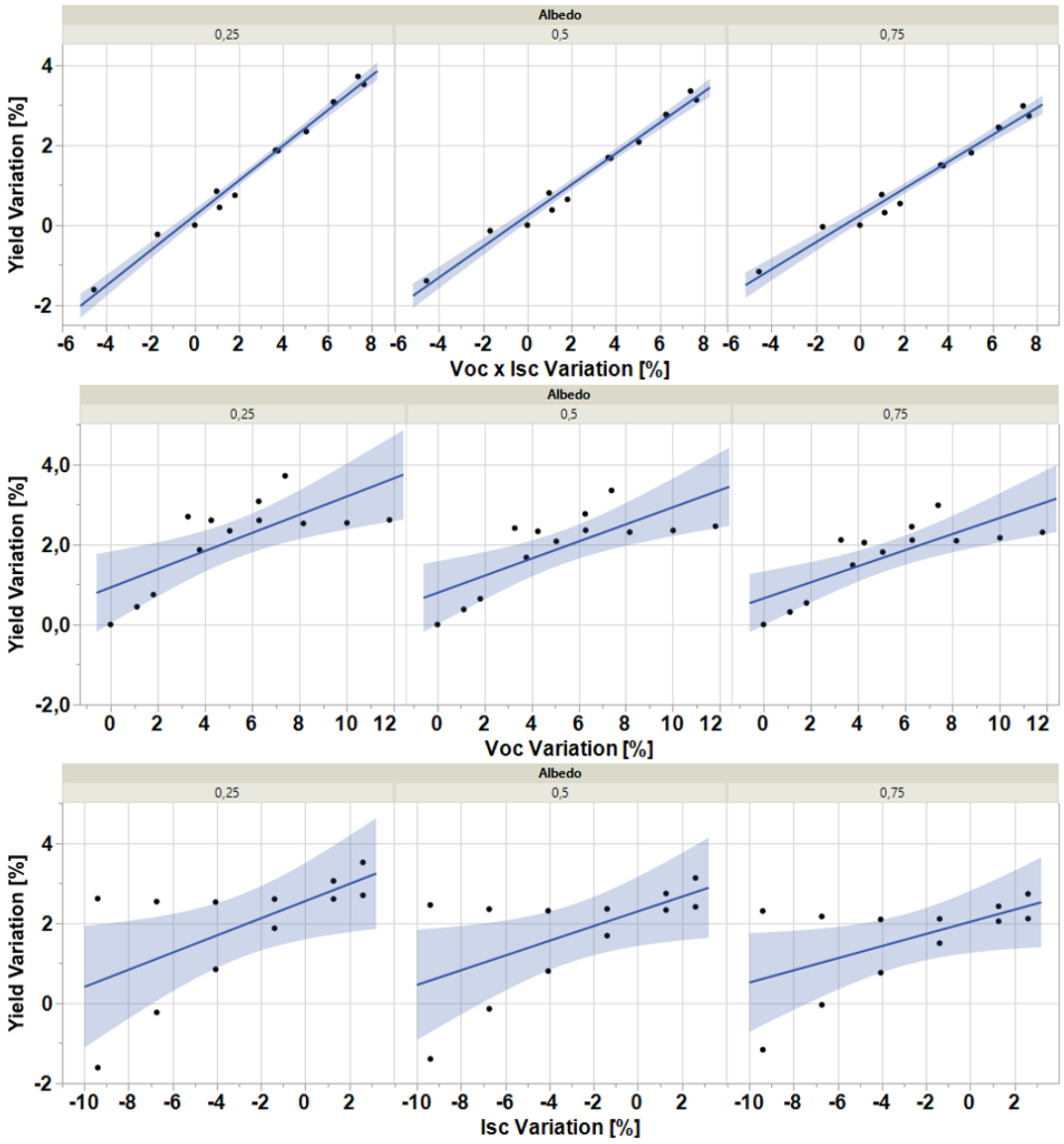

Figure B.2: yield variation against the variation of different parameters at different albedos.

B.2. Oceanic Climate - Amsterdam

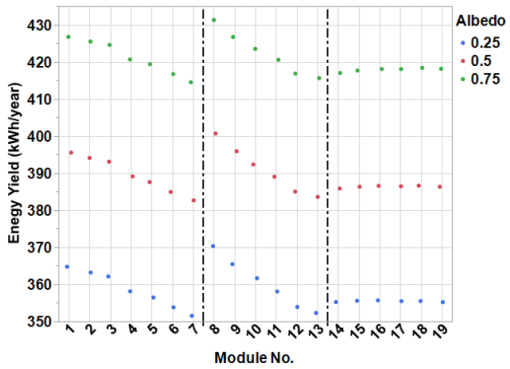

Figure B.3: Yield simulation results for the theoretical modules for different ground albedo at Amsterdam

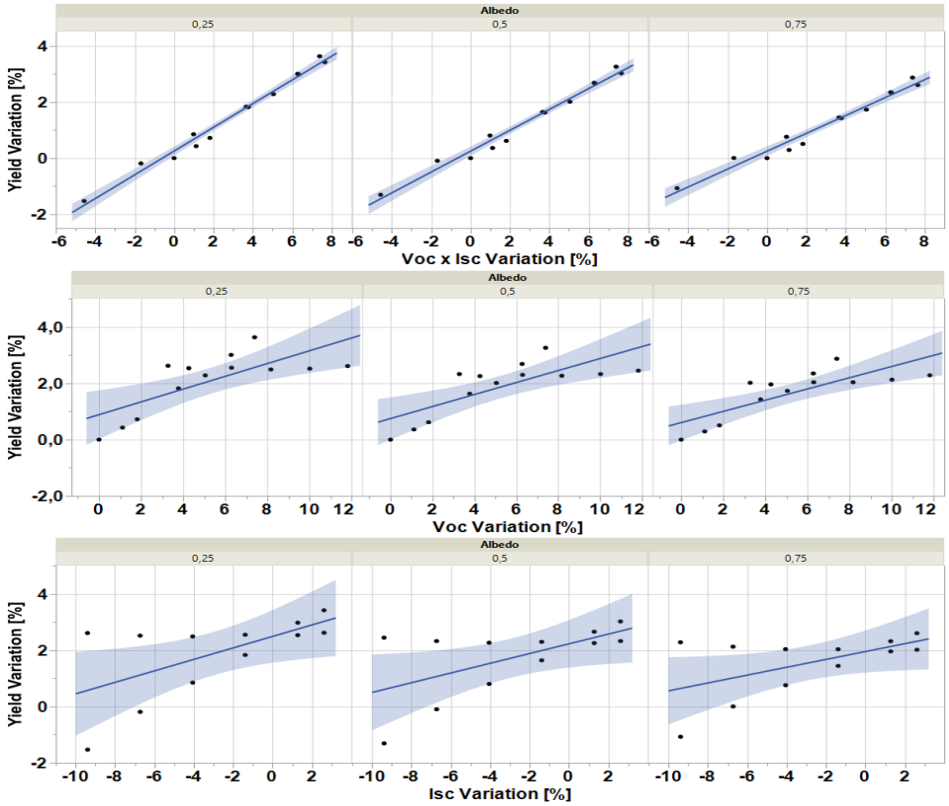

Figure B.4: yield variation against the variation of different parameters at different albedos.

B.3. Oceanic Climate - Vancouver

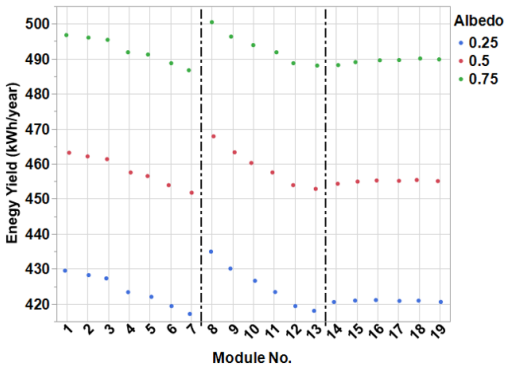

Figure B.5: Yield simulation results for the theoretical modules for different ground albedo at Vancouver

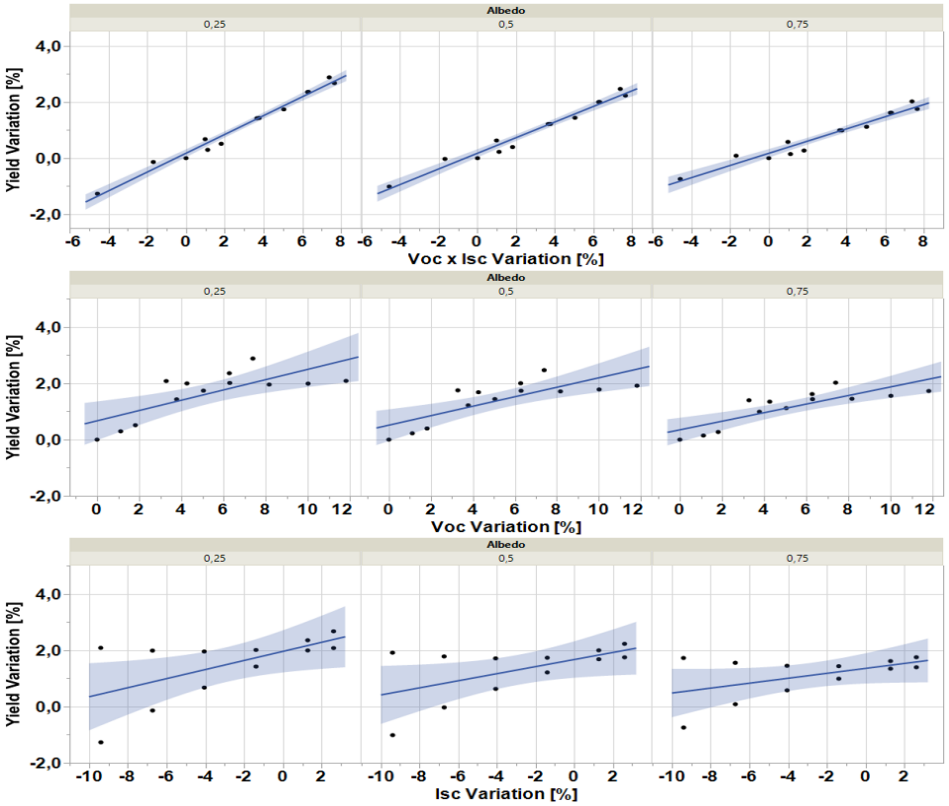

Figure B.6: yield variation against the variation of different parameters at different albedos.

B.4. Oceanic Climate - Chongqing

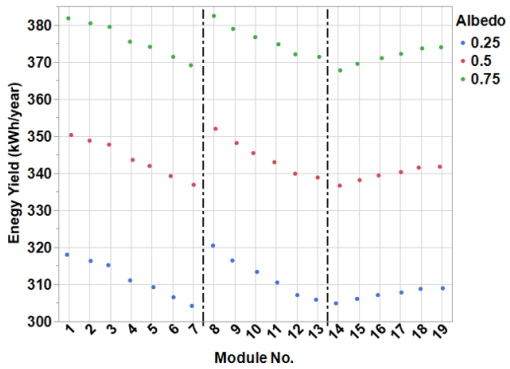

Figure B.7: Yield simulation results for the theoretical modules for different ground albedo at Chongqing

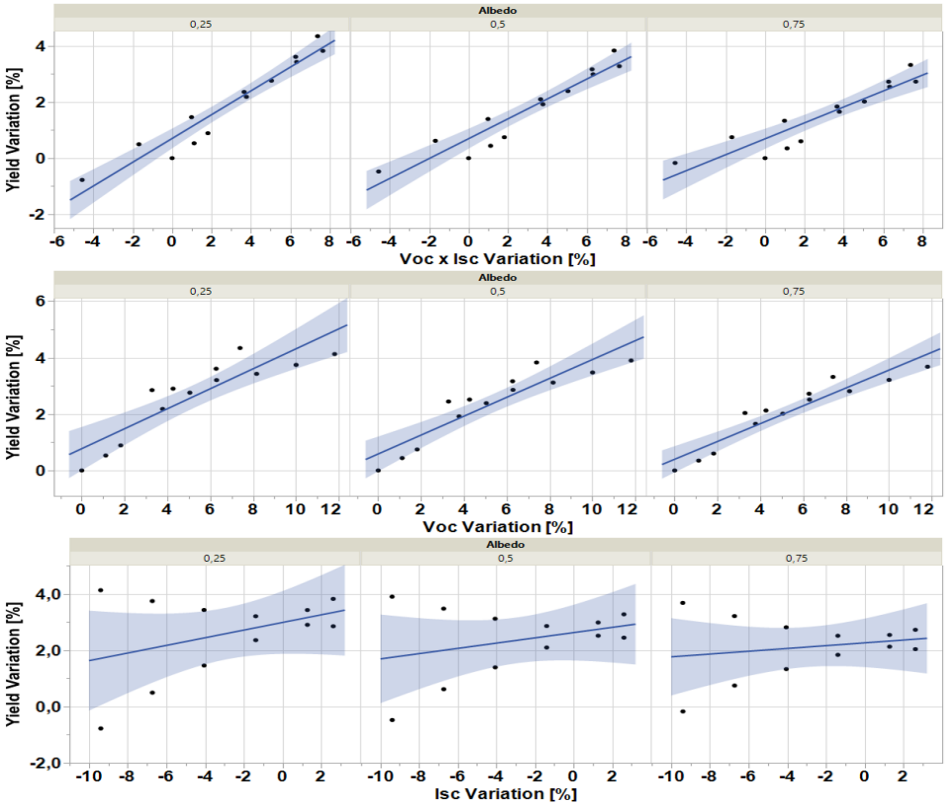

Figure B.8: yield variation against the variation of different parameters at different albedos.

B.5. Oceanic Climate - Malabo

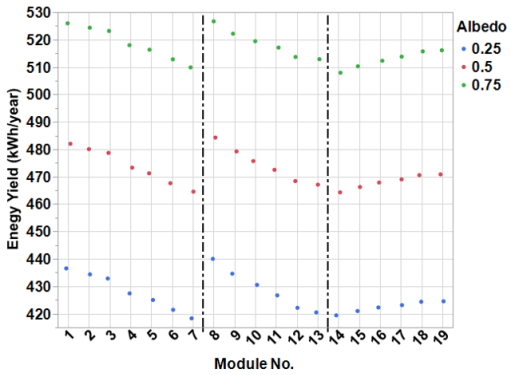

Figure B.9: Yield simulation results for the theoretical modules for different ground albedo at Malabo

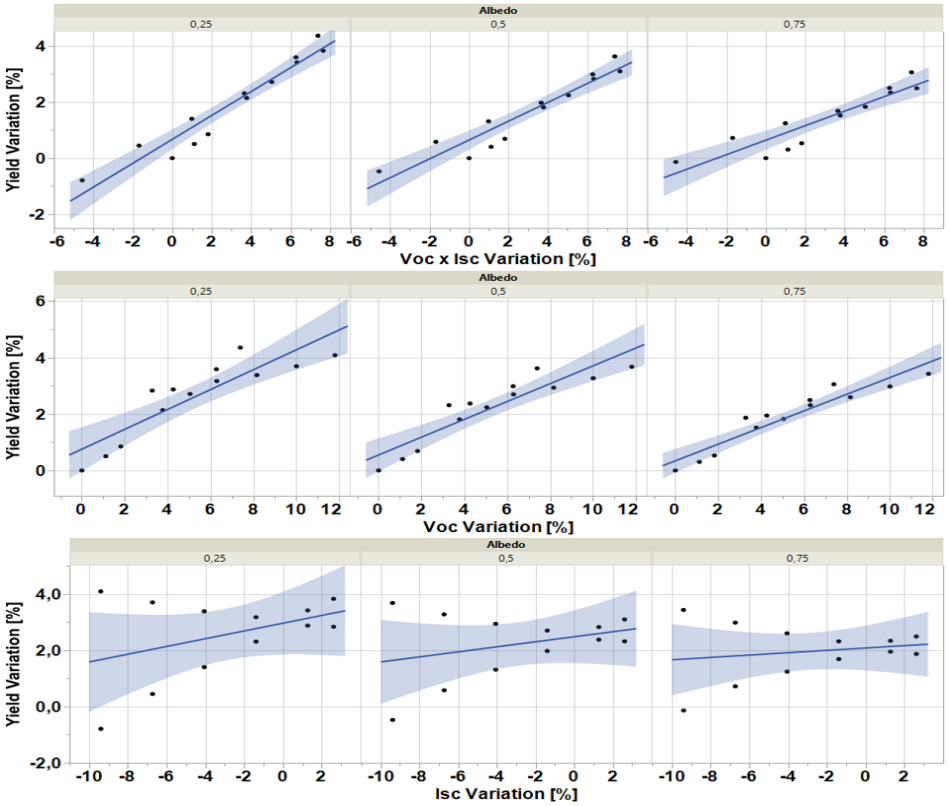

Figure B.10: yield variation against the variation of different parameters at different albedos

B.6. Tropical Climate - Singapore

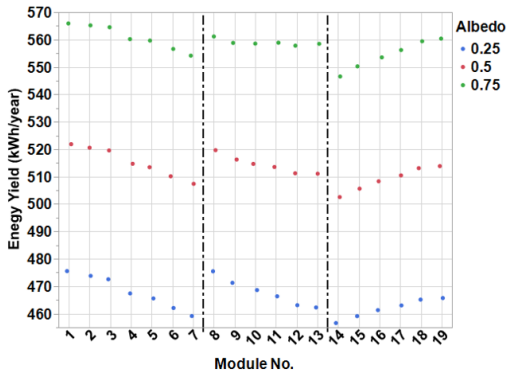

Figure B.11: Yield simulation results for the theoretical modules for different ground albedo at Singapore

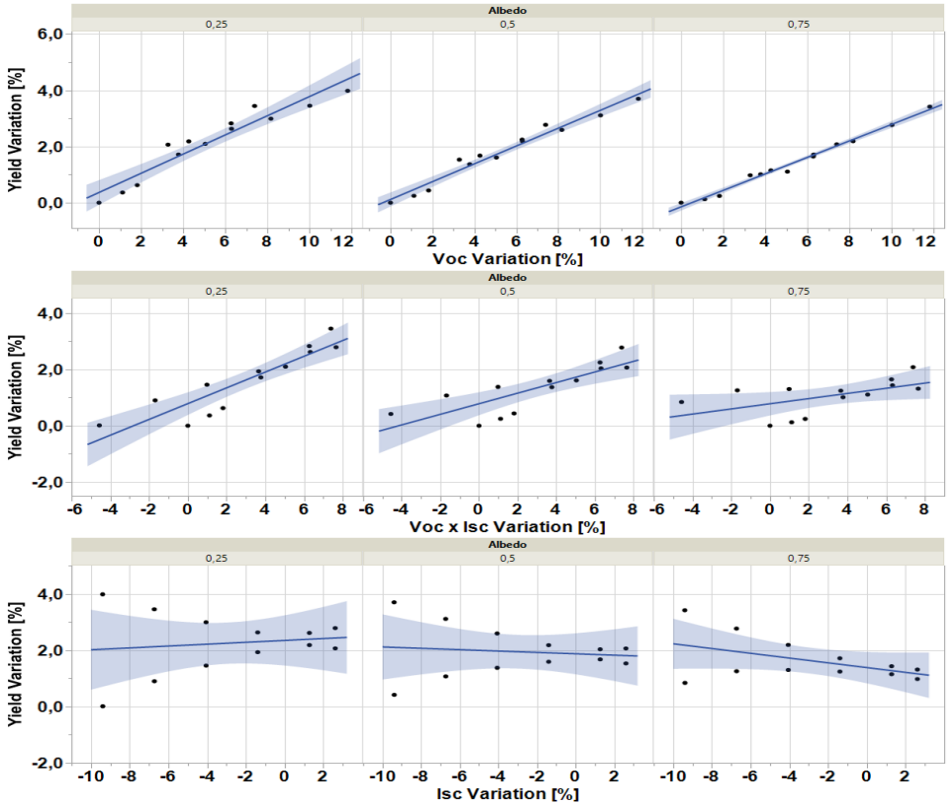

Figure B.12: yield variation against the variation of different parameters at different albedos

B.7. Tropical Climate - Chennai

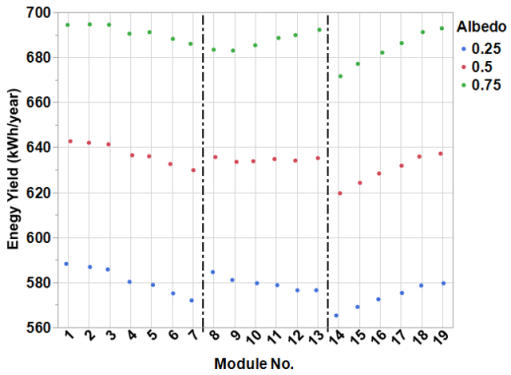

Figure B.13: Yield simulation results for the theoretical modules for different ground albedo at Chennai

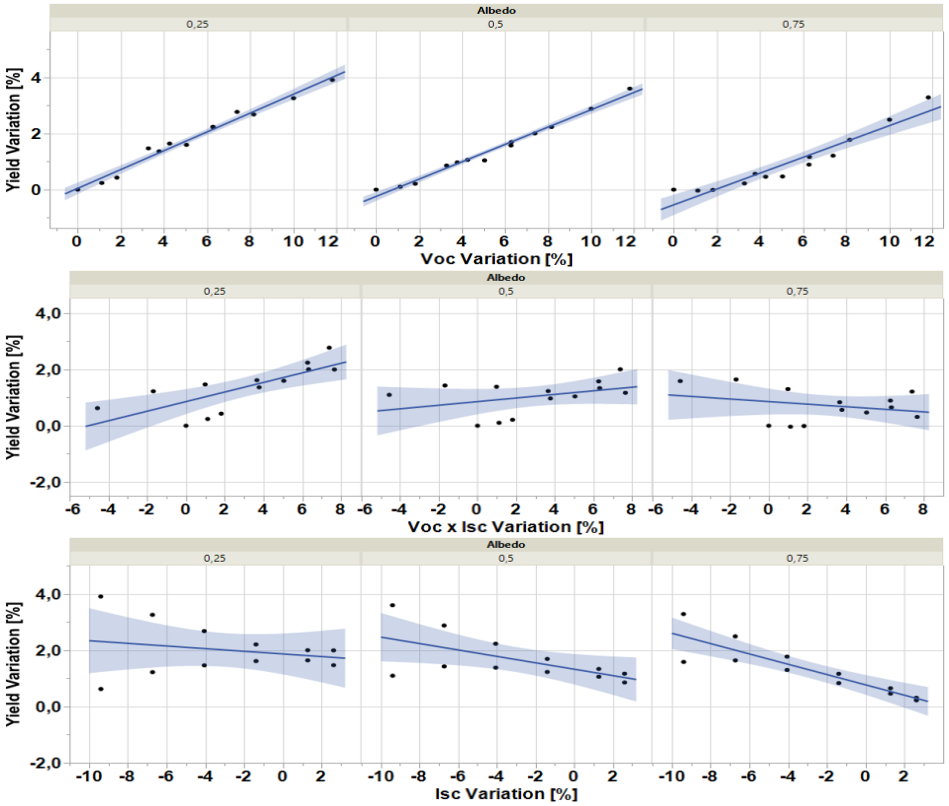

Figure B.14: yield variation against the variation of different parameters at different albedos

B.8. Tropical Climate - Perth

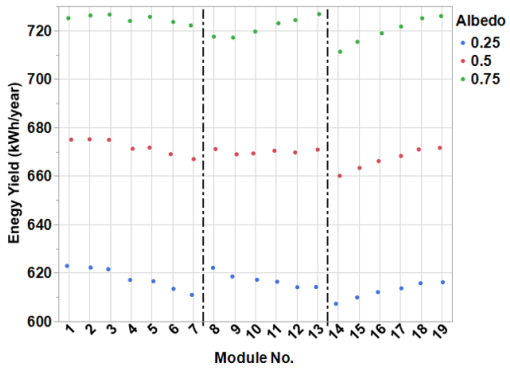

Figure B.15: Yield simulation results for the theoretical modules for different ground albedo at Perth

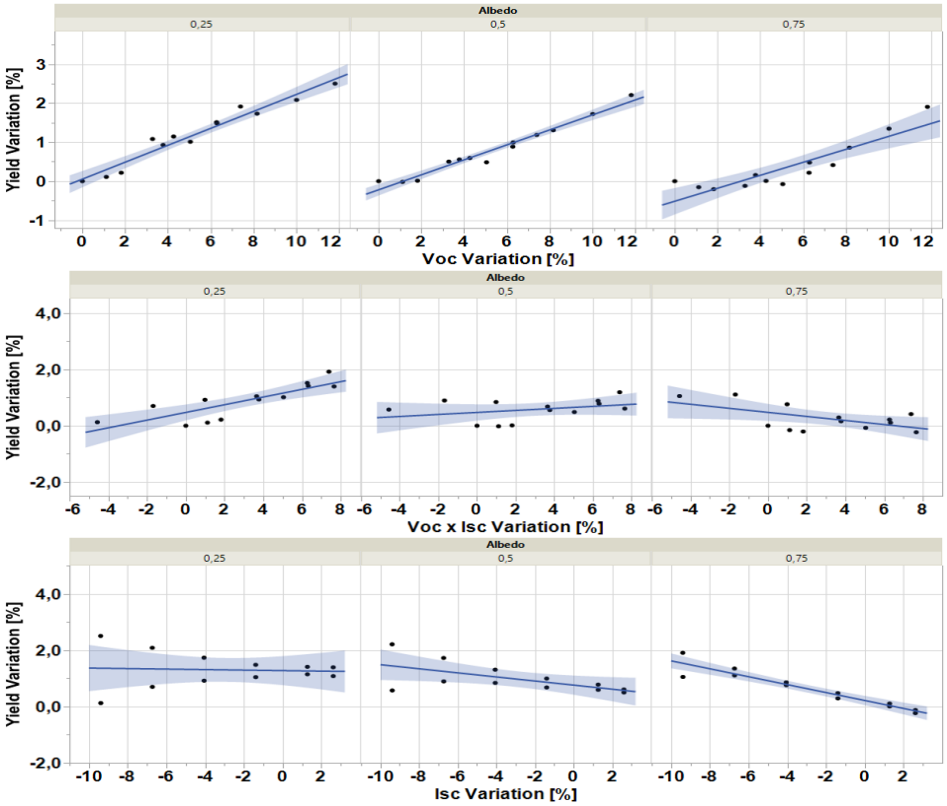

Figure B.16: yield variation against the variation of different parameters at different albedos

B.9. Tropical Climate - Durban

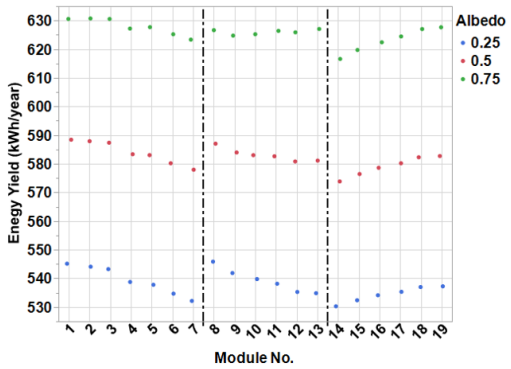

Figure B.17: Yield simulation results for the theoretical modules for different ground albedo at Durban

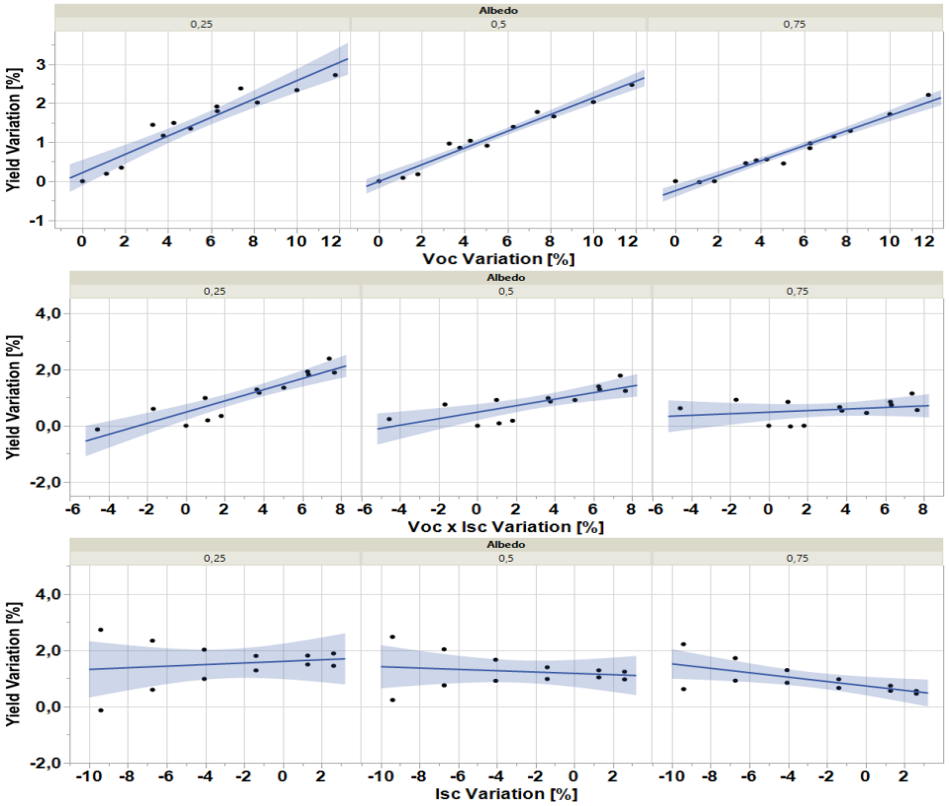

Figure B.18: yield variation against the variation of different parameters at different albedos

B.10. Tropical Climate - Los Angeles

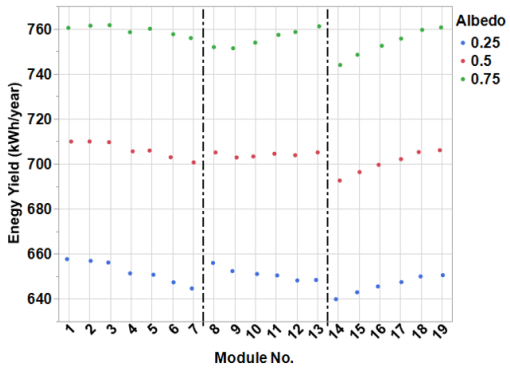

Figure B.19: Yield simulation results for the theoretical modules for different ground albedo at Los Angeles

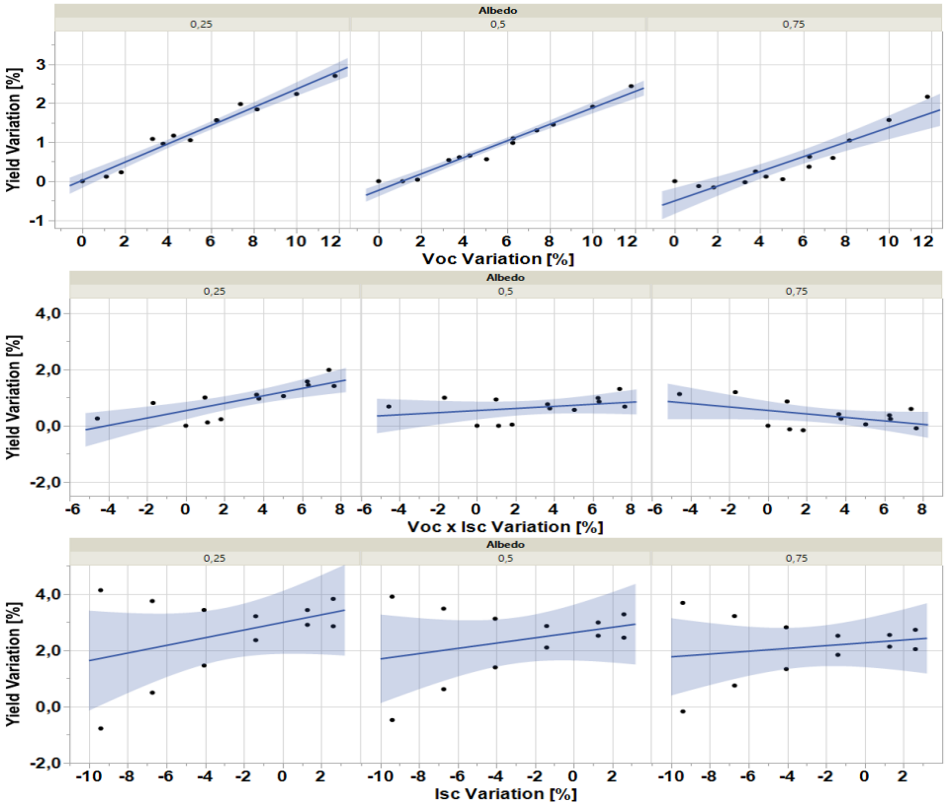

Figure B.20: yield variation against the variation of different parameters at different albedos

B.11. Hot Desert Climate - Cairo

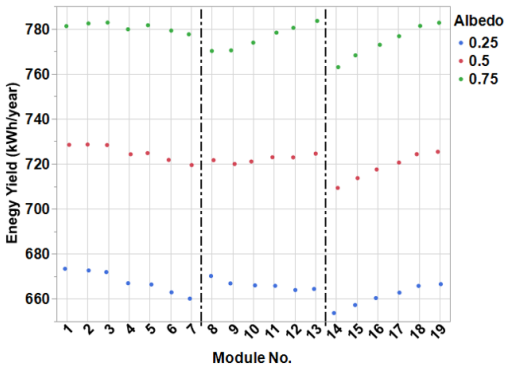

Figure B.21: Yield simulation results for the theoretical modules for different ground albedo at Cairo

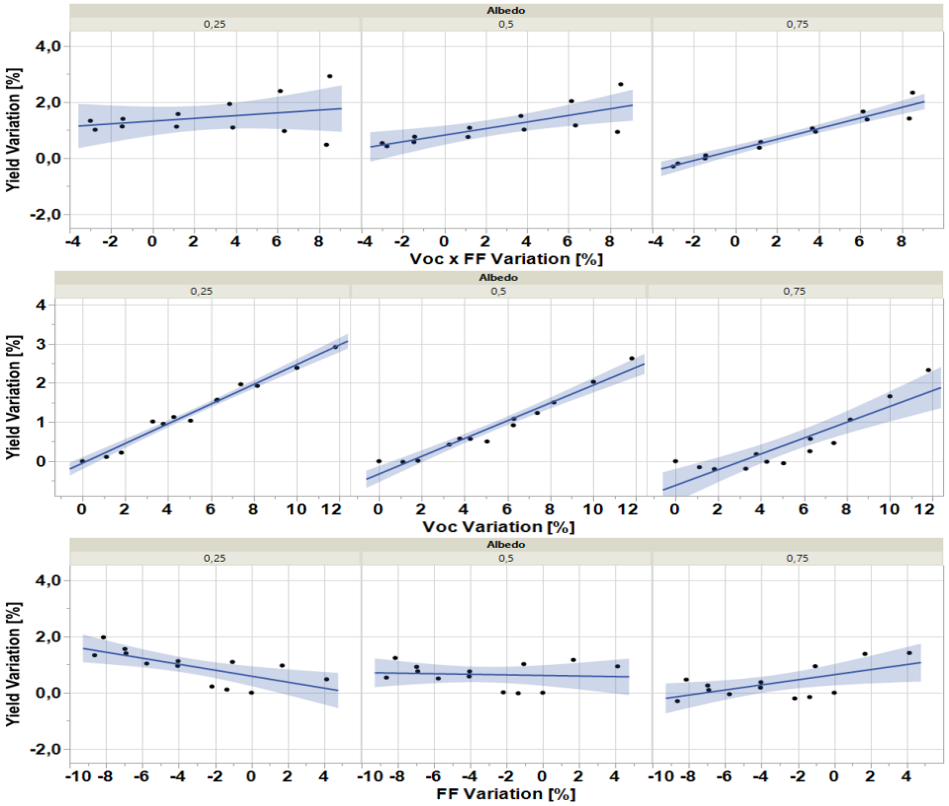

Figure B.22: yield variation against the variation of different parameters at different albedos

B.12. Hot Desert Climate - Port Louis

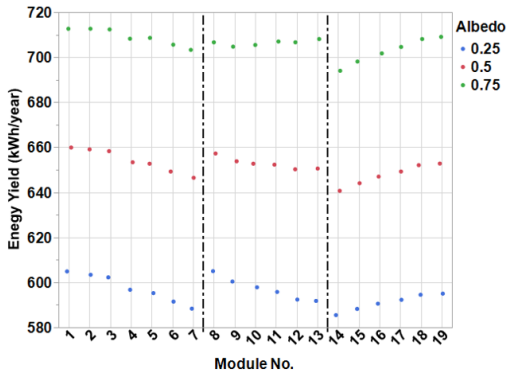

Figure B.23: Yield simulation results for the theoretical modules for different ground albedo at Port Louis

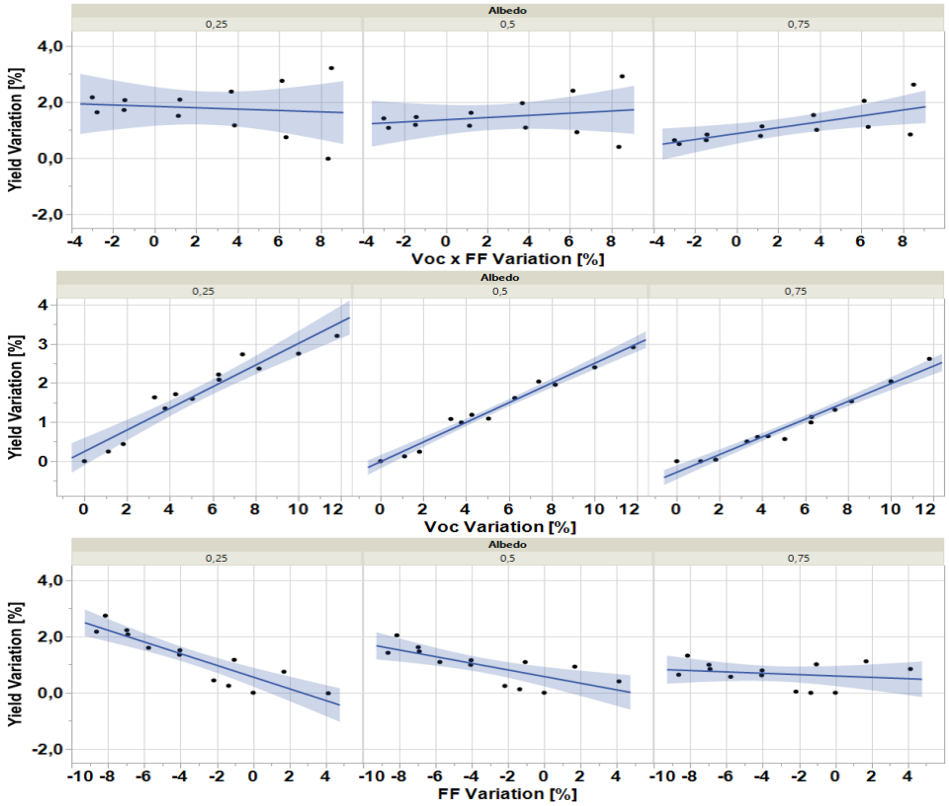

Figure B.24: yield variation against the variation of different parameters at different albedos

B.13. Hot Desert Climate - Doha

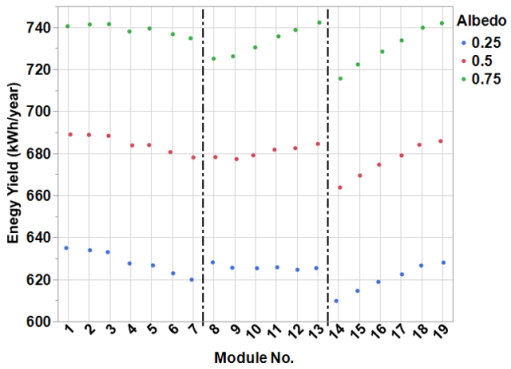

Figure B.25: Yield simulation results for the theoretical modules for different ground albedo at Doha

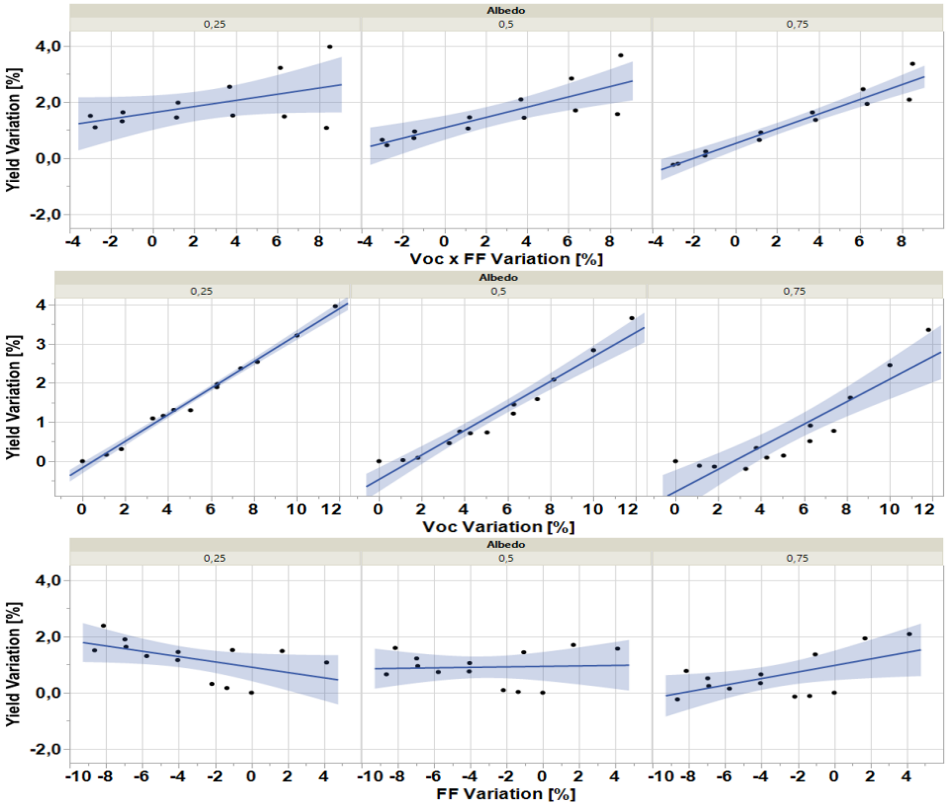

Figure B.26: yield variation against the variation of different parameters at different albedos

C

Metal optimization - additional results

C.1. Singapore - albedo : 0.25

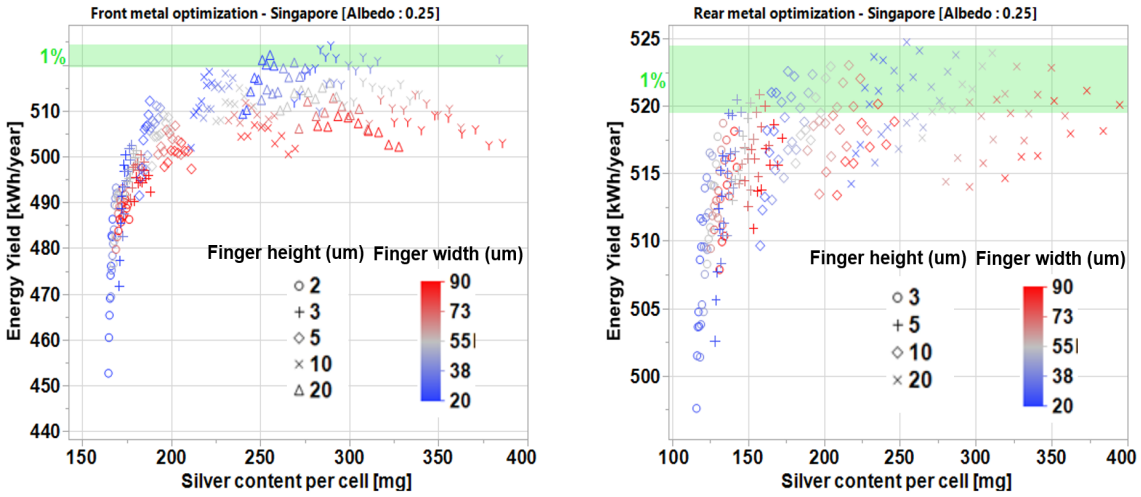

(a) (b)

Figure C.1: Metal pattern optimization results for Singapore (Tropical climate) at albedo of 0.25. a - yield data plotted against the silver content of the cells when front metal pattern is varied with constant rear metal; b - yield data plotted against the silver content of the cells when rear metal pattern is varied with constant front metal

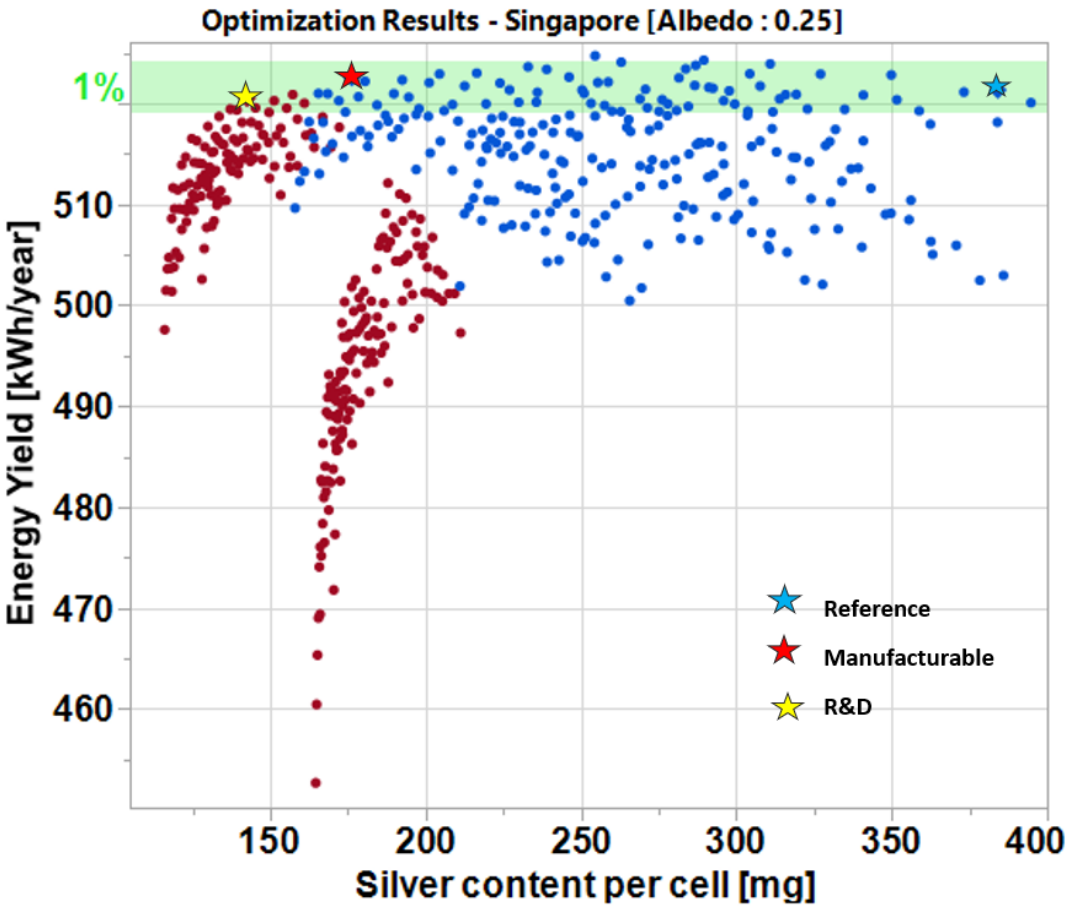

(a)

Figure C.2: The optimization results.Blue dots indicate patterns with height above 5um. Red dots indicate the pattern with thickness of 5 μm. The blue star denotes the reference pattern. The red star denotes the optimal pattern with height above 5 μm. The yellow star denotes the optimal pattern with height 5μm

D

Quokka setting file

```
% An example Quokka v2.2 settings file
% (c) 2014 Andreas Fell

% FRC (front and rear contact) version

version.design='FRC';
% unit cell geometry
geom.dimensions = 2; % set to 1, 2 or 3
geom.Wz = 180; % cell thickness [um] (including thickness of doped surface layers)
geom.Wxfront = 784;% front unit cell size in x-direction [um]
geom.Wxrear = 560; % rear unit cell size in x-direction [um]

% set above values equal to simulate a "standard" unit cell
% set to different values to let Quokka find the actual bigger unit cell
% note that the lowest common multiplier defines the actual unit cell size which may become very large and
slow down the simulation

geom.frontcont.shape='line'; % shape of front contact: 'circle', 'rectangle', 'line' or 'full'
geom.frontcont.wx=20; % contact half width in x-direction for 'rectangle', half width for 'line' or radius for
'circle'
geom.rearcont.shape='line';% shape of rear contact: 'circle', 'rectangle', 'line' or 'full'
geom.rearcont.wx=30;
geom.rearcont.position=[1];
geom.meshquality=1; % determines solution accuracy and computation time, 1: coarse, 2: medium or 3: fine
(or 'user' for expert settings)

% bulk material properties
bulk.type='n-type'; % doping type, 'p-type' or 'n-type'
bulk.rho=2.7; % resistivity [Ohm.cm]
bulk.taubfixed=2e3; % fixed lifetime [us] contribution to bulk recombination, set to very high value to disable
bulk.SRH.midgap.taup0=1e20; % taup (holes) for midgap SRH [us] (Et-Ei=0), set to very high value to disable
bulk.SRH.midgap.taun0=1e20;% taun (electrons) for midgap SRH [us] (Et-Ei=0), set to very high value to dis-
able
bulk.T=298; % temperature [K], leave at 300 K unless you are confident about what you are doing
bulk.Auger='Richter2012'; % Auger model: 'Richter2012' (default), 'Altermatt2011', 'Kerr2002', 'Sinton1987'
or 'off'
bulk.mobility='Klaassen'; % mobility model, 'Klaassen' (default) or 'Arora' (PC1D)

% Boundary properties, conductive (e.g. surface diffusion) and non-conductive (e.g. undiffused passivated
surface)
```

```
% Only one non-conductive boundary per front and rear surface can be defined, which is applied to wherever no other conductive boundary is defined
% 'cont' / 'noncont' denotes the contacted / non-contacted area
% For 1D, 'cont' i.e. contacted area properties will be used
% Several boundaries can be defined by cell indexing, note that a higher index overrides lower index boundaries if their shapes intersect
% Only applicable inputs must be given, e.g. contacted properties don't need to be defined if no area of the boundary is contacted

% Properties of all boundaries:
% .location: 'front' or 'rear'
% .cont.rec: recombination model of contacted area; 'S', 'J0' or 'expr'
% .noncont.rec: same as above of non-contacted area
% .cont.S: effective SRV [cm/s] of contacted area if if cont.rec='S'
% .noncont.S: same as above of non-contacted area
% .cont.J0: ideal (n=1) recombination current prefactor [A/cm2] of contacted area if cont.rec='J0'
% .noncont.J0: same as above of non-contacted area
% .noncont.expr: same as above of non-contacted area
% .cont.rc: contact resistivity [Ohm.cm2] of contacted area
% Additional applicable properties for conductive boundaries only
% .Rsheet: sheet resistance [Ohm/sq]
% .shape: 'none' (to disable), 'full', 'line', 'rectangle', 'circle' or 'contact' (the latter applies the same shape and dimensions as the contact on the respective side)
% .wx: half width in x-direction for 'rectangle', half width for 'line' or radius for 'circle' [um]
% .wy: half width in y-direction for 'rectangle' [um]

% optional expert boundary properties
% .cont.J02: nonideal (n=2) recombination current prefactor [A/cm2] of contacted area
% .noncont.J02: same as above of non-contacted area
% .jctdepth: junction depth [um], used for determination of collection current within the boundary
% additionally the area average of the junction depths is applied for reduction of the solution domain width in z-direction
% .colleff: collection efficiency [], used for determination of collection current within the boundary

% full area front emitter diffusion (automatically set to p-type):
bound.conduct1.location='front';
bound.conduct1.Rsheet=85;
bound.conduct1.noncont.rec='J0';
bound.conduct1.noncont.J0=45e-15;
bound.conduct1.cont.rec='J0';
bound.conduct1.cont.J0=1500e-15;
bound.conduct1.shape='full';
bound.conduct1.jctdepth=0.5;
bound.conduct1.colleff=1;
bound.conduct1.cont.rc=3e-3;

% non contacted rear BSF (automatically set to n-type):
bound.conduct2.location='rear';
bound.conduct2.Rsheet=70;
bound.conduct2.noncont.rec='J0';
bound.conduct2.noncont.J0=5e-15;
bound.conduct2.shape='full';
bound.conduct2.cont.rec='J0';
bound.conduct2.cont.J0=200e-15;
bound.conduct2.cont.rc=1e-3;
bound.conduct2.jctdepth=0.2;
```

```
bound.conduct2.colleff=0;
bound.conduct2.noncont.J02=1e-8;

generation.type='ext_file'; % how generation is defined: '1D_model', 'Jgen_surface', 'Jgen_uniform', 'ext_file', 'customdata' or 'off'
generation.intensity=100; % incident light intensity [mW/cm2] (default: 100), not applicable for 1D_model, does NOT influence the actual generation
generation.Jgen=40;% generation current [mA/cm2] (will be applied to the illuminated side surface or uniformly in the bulk)
generation.ext_file='Scaled39p5.txt'; % generation rate file; first column depth [um], second column G [cm-3s-1]
generation.customdata=[]; % generation rate vector data: [z1, z2, ... zn; G1, G2, ... Gn] with z = distance to illuminated surface [um] and G = generation rate [cm-3]
generation.suns=1; % scales the generation
generation.illum_side='front'; % illuminated side, 'front' or 'rear'
generation.shading_width=74.7318; % half width in x-direction [um] for shading of fingers, set to zero for no shading

% external circuit settings
circuit.Rseries=0.1166; % external series resistance [Ohm.cm2]
circuit.Rshunt=1e5; % external shunt resistance [Ohm.cm2]
circuit.terminal='light_IV_auto'; % 'Vuc', 'Vterm', 'Jterm', 'OC', 'MPP', 'Jsc' (not short circuit!), 'light_IV_auto', 'IV_curve', 'QE_curve' or 'sunsVoc_curve'
circuit.Vuc.value=0.5; % unit vell voltage [V] for 'Vuc'
circuit.Vterm.value=0.5;% terminal voltage [V] for 'Vterm'
circuit.Jterm.value=-30; % terminal current density [mA/cm2] for 'Jterm'
circuit.IV.V_values=[0.2:0.05:0.75]; % vector of voltage values [V] for 'IV_curve'
circuit.IV.mode='Vterm';% 'Vuc' (faster) or 'Vterm' defines the meaning of the voltage values for 'IV_curve'
circuit.QE.wavelength_values=[300:25:1125]; % vector of wavelength values [nm] for 'QE_curve'
circuit.sunsVoc.suns_values=10.^[-4:0.5:1];

circuit.DJ0=0; % J0 [A/cm2] of external parallel diode in forward bias
circuit.Dn=2; % ideality factor of external parallel diode in forward bias
circuit.Voc_guess=0.67; % guess of Voc [V] for quicker convergence, can be a vector / matrix for sweeps
circuit.IV_accuracy=2; % use values >1 to increase the number of IV points calculated for 'light_IV_auto'; default: 1
```

Bibliography

[1] A. J. Arnfield, "Causes of climate change," 2014.

[2] H. R. . M. Roser, "Co2 and other greenhouse gas emissions," 2017.

[3] I. energy agency, "Co2 emissions statistics," tech. rep., International energy agency, 2018.

[4] E. of Britannica, "Paris agreement," 04 2019.

[5] O. Edenhofer, R. Pichs-Madruga, Y. Sokona, E. Farahani, S. Kadner, K. Seyboth, A. Adler, I. Baum, S. Brunner, P. Eickemeier, B. Kriemann, J. Savolainen, S. Schlömer, C. von Stechow, T. Zwickel, and J. M. (eds.)], "Ipcc, 2014: Summary for policymakers," tech. rep., Cambridge University Press, Cambridge, United Kingdom and New York, NY, USA., 2014.

[6] IEA, "Global annual net energy capacity addition by type," tech. rep., International Energy Agency, 2017.

[7] M. Pehl, A. Arvesen, F. Humpenöder, A. Popp, E. G. Hertwich, and G. Luderer, "Understanding future emissions from low-carbon power systems by integration of life-cycle assessment and integrated energy modelling," *Nature Energy*, vol. 2, pp. 939–945, 2017.

[8] Guerrero-Lemus, R. Vega, T. Kim, A. Kimm, and L. Shephard, "Bifacial solar photovoltaics – a technology review," tech. rep., University of Texas at San Antonio, 2016.

[9] E. Troster and J.-D. Schmidt, "Evaluating the impact of pv module orientation on grid operation," tech. rep., Energy Nautics, 2018.

[10] M. Khan, A. Hanna, X. Sun, and M. Alam, "Vertical bifacial solar farms: Physics, design, and global optimization," *Applied Energy*, vol. 206, 04 2017.

[11] X. Sun, M. Khan, C. Deline, and M. Ashraful Alam, "Optimization and performance of bifacial solar modules: A global perspective," *Applied Energy*, vol. 212, 09 2017.

[12] E. Gerritsen, G. Janssen, and C. Deline, *Bi-facial photovoltaics: technology, applications and economics*. 2017.

[13] T. C. R. Russell, R. Saive, A. Augusto, S. G. Bowden, and H. A. Atwater, "The influence of spectral albedo on bi-facial solar cells: A theoretical and experimental study," tech. rep., California institute of technology and Arizona state university, 2017.

[14] "Calculating the additional energy yield of bi-facial solar modules."

[15] B. Y. H. Liu and R. C. Jordan, "The interrelationship and characteristic distribution of direct, diffuse and total solar radiation," tech. rep., 1960.

[16] U. A. Yusufoglu, T. Pletzer, L. Koduvelikulathu, C. Comparotto, R. Kopecek, and H. Kurz, "Analysis of the annual performance of bifacial modules and optimization methods," *IEEE Journal of Photovoltaics*, vol. 5, pp. 320–328, 01 2015.

[17] R. Perez, R. Seals, P. Ineichen, R. Stewart, and D. Menicucci, "A new simplified version of the perez diffuse irradiance model for tilted surfaces," *Solar Energy*, vol. 39, no. 3, pp. 221 – 231, 1987.

[18] J. A Duffie and W. Beckman, *Solar Engineering of Thermal Processes*. 01 2006.

[19] M. Lamers, E. Özkalay, R. Gali, G. Janssen, A. Weeber, I. Romijn, and B. V. Aken, "Temperature effects of bifacial modules: Hotter or cooler?," *Solar Energy Materials and Solar Cells*, vol. 185, pp. 192 – 197, 2018.

[20] D. Faiman, "Assessing the outdoor operating temperature of photovoltaic modules," *Progress in Photovoltaics: Research and Applications*, vol. 16, pp. 307 – 315, 06 2008.

[21] W. De Soto, S. Klein, and W. Beckman, "Improvement and validation of a model for photovoltaic array performance," *Solar Energy*, vol. 80, pp. 78–88, 01 2006.

[22] G. Janssen, B. A.R., A. Carr, B. Van Aken, I. Romijn, M. Klenk, and T. Nussbaumer, H.and Baumann, "How to maximize the kwh/kwp ratio: Simulations of single-axis tracking in bifacial systems," *EUPVSEC*, 2018.

[23] E. Wladimir Koppen (translated edited by Volken and S. Brönnimann), "The thermal zones of the earth according to the duration of hot, moderate and cold periods and of the impact of heat on the organic world," 1884.

[24] A. J. Arnfield, "Köppen climate classification," 2019.

[25] M. Kottek, J. Grieser, C. Beck, B. Rudolf, and F. Rubel, "World map of the köppen-geiger climate classification updated," 2006.

[26] D. Chen and H. Chen, "Using the koppen classfication to quantify climate variation and change; an example for 1901-2010," tech. rep., 2013.

[27] A. Fell, "A free and fast three-dimensional/two-dimensional solar cell simulator featuring conductive boundary and quasi-neutrality approximations," *IEEE Transactions on Electron Devices*, vol. 60, pp. 733–738, Feb 2013.

[28] "Settings file generator."

[29] A. Burgers, G. Janssen, and B. V. Aken, "Bigeye: Accurate energy yield prediction of bifacial pv systems," tech. rep., ECN part of TNO, 2018.

[30] P. L. house, "Pv lighthouse: Equivalent circuit calculator," 2016.

[31] E. Commission, "Typical meterological year generator," 2017.

[32] N. S. P. et al, "Results 2017 and maturity report 2018," tech. rep., Internaltional technology roadmap for photovoltaics, 2018.

[33] M. Stodolny, M. Lenes, Y. Wu, G. Janssen, I. Romijn, J. Luchies, and L. Geerligs, "n-type polysilicon passivating contact for industrial bifacial n-type solar cells," *Solar energy materials and solar cells*, vol. 158, pp. 24–28, 2016.

[34] "Grid calculator," 2016.

[35] A. Fell, "Quokka," 2016.

[36] A. R. Burgers, J. A. Eikelboom, A. Schonecker, and W. C. Sinke, "Improved treatment of the strongly varying slope in fitting solar cell i-v curves," 1996.

[37] A. Lorenz, M. Linse, H. Frintrup, M. Jeitler, A. Mette, M. Lehner, R. Greutmann, H. Brocker, M. König, D. Erath, and F. Clement, "Screen printed thick film metallization of silicon solar cells - recent developments and future perspectives," *35th European Photovoltaic Solar Energy Conference and Exhibition*, pp. 819 – 824, 12 2015.

[38] R. Fu, D. Feldman, and R. Margolis, "U.s. solar photovoltaic system cost benchmark: Q1 2018," tech. rep., National Renewable Energy Laboratory, USA, 2018.

[39] T. Silverman, M. Deceglie, and K. Horowitz, "Nrel comparative pv lcoe calculator," 2018.

[40] A. Richter, M. Hermle, and S. W. Glunz, "Reassessment of the limiting efficiency for crystalline silicon solar cells," *IEEE Journal of Photovoltaics*, vol. 3, pp. 1184–1191, Oct 2013.

[41] B. Andrew W, A. Wang, A. M, Milne, J. Zhao, and M. A. Green, "22.8% efficient solar cell," *Applied Physics*, vol. 55, pp. 1363–1365, 1989.

[42] T. Dullweber and J. Schmidt, "Industrial silicon solar cells applying the passivated emitter and rear cell (perc) concept—a review," *IEEE Journal of Photovoltaics*, vol. 6, p. 1366, 06 2016.

[43] A. Metz, D. Adler, S. Bagus, H. Blanke, M. Bothar, E. Brouwer, S. Dauwe, K. Dressler, R. Droessler, T. Droste, M. Fiedler, Y. Gassenbauer, T. Grahl, N. Hermert, W. Kuzminski, A. Lachowicz, T. Lauinger, N. Lenck, M. Manole, and K. Wangemann, "Industrial high performance crystalline silicon solar cells and modules based on rear surface passivation technology," *Solar Energy Materials and Solar Cells*, vol. 120, pp. 417–425, 01 2014.

[44] Z. Wang, P. Han, H. Lu, H. Qian, L. Chen, Q. Meng, N. Tang, F. Gao, Y. Jiang, J. Wu, W. Wu, H. Zhu, J. Ji, Z. Shi, A. Sugianto, L. Mai, B. Hallam, and S. Wenham, "Advanced perc and perl production cells with 20.3% record efficiency for standard commercial p-type silicon wafers," *Progress in Photovoltaics: Research and Applications*, vol. 20, no. 3, pp. 260–268, 2012.

[45] "Solarworld reaches 22% efficiency in p-type perc cell," Jan 2016.

[46] K. Pickerel, "Longi solar reaches 24.06% efficiency with its bifacial mono-perc modules," 01 2019.

[47] M. Müller, G. Fischer, B. Bitnar, S. Steckemetz, R. Schiepe, M. Mühlbauer, R. Köhler, P. Richter, C. Kusterer, A. Oehlke, E. Schneiderlöchner, H. Sträter, F. Wolny, M. Wagner, P. Palinginis, and D. Neuhaus, "Loss analysis of 22% efficient industrial perc solar cells," *Energy Procedia*, vol. 124, pp. 131–137, 09 2017.

[48] J. H. Zhao, A. Wang, and M. Green, "24.5% efficiency silicon pert cells on mcz substrates and 24.7% efficiency perl cells on fz substrates," *Progress in Photovoltaics: Research and Applications*, vol. 7, pp. 471–474, 11 1999.

[49] A. Smets, K. Jäger, O. Isabella, R. Van Swaaij, and M. Zeman, *Solar Energy - The physics and engineering of photovoltaic conversion, technologies and systems*. UIT cambridge, 02 2016.

[50] T. Kim, J.-K. Lim, H.-N.-R. Shin, D. Kyeong, J. Cho, M. Kim, J. Lee, H. Park, K. Lee, W.-j. Lee, and E. Cho, "21%-efficient perl solar cells with plated front contacts on industrial 156mm p-type crystalline silicon wafers," *Energy Procedia*, vol. 55, pp. 431–436, 12 2014.

[51] J. Zhao, A. Wang, and M. Green, "Series resistance caused by the localized rear contact in high efficiency silicon solar cells," *Solar Energy Materials and Solar Cells*, vol. 32, p. 89–94, 01 1994.

[52] L. Tous, M. Aleman, R. Russell, E. Cornagliotti, P. Choulat, A. Uruena, S. Singh, J. John, F. Duerinckx, J. Poortmans, and R. Mertens, "Evaluation of advanced p-perl and n-pert large area silicon solar cells with 20.5% energy conversion efficiencies," *Progress in Photovoltaics: Research and Applications*, vol. 23, 02 2014.

[53] A. Uruena, M. Aleman, E. Cornagliotti, A. Sharma, J. Deckers, M. Haslinger, L. Tous, R. Russell, J. John, Y. Yao, T. Söderström, F. Duerinckx, and J. Szlufcik, "Beyond 22% large area n-type silicon solar cells with front laser doping and a rear emitter," 09 2015.

[54] A. Richter, J. Benick, R. Müller, F. Feldmann, C. Reichel, M. Hermle, and S. Glunz, "Tunnel oxide passivating electron contacts as full-area rear emitter of high-efficiency p-type silicon solar cells," *Progress in Photovoltaics: Research and Applications*, vol. 26, 11 2017.

[55] C. Yu, S. Xu, J. Yao, and S. Han, "Recent advances in and new perspectives on crystalline silicon solar cells with carrier-selective passivation contacts," *Crystals*, 11 2018.

[56] A. Richter, J. Benick, R. Müller, F. Feldmann, C. Reichel, M. Hermle, and S. Glunz, "n-type si solar cells with passivating electron contact: Identifying sources for efficiency limitations by wafer thickness and resistivity variation," *Solar energy materials and solar cells*, vol. 173, pp. 96–105, 5 2017.

[57] Z. P. Ling, Z. Xin, R. S. Puqun Wang, C. Ke, and R. Stangl, "Double-sided passivated contacts for solar cell applications: An industrially viable approach toward 24% efficient large area silicon solar cells," *Intechopen*, 3 2019.

[58] B. Steinhauser, F. Feldmann, J.-I. Polzin, L. Tutsch, V. Arya, B. Grübel, A. Fischer, A. Moldovan, J. Benick, A. Richter, A. Brand, S. Kluska, and M. Hermle, "Large area topcon technology achieving 23.4% efficiency," 06 2018.

[59] K. Yoshikawa, H. Kawasaki, W. Yoshida, T. Irie, K. Konishi, K. Nakano, T. Uto, D. Adachi, M. Kanematsu, H. Uzu, and K. Yamamoto, "Exceeding conversion efficiency of 26% by heterojunction interdigitated back contact solar cell with thin film si technology," *Solar energy materials and solar cells*, vol. 173, pp. 37–42, 2017.

[60] J. Seif, A. Descoeudres, M. Filipic, F. Smole, M. Topic, Z. Charles Holman, S. De Wolf, and C. Ballif, "Amorphous silicon oxide window layers for high-efficiency silicon heterojunction solar cells," *Journal of Applied Physics*, vol. 024502, p. 115, 01 2014.

[61] C. Chana, B. Hallam, and S. Wenham, "Simplified interdigitated back contact solar cells," *Energy Procedia*, vol. 27, pp. 543–548, 2012.